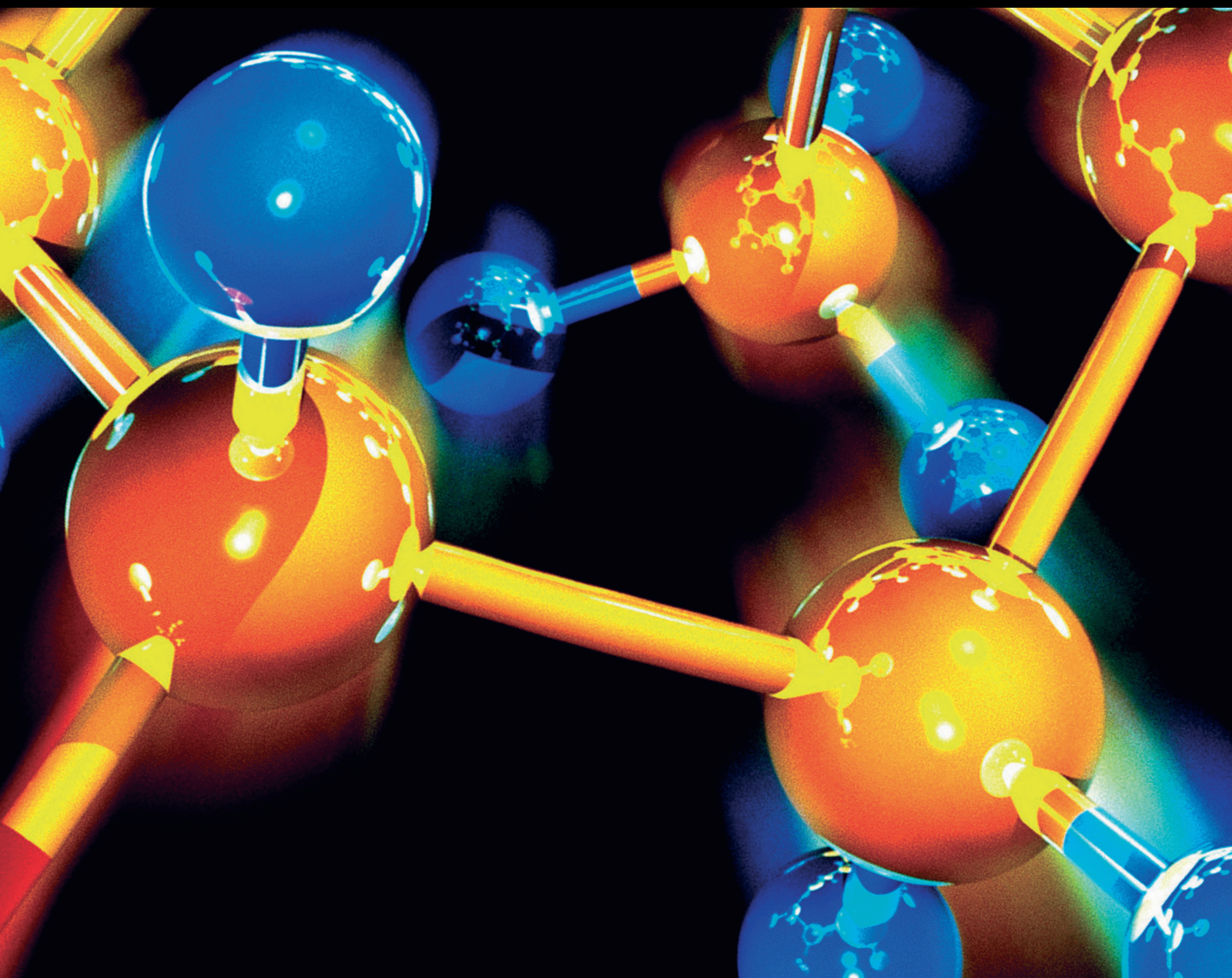


Journal of Chemistry

Nanotechnology for Food Engineering: Biomembrane and Nanocarriers

Lead Guest Editor: Pahn-Shick Chang

Guest Editors: Hiroshi Umakoshi and Hakjin Kim





Nanotechnology for Food Engineering: Biomembrane and Nanocarriers

Journal of Chemistry

**Nanotechnology for Food Engineering:
Biomembrane and Nanocarriers**

Lead Guest Editor: Pahn-Shick Chang

Guest Editors: Hiroshi Umakoshi and Hakjin Kim



Copyright © 2019 Hindawi. All rights reserved.

This is a special issue published in "Journal of Chemistry." All articles are open access articles distributed under the Creative Commons Attribution License, which permits unrestricted use, distribution, and reproduction in any medium, provided the original work is properly cited.

Contents

Nanotechnology for Food Engineering: Biomembrane and Nanocarriers

Pahn-Shick Chang , Hiroshi Umakoshi , and Hakjin Kim
Editorial (3 pages), Article ID 4629365, Volume 2019 (2019)

Synthesis and Application of Nanomagnetic Immobilized Phospholipase C

Yang Jiang, Jing Du, Honglin Tang, Xin Zhang, Wenbin Li, Liqi Wang, Lianzhou Jiang, and Dianyu Yu 
Research Article (9 pages), Article ID 5951793, Volume 2019 (2019)

Detection of L-Proline-Catalyzed Michael Addition Reaction in Model Biomembrane

Masanori Hirose, Shigenori Sugisaki, Keishi Suga , and Hiroshi Umakoshi 
Research Article (8 pages), Article ID 4926435, Volume 2019 (2019)

Functional Hydration Behavior: Interrelation between Hydration and Molecular Properties at Lipid Membrane Interfaces

Nozomi Watanabe, Keishi Suga , and Hiroshi Umakoshi 
Review Article (15 pages), Article ID 4867327, Volume 2019 (2019)

Investigation of the Thermal Performance of Salt Hydrate Phase Change of Nanoparticle Slurry Flow in a Microchannel

Safi A. Memon , M. B. Sajid, M. S. Malik , Awad B. S. Alquaity , M. Mohib ur. Rehman, Taqi A. Cheema , Moon Kyu Kwak , and Cheol Woo Park 
Research Article (10 pages), Article ID 5271923, Volume 2019 (2019)

Continuous Fabrication of Wide-Tip Microstructures for Bio-Inspired Dry Adhesives via Tip Inking Process

Sung Ho Lee, Cheol Woo Park , and Moon Kyu Kwak 
Research Article (5 pages), Article ID 4827918, Volume 2019 (2019)

Influence of Oxidants on the Stability of Tocopherol in Model Nanoemulsions: Role of Interfacial Membrane Organized by Nonionic Emulsifiers

Jinhyuk Kim, Ha Youn Song, and Seung Jun Choi 
Research Article (8 pages), Article ID 6438787, Volume 2018 (2019)

An Overview of Nanotechnology in Food Science: Preparative Methods, Practical Applications, and Safety

Hyunjong Yu, Jun-Young Park, Chang Woo Kwon , Sung-Chul Hong, Kyung-Min Park, and Pahn-Shick Chang 
Review Article (10 pages), Article ID 5427978, Volume 2018 (2019)

Editorial

Nanotechnology for Food Engineering: Biomembrane and Nanocarriers

Pahn-Shick Chang ¹, **Hiroshi Umakoshi** ², and **Hakjin Kim**³

¹Department of Agricultural Biotechnology, Research Institute of Agriculture and Life Sciences, Center for Food and Bioconvergence, Seoul National University, Seoul 08826, Republic of Korea

²Bio-Inspired Chemical Engineering Laboratory, Division of Chemical Engineering, Graduate School of Engineering Science, Osaka University, Toyonaka, Osaka, Japan

³Department of Biosystems & Biomaterials Science and Engineering, Research Institute of Agriculture and Life Sciences, Seoul National University, Seoul 08826, Republic of Korea

Correspondence should be addressed to Pahn-Shick Chang; pschang@snu.ac.kr

Received 3 February 2019; Accepted 3 February 2019; Published 24 March 2019

Copyright © 2019 Pahn-Shick Chang et al. This is an open access article distributed under the Creative Commons Attribution License, which permits unrestricted use, distribution, and reproduction in any medium, provided the original work is properly cited.

Nanotechnology has been hired in various areas of food engineering and technology. Recent research has begun to address the potential applications of nanotechnology for functional foods and nutraceuticals by applying the new concepts and engineering approaches involved in nanomaterials to target delivery of bioactive compounds and nutrients. “Nano” must exist naturally in food because even in natural foods, structural components are built from molecules and, during digestion, break down into molecules. There is strong interest in significantly improving the quality of foods, especially nanocarriers, in order to improve the encapsulation efficiency of the carrier and to control the release rate under various stimulus conditions for target delivery by using biocompatibility materials and optimizing their size.

In this point of view, the designs of suitable nanocarriers grew in importance because nanomaterials could be highly toxic, have very low bioavailability, and require protection from rapid degradation and excretion. Such carriers generally need to be stable, biocompatible, and biodegradable, and have the ability to target specific digestion process.

The miniaturization of electronic devices coupled with advances in microscale manufacturing technology has prompted studies on increased thermal management and cooling performance in microchannels. S. A. Memon and colleagues analyzed these thermal performances of the water-based salt hydrate S44 nanoparticle (as the phase

change material) slurry flow through a microchannel heat sink. In this study, they suggested that the salt hydrate S44 would provide better thermal performance than lauric acid and provided a design guideline for manufacturing phase change material particles and microchannel heat sinks.

On the other hand, in the study by S. H. Lee et al., mushroom-shaped microstructure-based dry adhesives are expected to be applied in various fields, thanks to their unique properties, such as strong adhesive force, repeatability, durability, reversibility, and self-cleaning. However, in order for dry adhesives to be widely used, the efficiency of the production process needs to be increased. Until now, dry adhesives have been made by fabricating a silicon master using a complex surface micromachining process and then replicating thermosetting or UV-curable resins. S. H. Lee et al. introduced a method to continuously fabricate a mushroom-like microstructure by continuously fabricating a simple microstructure using a simple molding process and resin inking. The fabricated microstructures showed similar properties to general dry adhesives and showed adhesion of about 13 N/cm² to the smooth surface.

Besides, its nutraceuticals are a natural way to achieve a therapeutic outcome with minimal or no side effects. However, they are subject to degradation resulting from exposure to environmental factors such as humidity, oxygen, heat, light, and extreme pH. The biomembrane is one of the

important molecular assemblies that contribute in an essential way to the functioning of organelles and of biological cells at large. A systematic study of the “Membranome,” in addition to the genome and proteome, is expected to be achieved in the 21st century with considerable potential for biomedicine, bioengineering, biomaterials, and functional food engineering development. In addition, enzymes are produced by all living organisms, from microorganisms to plants and animals; enzymes are necessary for nearly all of life’s chemical breakdown of complex molecules into simpler ones which often results in a release of energy and the biochemical synthesis of complex substances with the energy storage.

In this context, biomembrane technology such as liposome presents exciting opportunities for food technologists in areas such as encapsulation and controlled release of food materials, as well as the enhanced bioavailability, stability, and shelf-life of sensitive ingredients.

Watanabe and colleagues explored the functional hydration behavior such as interrelation between hydration and molecular properties at lipid membrane interfaces. Common aspects of interfacial water can be obtained by overviewing fundamental functions and properties at different temporal and spatial scales. It is important to understand the hydrogen bonding and structural properties of water and to evaluate the individual molecular species having different hydration properties. Water molecules form hydrogen bonds with biomolecules and contribute to the adjustment of their properties, such as surface charge, hydrophilicity, and structural flexibility. In this review, the fundamental properties of water molecules and the methods used for the analyses of water dynamics are summarized. In particular, the interrelation between the hydration properties, determined by molecules, and the properties of molecules, determined by their hydration properties, are discussed using the lipid membrane as an example.

In the study by M. Hirose et al., the authors investigate the L-proline-catalyzed Michael addition reaction of *N*-[*p*(2-benzimidazolyl)phenyl]maleimide (BIPM) and acetone was employed because BIPM is reported to be a good substrate to monitor L-proline-catalyzed reactions through the fluorescence of the product. The effect of liposome membranes on this reaction was kinetically analyzed using fluorescence spectroscopy. The kinetics of the reaction were different from those of the constituent lipids of the liposomes. Zwitterionic 1,2-dipalmitoyl-*sn*-glycero-3-phosphocholine liposome, which is in the solid-ordered phase, had a better value of reaction rate, suggesting that the reaction rate constants of this reaction in liposome membrane systems could be regulated by the characteristics of the liposome membrane (i.e., the phase state and surface charge). Based on the results obtained, a plausible model of the L-proline-catalyzed Michael addition reaction was discussed. The obtained results provide us with an easily detectable method to assess the reactivity of L-proline in biological systems.

It is necessary to describe the current circumstances of nanotechnology utilized in the food sector in order to develop the novel functional foods and to present a

comprehensive perspective to food scientists embarking on research about nanotechnology.

The free enzyme is easily denatured under the conditions of strong acid or alkali in the process of degumming. Therefore, many scholars have been working on the nanocarrier material since the rise of immobilizing technology. A magnetic immobilized enzyme can be oriented to replace the traditional mechanical stirring under the external magnetic field, avoiding the loss of enzyme on the magnetic carrier caused by mechanical stirring to improve the catalytic efficiency of the immobilized enzyme. At the same time, it can be quickly separated from the reaction system and easy to operate. J. Yang et al. developed the nanomagnetic carrier ($\text{Fe}_3\text{O}_4\text{-SiO}_2\text{-p}(\text{glycidyl methacrylate, GMA})$) prepared by atom transfer radical polymerization and immobilized the free phospholipase C (PLC) to the nanomagnetic carrier. Phospholipids were successfully converted to 1,2-diacylglycerol in degumming process. The enzymatic properties of PLC- $\text{Fe}_3\text{O}_4\text{-SiO}_2\text{-p}(\text{GMA})$ showed that the tolerance pH range was widened and the tolerance temperature increased by 10°C.

In nanoemulsion-based oral delivery systems for functional lipophilic compounds, it is important to know how the interfacial membrane affects the stability of compounds incorporated into the emulsion for the prevention of lipid oxidation. J. Kim et al. investigated the influence of oxidants on the stability of α -tocopherol in model nanoemulsions and the role of interfacial membrane organized by nonionic emulsifiers (P10L, P10S, P20S, P23L, and P100S) because the structural and physicochemical properties of emulsifiers play important roles in the nanoemulsion stability and in the storage stability of functional compounds incorporated into the oil droplets. Although their data are still insufficient to generalize the influence of droplet interface characteristics on the oxidative stability of emulsified oils, it was an excellent example out of relevant studies.

In addition, H. Yu et al. described the current applications of nanotechnology in food science including flavor control, enhancement of bioavailability of bioactive compounds, and detection of deleterious substances in foods. Furthermore, they provided a well-organized overview of classification, preparative methods, and safety issues of nanomaterials for food science. Nanotechnology in foods has progressed year upon year as they described; however, further research is necessary to maximize the number of uses within the food industry. In particular, the safety concerns regarding the consumption of nanomaterials in foods must be addressed before the products are released to the market. Therefore, it is necessary to standardize test procedures to determine the impact of nanomaterials.

Whilst it is clear from the studies included in this special issue that many advances have been made in food engineering, there is a crucial key issue still to be overcome. That is, nanotechnology in foods has progressed year upon year; however, further research is necessary to maximize the number of uses within the food industry. In particular, the safety concerns regarding the consumption of nanomaterials in foods must be addressed before the products are released to the market. Therefore, it is necessary to standardize test

procedures to determine the impact of nanomaterials. Finally, regulations should be introduced and constructed that can ease consumer worry and enhance consumer acceptability.

Conflicts of Interest

The Editors declare that they have no conflicts of interest regarding the publication of this special issue.

Pahn-Shick Chang
Hiroshi Umakoshi
Hakjin Kim

Research Article

Synthesis and Application of Nanomagnetic Immobilized Phospholipase C

Yang Jiang,¹ Jing Du,² Honglin Tang,¹ Xin Zhang,¹ Wenbin Li,² Liqi Wang,³ Lianzhou Jiang,¹ and Dianyu Yu ¹

¹School of Food Science, Northeast Agricultural University, Harbin 150030, China

²The Key Laboratory of Soybean Biology in Chinese Ministry of Education, Northeast Agricultural University, Harbin 150030, China

³School of Computer and Information Engineering, Harbin University of Commerce, Harbin 150028, China

Correspondence should be addressed to Dianyu Yu; dyyu2000@126.com

Received 14 October 2018; Accepted 20 January 2019; Published 3 March 2019

Guest Editor: Hiroshi Umakoshi

Copyright © 2019 Yang Jiang et al. This is an open access article distributed under the Creative Commons Attribution License, which permits unrestricted use, distribution, and reproduction in any medium, provided the original work is properly cited.

The nanomagnetic carrier ($\text{Fe}_3\text{O}_4@/\text{SiO}_2@/\text{p}(\text{GMA})$) was prepared by atom transfer radical polymerization, and then, the free phospholipase C (PLC) was immobilized on it proved by the results of FT-IR analysis. The enzyme loading was 135.64 mg/g, the enzyme activity was 8560.7 U/g, the average particle size was 99.86 ± 0.80 nm, and the specific saturation magnetization was 16.00 ± 0.20 emu/g. PLC- $\text{Fe}_3\text{O}_4@/\text{SiO}_2@/\text{p}(\text{GMA})$ showed the highest activities at the pH of 7.5, and tolerance temperature raised to 65°C in soybean lecithin emulsion. Enzymatic degumming with PLC- $\text{Fe}_3\text{O}_4@/\text{SiO}_2@/\text{p}(\text{GMA})$ under the conditions of the enzyme dosage of 110 mg/kg, reaction temperature of 65°C, pH of 7.5, and reaction time of 2.5 h resulted in residual phosphorus of 64.7 mg/kg, 1,2-diacylglycerol (1,2-DAG) contents of 1.07%, and oil yield of 98.1%. Moreover, PLC- $\text{Fe}_3\text{O}_4@/\text{SiO}_2@/\text{p}(\text{GMA})$ still possessed more than 80% of its initial activity after 5 cycles.

1. Introduction

Soybean crude oil generally contains 3% of phospholipids. These need to be removed in the degumming process. The purpose of degumming removes colloidal impurities in crude oil improving the quality of it, building a good foundation for the subsequent processes [1, 2]. Phospholipids in soybean crude oil are divided into hydratable phospholipids (HPs) and nonhydratable phospholipids (NHPs). There are some differences in properties and removal process between them. HP is relatively easy to remove, while NHP is difficult to remove by water degumming [3]. In order to reduce the phosphorus content in crude oil, many factories add a large amount of phosphoric acid and alkali to remove the phospholipids, producing a lot of waste liquid, polluting the environment, and increasing the cost of oil degumming. However, enzymatic degumming effectively removes NHP from crude oil [4].

Phospholipases A_1 (PLA_1) cleaves the sn-1 ester bond of phospholipids that hydrolyzes NHP, but lysophospholipids

undergo transacylation decreasing its enzymatic hydrolysis efficiency during the hydrolysis of PLA_1 . Phospholipases A_2 (PLA_2) targets the sn-2 ester of phospholipids, but its enzyme activity is lower than PLA_1 and the free fatty acids produced by PLA_2 increase the acid value of soybean oil [5]. Phospholipase C (PLC) hydrolyzes the sn-3 phosphate ester bond on the glycerol side, yielding a 1,2-DAG that retains in the oil to improve oil yield and the free head group [6], so it has a good application prospect in enzymatic degumming.

The free enzyme is sensitive to temperature and pH and easily denatured under the conditions of strong acid or alkali in the process of degumming, thereby reducing the enzymatic efficiency of free enzyme. It is difficult to separate from the reaction system, and the purification procedure of it after separation is complex and expensive, which limits the application of free enzymes in oil degumming. These drawbacks can generally be overcome by immobilization. The immobilization of free enzyme improves its tolerance, stability, and easy separation from the product, and realizes the recovery and reuse of the enzyme [7]. Enzyme immobilization

methods mainly include entrapping, adsorption, covalent bonding, and cross-linking methods. The carrier materials of immobilized enzyme include natural polymer materials, synthetic polymer materials, inorganic materials, and composite materials.

As a part of immobilized enzyme, the structure and properties of carrier materials have great influence on the properties of immobilized enzyme. Therefore, many scholars have been working on the carrier material since the rise of immobilizing technology. Yu et al. found that PLA₁ was immobilized on different high molecular materials such as calcium alginate, calcium alginate-chitosan, and calcium alginate-gelatin and its catalytic performance was improved, but the viscosity of the reaction system increased due to the formation of oil residue. It brings difficulties to the separation of immobilized PLA₁ [8]. Magnetic polymer microspheres are a new type of functional biopolymer material. They are made up of magnetic materials and polymer materials, which can ensure the catalytic performance of free enzyme and the rapid separation of enzyme from the reaction system, having been widely studied. Magnetic materials generally include Fe₃O₄, CoFe₂O₄, Pt, Ni, and Co. Among them, Fe₃O₄ is widely studied. It combines with other modifiers to complete its surface modification so that new physical and chemical properties are more suitable for magnetic immobilization of enzymes. After magnetic immobilization of PLA₁ by Yu et al., the separation of magnetic immobilized enzyme from the reaction system was better than that of PLA₁ immobilized on polymer material [9]. Therefore, compared with polymer materials, magnetic polymer microspheres had more advantages in immobilizing enzyme.

The operational stability of the enzyme was generally improved after magnetic immobilization. Lipase and α -amylase were immobilized on magnetic carriers by Xie et al.; the thermal stability, pH stability, and storage stability of enzymes were significantly enhanced [10, 11]. Magnetic immobilized enzyme can be oriented to replace the traditional mechanical stirring under external magnetic field, avoiding the loss of enzyme on the magnetic carrier caused by mechanical stirring to improve the catalytic efficiency of immobilizing enzyme. At the same time, it can be quickly separated from the reaction system and is easy to operate. Cao et al. combined chitosan with magnetic material to immobilize papain. The results showed that the immobilized enzyme had high catalytic efficiency and was easy to separate [12]. Therefore, enzyme immobilized on a magnetic carrier can be applied to a magnetic fluidized bed, and it is easier to realize industrial continuous degumming [13].

At present, the study of PLC in oil mainly focuses on the application of free PLC in oil degumming. No article has studied the magnetic immobilization of PLC. This is the first report on magnetic immobilized PLC. In this work, a layer of SiO_x was coated on Fe₃O₄, and then, (3-aminopropyl)triethoxysilane (APTES) was used to modify the surface and attached to glycidyl methacrylate (GMA) polymer to prepare Fe₃O₄@SiO₂@p(GMA) magnetic carrier. The free PLC was immobilized on the carrier, and its characteristic absorption peak, morphological structure, particle size, and specific

saturation magnetization were characterized. The enzymatic characteristics of magnetic immobilized PLC were studied, and the effect of soybean oil degumming was also investigated. It provides a theoretical basis for the application of magnetic immobilized PLC in a magnetic fluidized bed.

2. Materials and Methods

2.1. Materials. PLC, with a phospholipase activity of 17000.2 U/g, was purchased from DSM (Shanghai, China). Soybean crude oil was provided by Jiusan Group (Harbin, China) with an original phosphorus content of 802.6 mg/kg. *p*-Nitrophenylphosphorylcholine (*p*-NPPC), phosphatidylcholine (PC), and 1,2-DAG with purities greater than 98% were purchased from Sigma Chemical Ltd. (St. Louis, MO, USA). All other analytical-grade reagents were from Sino-pharm Chemical Reagent Co., Ltd. (Shanghai, China).

2.2. Synthesis of Fe₃O₄@SiO₂@p(GMA). Fe₃O₄ nanoparticles were prepared by chemical coprecipitation [14], the silica-coating procedure was performed by the Deng et al. [15], and APTES-modified Fe₃O₄/SiO_x nanoparticles were made by Lei et al.'s method [16]. Preparation of Fe₃O₄@SiO₂@p(GMA) with reference to Lei et al. [16] and detailed steps are as follows: 2 g of Fe₃O₄/SiO_x-g-APTES were dispersed into 30 mL of toluene containing 4 mL of triethylamine under stirring in an ice bath. A solution of 4 mL chloroacetyl chloride and 8 mL toluene was added into the dispersoid after cooling the mixture to 0°C. The mixture was stirred for 10 h at room temperature. The nanoparticles were separated with a magnet, washed with toluene and ethanol, and then dried under vacuum. 0.5 g of the above-prepared particles was dispersed in 20 mL of dimethylformamide (DMF)/water (1:1, mL:mL). Nitrogen was pumped into the mixture to remove oxygen for 30 min, and then [GMA]/[CuCl]/[CuCl₂]/[2,2'-bipyridyl](100:1:0.2:2) was added. The mixture was stirred with 20 r/min at room temperature for 12 h and extracted thoroughly with acetone for 48 h after the reaction; then, the samples were vacuum-dried at room temperature for 24 h.

2.3. Immobilization of PLC. The epoxy group of Fe₃O₄@SiO₂@p(GMA) forms a covalent bond with the amino group on the PLC, completing the immobilization of the PLC [16]. 1.0 g Fe₃O₄@SiO₂@p(GMA) was immersed in phosphate buffer (0.1 mol/L, pH=7) at room temperature for 24 h. After magnetic separation, the magnetic carriers were transferred into PLC solution (0.02 g/mL, pH=7) and stirred at 55°C for 5 h. The magnetic immobilized PLC was separated and washed with phosphate buffer (0.1 mol/L, pH=7) three times to prepare PLC-Fe₃O₄@SiO₂@p(GMA). PLC-Fe₃O₄@SiO₂@p(GMA) was preserved at 4°C. The enzyme loading of PLC-Fe₃O₄@SiO₂@p(GMA) was detected as described by Soozanipour et al. [17].

2.4. Characterization. Fe₃O₄@SiO₂@p(GMA) and PLC-Fe₃O₄@SiO₂@p(GMA) were characterized by Fourier-

transform infrared spectrophotometer (FT-IR), X-ray diffraction (XRD), scanning electron microscope (SEM), laser particle size analyzer, and vibrating sample magnetometer (VSM).

2.5. Determination of PLC Activity. Refer to the method of Jiang et al. [18]. 1 U/mL of PLC was defined as the amount of enzyme solution needed to produce 1 nmol nitrophenol per minute by the hydrolysis of *p*-NPPC at the temperature of 36°C and the pH of 7.2. One hundred microliters of the PLC enzyme solution were added to 2 mL of *p*-NPPC solution, which contained 10 mmol/L *p*-NPPC, 250 mmol/L tris-HCl (pH 7.2), 60% sorbitol, and 1 mmol/L ZnCl₂, in a test tube. The tube was incubated at 37°C for 30 min. Substrate hydrolysis was quantified by measuring absorbance at 410 nm. The activity of PLC was calculated as follows:

$$\text{activity (U/mL)} = 1.3636 \times 10^3 \times \frac{A}{t}, \quad (1)$$

where *A* is the absorption value at 410 nm and *t* is the time (in minutes) used in the substrate hydrolysis reaction. The conversion factor 1.3636×10^3 was calculated based on the standard curve of nitrophenol.

2.6. Enzymatic Characteristics of Magnetic Immobilized PLC: Effect of pH and Temperature on the Relative Activity of Magnetic Immobilized PLC. Several 4 g/100 g soybean lecithin emulsions were prepared in 0.1 mol/L phosphate buffer with different pH values. The temperature was 55°C, and the amount of free PLC or PLC-Fe₃O₄@SiO₂@p(GMA) was 2.7 mg/kg or 110 mg/kg, respectively. The effect of pH, which in the range of 5.0–8.5, on the relative activity of free PLC and PLC-Fe₃O₄@SiO₂@p(GMA) was studied. The effect of temperature on the relative activity of free PLC and PLC-Fe₃O₄@SiO₂@p(GMA) was determined using a 4 g/100 g lecithin emulsion that was soluble in 0.1 mol/L phosphate buffer with the previously determined optimum pH at temperatures ranging from 40°C to 75°C. The highest activity measured over the range of pH and temperatures was designated as 100%, and the activities at other pH and temperatures were calculated as proportions of the highest activity.

2.7. Enzymatic Degumming Process. Crude soybean oil (100.0 g) was heated to 70°C in a water bath, and 0.13 mL of 45% citric acid solution was added under high shear rate (500 rpm) for 20 min. The temperature was decreased to optimum temperature, and a 4% (w/w) NaOH solution was added to adjust the mixture pH. 3 mL deionized water and 110 mg/kg PLC-Fe₃O₄@SiO₂@p(GMA) were added to crude soybean oil. The mixture was incubated with continuous stirring at 150 rpm for 2.5 h. After the reaction, the oil mixture was quickly centrifuged at 10,000 rpm for 10 min. The residual phosphorus content in the oil phase was determined according to Yu et al. [9]. The content changes of 1,2-DAG during reaction process were researched, and the method of determination was referenced [19]. The oil yield after degumming was calculated, and the formula is as follows:

$$\text{oil yield (\%)} = \frac{M_1}{M_2} \times 100\%, \quad (2)$$

where *M*₁ is the quality of oil after degumming, g; *M*₂ is the quality of crude soybean oil, g.

Reusability of PLC-Fe₃O₄@SiO₂@p(GMA) in the process of soybean crude oil degumming was also studied. PLC-Fe₃O₄@SiO₂@p(GMA) was washed with 0.1 mol/L phosphate buffer to its optimum pH to determine the relative enzyme activity after degumming. The ratio of the residual enzyme activity to the initial enzyme activity was the relative enzyme activity.

2.8. Statistical Analysis. All experiments were carried out in triplicate to allow for the calculation of means. Statistical analysis was performed with Origin 8.5 software (OriginLab Ltd., USA).

3. Results and Discussion

3.1. Immobilization of PLC. Fe₃O₄@SiO₂@p(GMA) carrier was prepared by atom transfer radical polymerization. The reaction conditions were reaction temperature 55°C, pH 7.0, and reaction time 5 h. The effect of free PLC dosage enzyme loading and enzyme activity was investigated. The results are shown in Figure 1. When the enzyme dosage was less than 15 mL, enzyme loading and enzyme activity increased with the increase of enzyme dosage. When the enzyme dosage was more than 15 mL, enzyme loading increased slowly and the enzyme activity decreased. If the enzyme loading was high enough, it was likely that some molecules may be packed together and near enough to interact with each other reducing enzyme activity [20]. So, the optimum enzyme dosage was 15 mL, the enzyme loading of Fe₃O₄@SiO₂@p(GMA) was 135.64 mg/g, and the enzyme activity of PLC-Fe₃O₄@SiO₂@p(GMA) was 8560.7 U/g.

3.2. Characterization by FT-IR Analysis and XRD Analysis. The FT-IR analysis results of Fe₃O₄@SiO₂@p(GMA) and PLC-Fe₃O₄@SiO₂@p(GMA) are presented in Figure 2(a). The FT-IR spectroscopy of Fe₃O₄@SiO₂@p(GMA) and PLC-Fe₃O₄@SiO₂@p(GMA) had characteristic absorption peaks at 579 cm⁻¹, 1091 cm⁻¹, 1637 cm⁻¹, and 3450 cm⁻¹, respectively. The absorption peaks at 579 cm⁻¹ belonged to the stretching vibration mode of FeO bonds in Fe₃O₄. The absorption peak presented at 1091 cm⁻¹ was the stretching vibration of Si-O-Si bonds. The absorption peaks presented at 1637 cm⁻¹ should be the stretching vibrations of -C=O bonds. The absorption peaks presented at 3450 cm⁻¹ were supposed to be the stretching vibration of -OH bonds. The absorption peaks of the PLC-Fe₃O₄@SiO₂@p(GMA) presented at near 1600 cm⁻¹ belonged to the amide band in protein [21]. It showed that the PLC was immobilized.

Fe₃O₄@SiO₂@p(GMA) and PLC-Fe₃O₄@SiO₂@p(GMA) were analyzed by XRD as shown in Figure 2(b). It is apparent that the diffraction pattern of Fe₃O₄@SiO₂@p(GMA) is close to PLC-Fe₃O₄@SiO₂@p(GMA). This revealed that free PLC immobilized on Fe₃O₄@SiO₂@p(GMA) did not lead to

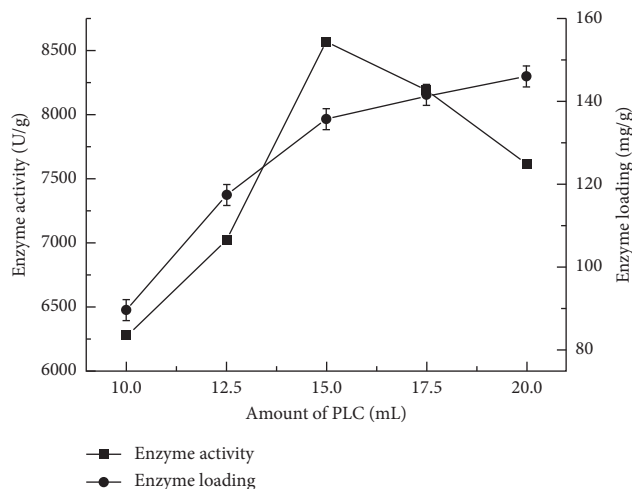


FIGURE 1: Effect of free PLC dosage on enzyme loading and enzyme activity. The reaction conditions were as follows: reaction temperature 55°C, pH 7.0, and reaction time 5 h. The optimum enzyme dosage was 15 mL, the enzyme loading of $\text{Fe}_3\text{O}_4@\text{SiO}_2@\text{p}(\text{GMA})$ was 135.64 mg/g, and the enzyme activity of $\text{PLC-Fe}_3\text{O}_4@\text{SiO}_2@\text{p}(\text{GMA})$ was 8560.7 U/g.

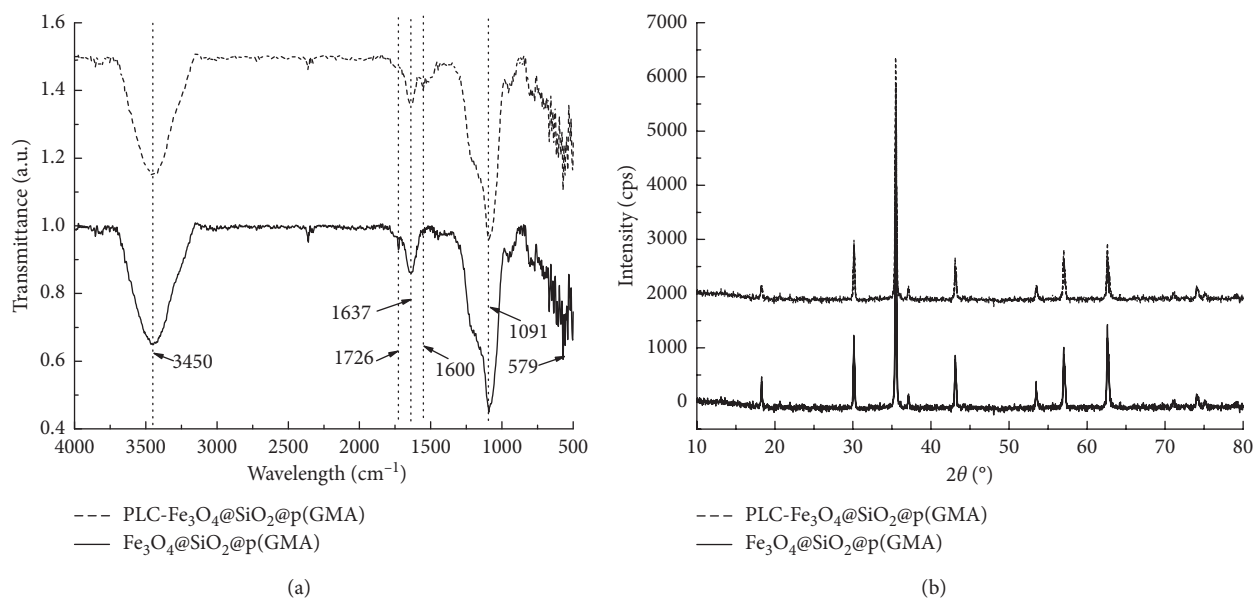


FIGURE 2: FT-IR spectrum analysis and XRD spectrum analysis. The FT-IR spectroscopy of $\text{Fe}_3\text{O}_4@\text{SiO}_2@\text{p}(\text{GMA})$ and $\text{PLC-Fe}_3\text{O}_4@\text{SiO}_2@\text{p}(\text{GMA})$ had characteristic absorption peaks at 579 cm^{-1} , 1091 cm^{-1} , 1637 cm^{-1} , and 3450 cm^{-1} , respectively. The absorption peaks presented at near 1600 cm^{-1} belonged to ester groups of phospholipase in the FT-IR spectroscopy of $\text{PLC-Fe}_3\text{O}_4@\text{SiO}_2@\text{p}(\text{GMA})$. The diffraction pattern of $\text{Fe}_3\text{O}_4@\text{SiO}_2@\text{p}(\text{GMA})$ was close to $\text{PLC-Fe}_3\text{O}_4@\text{SiO}_2@\text{p}(\text{GMA})$'s that no phospholipase crystal peak was found in it, proving phospholipase well-dispersed on carrier. (a) FT-IR spectrum analysis. (b) XRD spectrum analysis.

Fe_3O_4 crystal structure change. However, the intensity of diffraction peak of $\text{Fe}_3\text{O}_4@\text{SiO}_2@\text{p}(\text{GMA})$, immobilized with PLC, decreased, which was consistent with the decrease of XRD peak intensity of immobilized enzyme by Pandey et al. [22]. It shows that the interaction between $\text{Fe}_3\text{O}_4@\text{SiO}_2@\text{p}(\text{GMA})$ and PLC will have some influence on the structure of $\text{Fe}_3\text{O}_4@\text{SiO}_2@\text{p}(\text{GMA})$.

3.3. Morphological Structure and Particle Size Analysis. The morphologies of $\text{Fe}_3\text{O}_4@\text{SiO}_2@\text{p}(\text{GMA})$ and $\text{PLC-Fe}_3\text{O}_4@\text{SiO}_2@\text{p}(\text{GMA})$ were observed by SEM. The results are

shown in Figure 3(a). As shown in Figure 3(a), the ballability of $\text{Fe}_3\text{O}_4@\text{SiO}_2@\text{p}(\text{GMA})$ was good and the average size was 90 nm; however, some of them were agglomerated. The smaller the particle size of the nanocarrier is, the more conducive to the immobilization of enzyme was. $\text{PLC-Fe}_3\text{O}_4@\text{SiO}_2@\text{p}(\text{GMA})$ also had a good ballability, and the average particle size was about 105 nm as shown in Figure 3(b). Because $\text{PLC-Fe}_3\text{O}_4@\text{SiO}_2@\text{p}(\text{GMA})$'s surface was uneven, this phenomenon increased the surface area of it that loaded more PLC to increase the specific activity and at the same time, increased the chance of contact between enzymes and reactants, reducing the mass transfer resistance caused by

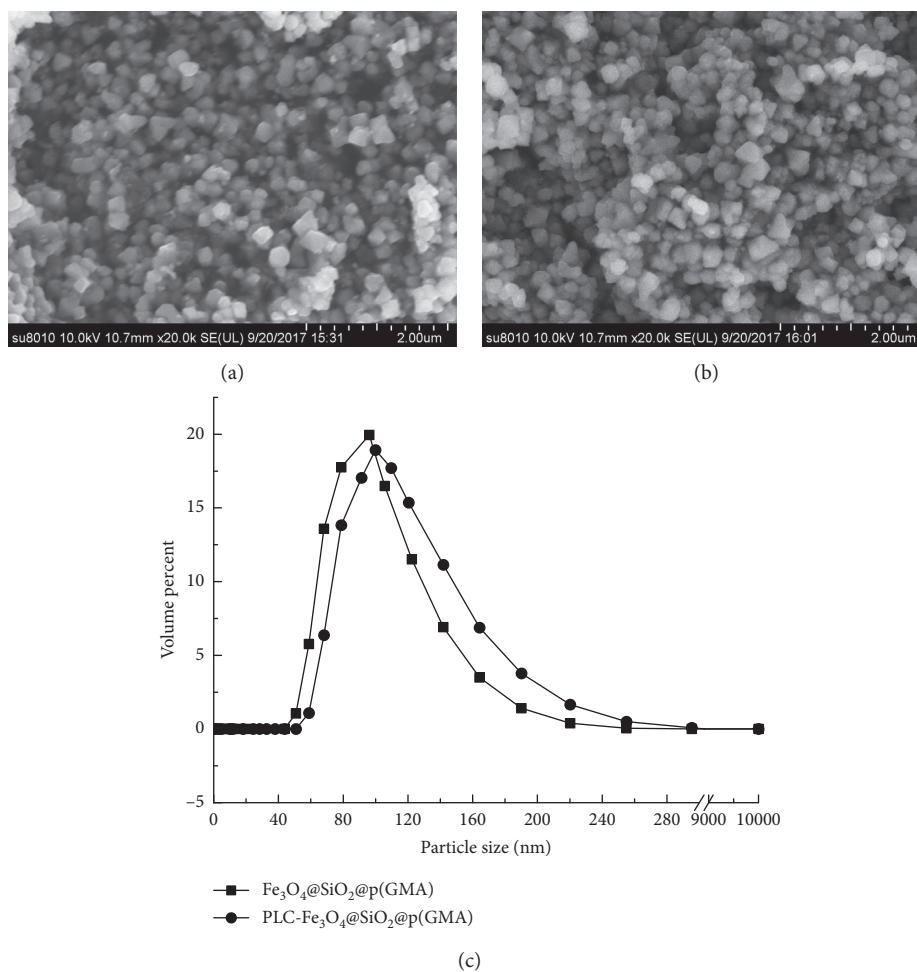


FIGURE 3: Scanning electron microscopy images of particles prepared and particle size analysis. In (a), the ballability of $\text{Fe}_3\text{O}_4@SiO_2@p(GMA)$ was good and the average size was 90 nm. In (b), SEM micrographs of $\text{PLC-Fe}_3\text{O}_4@SiO_2@p(GMA)$ also had a good ballability and the average particle size was about 105 nm. The average particle size of $\text{Fe}_3\text{O}_4@SiO_2@p(GMA)$ was 96.70 ± 1.00 nm, and the particle size distribution range was 55 to 255 nm. For $\text{PLC-Fe}_3\text{O}_4@SiO_2@p(GMA)$, the average particle size was 99.86 ± 0.80 nm and 90% of the particles were in the range of 58 to 295 nm. (a) $\text{Fe}_3\text{O}_4@SiO_2@p(GMA)$. (b) $\text{PLC-Fe}_3\text{O}_4@SiO_2@p(GMA)$. (c) Particle size analysis.

product accumulation to a certain extent [23]. Its average particle size was uniform and the diameter of it was larger than that of $\text{Fe}_3\text{O}_4@SiO_2@p(GMA)$, indicating that the immobilization effect of $\text{PLC-Fe}_3\text{O}_4@SiO_2@p(GMA)$ was fine.

Determination of particle size of $\text{Fe}_3\text{O}_4@SiO_2@p(GMA)$ and $\text{PLC-Fe}_3\text{O}_4@SiO_2@p(GMA)$ by using the laser particle size analyzer is shown in Figure 3(c).

When the laser passes through the moving particles, the light scattering will occur and the frequency of the scattering light will cause Doppler shift. The particle size can be calculated by measuring the spectrum half width of scattered light intensity. In the graph, the average particle size of the $\text{Fe}_3\text{O}_4@SiO_2@p(GMA)$ was 96.70 ± 1.00 nm, larger than the particle size measured by the SEM, the polydispersity index (PDI) was 0.245, and the particle size distribution range was 55 to 255 nm that had a wide range. The average particle size of $\text{PLC-Fe}_3\text{O}_4@SiO_2@p(GMA)$ had a concentrated distribution range. 90% of the particles were in the range of 58 to 295 nm. The average particle size was 99.86 ± 0.80 nm that was smaller than the particle size measured by SEM, and PDI

was 0.293. The number of particles between 60~80 nm, 80~100 nm, 100~120 nm, and 120~160 nm were 20%, 35%, 32%, and 14%, respectively, which showed that the particles were concentrated in the area with larger particle size. $\text{PLC-Fe}_3\text{O}_4@SiO_2@p(GMA)$ was a kind of nanoparticles as a result of its particle size [16].

3.4. Magnetic Analysis. Figure 4 shows that the specific saturation magnetization of $\text{Fe}_3\text{O}_4@SiO_2@p(GMA)$ and $\text{PLC-Fe}_3\text{O}_4@SiO_2@p(GMA)$ was analyzed by VSM. The specific saturation magnetization was found to be 19.70 ± 0.60 emu/g and 16.00 ± 0.20 emu/g for $\text{Fe}_3\text{O}_4@SiO_2@p(GMA)$ and $\text{PLC-Fe}_3\text{O}_4@SiO_2@p(GMA)$, respectively. The specific saturation magnetization of $\text{PLC-Fe}_3\text{O}_4@SiO_2@p(GMA)$ decreased, and it may be that PLC reduced the specific saturation magnetization of the carrier after immobilizing. However, they could be well magnetized under external magnetic field, which was conducive to regular movement in the magnetic reactor. Remanence and

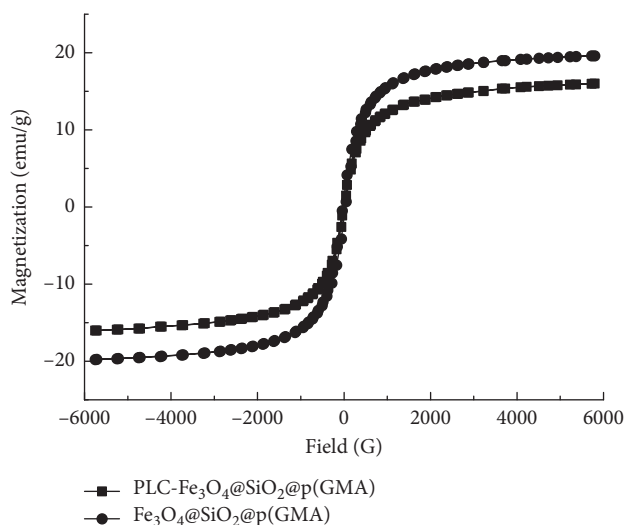


FIGURE 4: Magnetic hysteresis loop. The specific saturation magnetization was found to be 19.70 ± 0.60 emu/g and 16.00 ± 0.20 emu/g for $\text{Fe}_3\text{O}_4@SiO_2@p(GMA)$ and $\text{PLC-Fe}_3\text{O}_4@SiO_2@p(GMA)$, respectively.

coercivity of $\text{Fe}_3\text{O}_4@SiO_2@p(GMA)$ and $\text{PLC-Fe}_3\text{O}_4@SiO_2@p(GMA)$ were almost zero, resulting in them having no remanence and agglomeration when the external magnetic field was removed [24]. The results can realize redispersion and subsequent separation of $\text{PLC-Fe}_3\text{O}_4@SiO_2@p(GMA)$ in a magnetically fluidized bed.

3.5. Enzymatic Characteristics of Nanomagnetic Immobilized PLC: Effect of pH and Temperature on the Relative Activity of Nanomagnetic Immobilized PLC. The effect of pH on the relative activity of nanomagnetic immobilized PLC was determined, and the results are shown in Figure 5(a). As shown in Figure 5(a), the maximum relative activity of free PLC was obtained at pH 6.5 (12124.7 U/g). $\text{PLC-Fe}_3\text{O}_4@SiO_2@p(GMA)$ possessed maximum relative activity at pH 7.5 (7547.5 U/g) that retained more than 80% relative activity in the pH range of 6.0–8.5. So, the optimum pH was shifted, and the tolerance pH range was obviously wider than that of free PLC after immobilizing. Magnetic carriers attached to negative charges since a large number of carboxyl groups may have existed on the surface of $\text{Fe}_3\text{O}_4@SiO_2@p(GMA)$, attracted cations, including H^+ , and attached them to the surface of the carrier. As a result, the concentration of H^+ in the diffusion layer was higher than that in the surrounding solution. The pH in the external solution shifted to alkalinity in order to counteract the microenvironmental effect to make the enzyme show maximum activity. So, the optimum pH of $\text{PLC-Fe}_3\text{O}_4@SiO_2@p(GMA)$ has a shift toward the alkaline side, which also proves that PLC has been immobilized on $\text{Fe}_3\text{O}_4@SiO_2@p(GMA)$ [25]. This result is consistent with the migration direction of optimum pH after magnetic immobilization of PLA_2 by Qu et al. [26]. When pH was 7.5, the enzyme activity of $\text{PLC-Fe}_3\text{O}_4@SiO_2@p(GMA)$ was the highest, probably because the pH was close to its isoelectric point, which enhanced its

tolerance in the alkaline environment. It may also be that there was a sufficiently stable covalent bond between PLC and $\text{Fe}_3\text{O}_4@SiO_2@p(GMA)$ to resist the conformation change of PLC and to reduce the dissociation rate of PLC. When pH was greater than 7.5, the reduction of enzyme activity may be due to the abscission of PLC on the carrier. Accordingly, the optimum pH of $\text{PLC-Fe}_3\text{O}_4@SiO_2@p(GMA)$ was 7.5.

The effect of temperature on the relative activity of nanomagnetic immobilized PLC to hydrolyze soybean lecithin emulsions was determined, and the results are shown in Figure 5(b). The maximum relative activity of free PLC was at 55°C (11043.8 U/g), while that of $\text{PLC-Fe}_3\text{O}_4@SiO_2@p(GMA)$ was at 65°C (7693.8 U/g) that had more than 80% of the initial activity in the range of 50°C – 70°C . It demonstrated that immobilized PLC had a wider tolerance for temperature. Stability of immobilized enzyme depends on the immobilization strategy. Free PLC was connected with $\text{Fe}_3\text{O}_4@SiO_2@p(GMA)$ in covalent bond and changed the secondary structure of free PLC, increasing the rigidity of PLC structure, changing the conformation of immobilized enzyme that made it more suitable for contact with substrate, reducing the denaturant at high temperature, and improving its thermal stability [27, 28]. Defaei et al. immobilized α -amylase onto naringin functionalized MNPs that exhibited a good thermostability [29]. *Candida antarctica* lipase B was immobilized on $\text{Fe}_3\text{O}_4@SiO_2@p(GMA)$; its optimum temperature was increased by 5°C and had higher activities at a wider range of temperatures [30]. The results suggest that the optimum temperature of PLC is increased by 10°C through immobilizing.

3.6. Enzymatic Degumming Process. The content changes of residual phosphorus and 1,2-DAG in reaction are shown in Figure 6. Within 0–1.0 h, the content of residual phosphorus decreased rapidly and nevertheless, the content of 1,2-DAG increased rapidly. There was a slow reduction in residual phosphorus content, but 1,2-DAG content continued to increase at the same time when reaction time was from 1.0 h to 2.0 h. $\text{PLC-Fe}_3\text{O}_4@SiO_2@p(GMA)$ reacted in crude soybean oil for 2.0 h, and the residual phosphorus and 1,2-DAG were 64.7 mg/kg and 1.07%, respectively. The oil yield after degumming was 98.1%, which was about 1.0% higher than that of water degumming oil [18]. When the reaction time continued to prolong, the change of residual phosphorus and 1,2-DAG was not significant. The main reason was that $\text{PLC-Fe}_3\text{O}_4@SiO_2@p(GMA)$ hydrolyzed PC and phosphatidyl ethanolamines (PE) to produce 1,2-DAG in crude soybean oil at the beginning of reaction [31], and there was no remarkable change in residual phosphorus and 1,2-DAG on account of the substrate decreased gradually. As clearly seen here, $\text{PLC-Fe}_3\text{O}_4@SiO_2@p(GMA)$ can be applied to crude soybean oil degumming.

3.7. Reusability of Nanomagnetic Immobilized PLC in Degumming. Reusability of nanomagnetic immobilized PLC in degumming is shown in Figure 7. $\text{PLC-Fe}_3\text{O}_4@SiO_2@p(GMA)$ had 82.5% relative activity after 5 recycles.

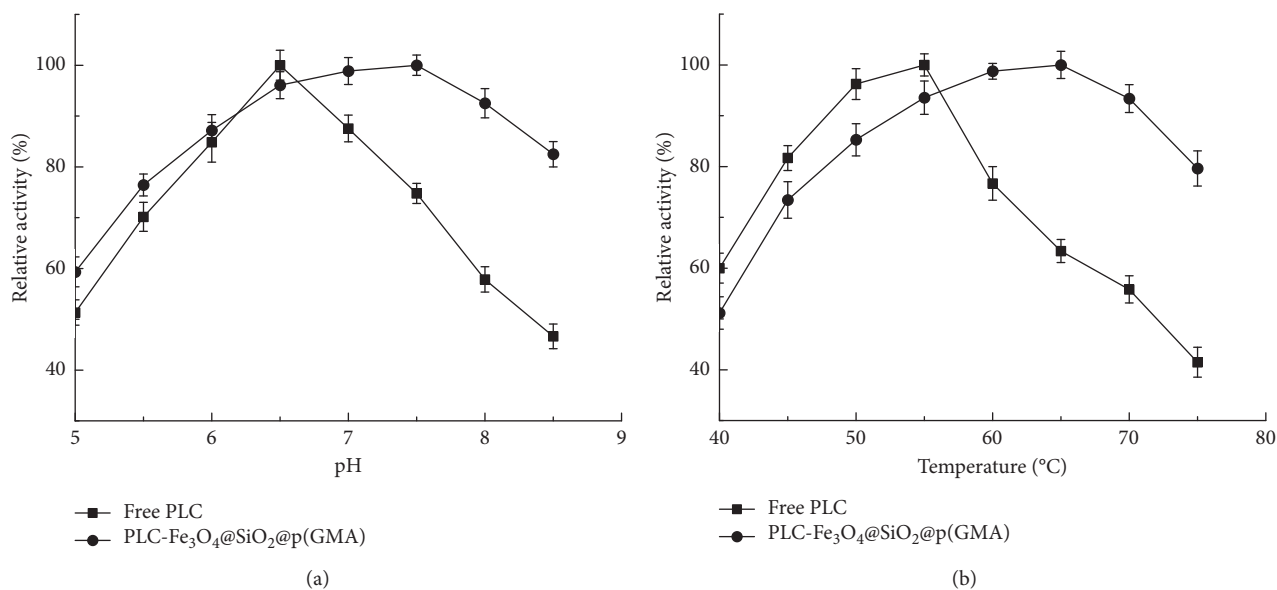


FIGURE 5: Effect of pH and temperature on the relative activity of free PLC and PLC-Fe₃O₄@SiO₂@p(GMA). Effect of pH on the relative activity of free PLC and PLC-Fe₃O₄@SiO₂@p(GMA) using soybean lecithin emulsions as a substrate at 55°C for 2 h. The optimum pH of PLC was 7.5 after immobilizing. Effect of temperature on the relative activity of free PLC and PLC-Fe₃O₄@SiO₂@p(GMA), hydrolyzing soybean lecithin emulsions, was determined within pH 6.5 and 7.5 for 2 h. The optimum temperatures of PLC were increased by 10°C through immobilizing. The data were reproduced three times, and error bars indicate standard deviations. (a) Effect of pH on the relative activity of free PLC and PLC-Fe₃O₄@SiO₂@p(GMA). (b) Effect of temperature on the relative activity of free PLC and PLC-Fe₃O₄@SiO₂@p(GMA).

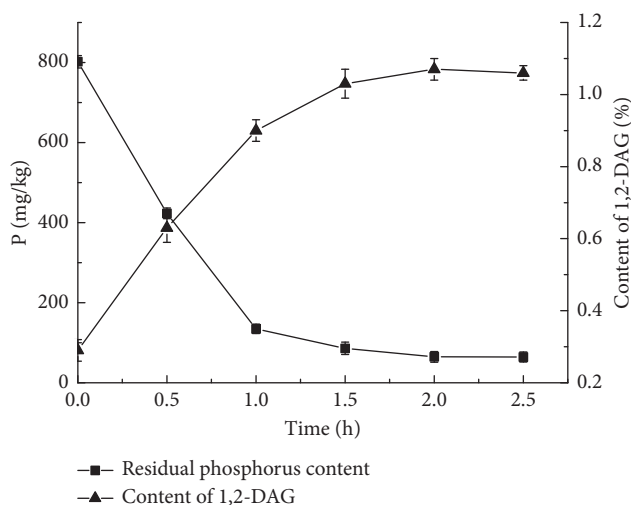


FIGURE 6: Content of residual phosphorus and 1,2-DAG changes with time. The degumming conditions were at 65°C and pH of 7.5 for 2.5 h in crude soybean oil. After reacting for 2.0 h in crude soybean oil, the residual phosphorus and 1,2-DAG were 64.7 mg/kg and 1.07%, respectively. The data were reproduced three times, and error bars indicate standard deviations.

The relative activity of it was 73.4% after 6 recycles. So, PLC-Fe₃O₄@SiO₂@p(GMA) exhibited a good reusability. The research of Segato et al. showed that immobilized cellobiohydrolase D (CelD) retained more than 80% of its initial activity after 4 consecutive reuses [32]. The loss of enzyme activity was attributed to the denaturation of PLC in the hydrolysis environment, followed by the mechanical agitation and the collision of magnetic immobilized PLC during

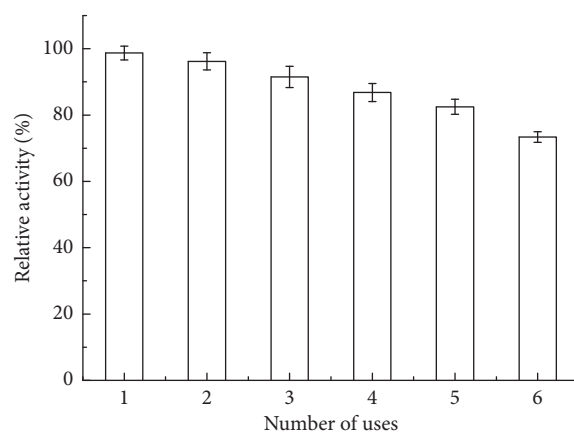


FIGURE 7: Reusability of PLC-Fe₃O₄@SiO₂@p(GMA), using crude soybean oil as a substrate at 65°C with a pH of 7.5 for 2.5 h. PLC-Fe₃O₄@SiO₂@p(GMA) retained 82.5% relative activity after 5 recycles. The data were reproduced three times, and error bars indicate standard deviations.

hydrolysis, which resulted in the PLC shedding off the carrier [9]. So, magnetic immobilized enzymes have good reusability.

4. Conclusion

In this experiment, the free PLC was immobilized on the Fe₃O₄@SiO₂@p(GMA) carrier. PLC-Fe₃O₄@SiO₂@p(GMA) had high enzyme loading and enzyme activity. It had a good ballability as nanoparticles and high specific saturation magnetization that quickly separated from the reaction

system. The enzymatic properties of PLC-Fe₃O₄@SiO₂@p(GMA) showed that the tolerance pH range was widened and the tolerance temperature increased by 10°C. Phospholipids were converted to 1,2-DAG in degumming, which increased the oil yield about 1.0%, and PLC-Fe₃O₄@SiO₂@p(GMA) had good reusability. So, PLC-Fe₃O₄@SiO₂@p(GMA) can be used in the degumming of oil in a magnetic fluidized bed.

Data Availability

The data used to support the findings of this study are available from the corresponding author upon request.

Conflicts of Interest

The authors declare that there are no conflicts of interest regarding the publication of this paper.

Acknowledgments

This work was supported by a grant from the National Natural Science Foundation of China (NSFC), "Study on the Mechanism of Nanomagnetic Enzyme Hydrolysis of Soybean Oil by Multi-Effect Orientation and Biosynthesis of Functional Lipids" (No. 31571880). This work was also supported by a grant from "Rice Bran High-Value Steady-State Processing Technology and Intelligent Equipment Research and Demonstration" (No. 2018YFD0401101).

References

- [1] G. Gofferjé, J. Motulewicz, A. Stäbler, T. Herfellner, U. Schweiggert-Weisz, and E. Flöter, "Enzymatic degumming of crude jatropha oil: evaluation of impact factors on the removal of phospholipids," *Journal of the American Oil Chemists' Society*, vol. 91, no. 12, pp. 2135–2141, 2014.
- [2] C. Elena, S. Cerminati, P. Ravasi et al., "B. cereus phospholipase C engineering for efficient degumming of vegetable oil," *Process Biochemistry*, vol. 54, pp. 67–72, 2017.
- [3] X. Jiang, M. Chang, X. Wang, Q. Jin, and X. Wang, "A comparative study of phospholipase A₁ and phospholipase C on soybean oil degumming," *Journal of the American Oil Chemists' Society*, vol. 91, no. 12, pp. 2125–2134, 2014.
- [4] D. L. Lamas, D. T. Constenla, and D. Raab, "Effect of degumming process on physicochemical properties of sunflower oil," *Biocatalysis and Agricultural Biotechnology*, vol. 6, pp. 138–143, 2016.
- [5] D. L. Lamas, G. H. Crapiste, and D. T. Constenla, "Changes in quality and composition of sunflower oil during enzymatic degumming process," *LWT-Food Science and Technology*, vol. 58, no. 1, pp. 71–76, 2014.
- [6] M. S. Piel, G. H. J. Peters, and J. Brask, "Chemoenzymatic synthesis of fluorogenic phospholipids and evaluation in assays of phospholipases A, C and D," *Chemistry and Physics of Lipids*, vol. 202, pp. 49–54, 2017.
- [7] D. Yu, Y. Ma, L. Jiang et al., "Stability of soybean oil degumming using immobilized phospholipase A₂," *Journal of Oleo Science*, vol. 63, no. 1, pp. 25–30, 2014.
- [8] D. Yu, L. Jiang, Z. Li, J. Shi, J. Xue, and Y. Kakuda, "Immobilization of phospholipase A₁ and its application in soybean oil degumming," *Journal of the American Oil Chemists' Society*, vol. 89, no. 4, pp. 649–656, 2011.
- [9] D. Yu, Y. Ma, S. J. Xue, L. Jiang, and J. Shi, "Characterization of immobilized phospholipase A₁ on magnetic nanoparticles for oil degumming application," *LWT-Food Science and Technology*, vol. 50, no. 2, pp. 519–525, 2013.
- [10] W. Xie and J. Wang, "Enzymatic production of biodiesel from soybean oil by using immobilized lipase on Fe₃O₄/poly(styrene-methacrylic acid) magnetic microsphere as a biocatalyst," *Energy & Fuels*, vol. 28, no. 4, pp. 2624–2631, 2014.
- [11] H. Guo, Y. Tang, Y. Yu, L. Xue, and J.-q. Qian, "Covalent immobilization of α-amylase on magnetic particles as catalyst for hydrolysis of high-amylose starch," *International Journal of Biological Macromolecules*, vol. 87, pp. 537–544, 2016.
- [12] S.-L. Cao, X.-H. Li, W.-Y. Lou, and M.-H. Zong, "Preparation of a novel magnetic cellulose nanocrystal and its efficient use for enzyme immobilization," *Journal of Materials Chemistry B*, vol. 2, no. 34, pp. 5522–5530, 2014.
- [13] K. Atacan, B. Çakıroğlu, and M. Özacar, "Improvement of the stability and activity of immobilized trypsin on modified Fe₃O₄ magnetic nanoparticles for hydrolysis of bovine serum albumin and its application in the bovine milk," *Food Chemistry*, vol. 212, pp. 460–468, 2016.
- [14] H. Meng, Z. Zhang, F. Zhao, T. Qiu, and J. Yang, "Orthogonal optimization design for preparation of Fe₃O₄ nanoparticles via chemical coprecipitation," *Applied Surface Science*, vol. 280, no. 8, pp. 679–685, 2013.
- [15] Y.-H. Deng, C.-C. Wang, J.-H. Hu, W.-L. Yang, and S.-K. Fu, "Investigation of formation of silica-coated magnetite nanoparticles via sol-gel approach," *Colloids and Surfaces A: Physicochemical and Engineering Aspects*, vol. 262, no. 1–3, pp. 87–93, 2005.
- [16] L. Lei, X. Liu, Y. Li, Y. Cui, Y. Yang, and G. Qin, "Study on synthesis of poly(GMA)-grafted Fe₃O₄/SiO_x magnetic nanoparticles using atom transfer radical polymerization and their application for lipase immobilization," *Materials Chemistry & Physics*, vol. 125, no. 3, pp. 866–871, 2011.
- [17] A. Soozanipour, A. Taheri-Kafrani, and A. Landarani Isfahani, "Covalent attachment of xylanase on functionalized magnetic nanoparticles and determination of its activity and stability," *Chemical Engineering Journal*, vol. 270, pp. 235–243, 2015.
- [18] X. Jiang, M. Chang, Q. Jin, and X. Wang, "Application of phospholipase A₁ and phospholipase C in the degumming process of different kinds of crude oils," *Process Biochemistry*, vol. 50, no. 3, pp. 432–437, 2015.
- [19] P. Ravasi, M. Braia, F. Eberhardt et al., "High-level production of Bacillus cereus phospholipase C in Corynebacterium glutamicum," *Journal of Biotechnology*, vol. 216, pp. 142–148, 2015.
- [20] L. Fernandez-Lopez, S. G. Pedrero, N. Lopez-Carrobles, B. C. Gorines, J. J. Virgen-Ortiz, and R. Fernandez-Lafuente, "Effect of protein load on stability of immobilized enzymes," *Enzyme and Microbial Technology*, vol. 98, pp. 18–25, 2017.
- [21] J. Yang, L. Zhong, B. Zou et al., "Spectroscopic investigations on the binding of persimmon tannin to phospholipase A₂ from Chinese cobra (Naja naja atra)," *Journal of Molecular Structure*, vol. 1008, pp. 42–48, 2012.
- [22] G. Pandey, D. M. Munguambe, M. Tharmavaram et al., "Halloysite nanotubes-an efficient 'nano-support' for the immobilization of α-amylase," *Applied Clay Science*, vol. 136, pp. 184–191, 2017.
- [23] L. Zhang and Y. Sun, "Poly(carboxybetaine methacrylate)-grafted silica nanoparticle: a novel carrier for enzyme

- immobilization," *Biochemical Engineering Journal*, vol. 132, pp. 122–129, 2018.
- [24] F. Guo, Q. Zhang, B. Zhang, H. Zhang, and L. Zhang, "Preparation and characterization of magnetic composite microspheres using a free radical polymerization system consisting of DPE," *Polymer*, vol. 50, no. 8, pp. 1887–1894, 2009.
- [25] Q. Liu, Y. Hua, X. Kong, C. Zhang, and Y. Chen, "Covalent immobilization of hydroperoxide lyase on chitosan hybrid hydrogels and production of C6 aldehydes by immobilized enzyme," *Journal of Molecular Catalysis B: Enzymatic*, vol. 95, pp. 89–98, 2013.
- [26] Y. Qu, L. Sun, X. Li et al., "Enzymatic degumming of soybean oil with magnetic immobilized phospholipase A₂," *Lebensmittel-Wissenschaft & Technologie*, vol. 73, pp. 290–295, 2016.
- [27] A. Sanchez, J. Cruz, N. Rueda et al., "Inactivation of immobilized trypsin under dissimilar conditions produces trypsin molecules with different structures," *RSC Advances*, vol. 6, no. 33, pp. 27329–27334, 2016.
- [28] M. Y. Arica, "Immobilization of polyphenol oxidase on carboxymethylcellulose hydrogel beads: preparation and characterization," *Polymer International*, vol. 49, no. 7, pp. 775–781, 2000.
- [29] M. Defaei, A. Taheri-Kafrani, M. Miroliaei, and P. Yaghmaei, "Improvement of stability and reusability of α -amylase immobilized on naringin functionalized magnetic nanoparticles: a robust nanobiocatalyst," *International Journal of Biological Macromolecules*, vol. 113, pp. 354–360, 2018.
- [30] D. Yu, X. Zhang, D. Zou et al., "Immobilized CALB catalyzed transesterification of soybean oil and phytosterol," *Food Biophysics*, vol. 13, no. 2, pp. 208–215, 2018.
- [31] C. Elena, P. Ravasi, S. Cerminati, S. Peiru, M. E. Castelli, and H. G. Menzella, "Pichia pastoris, engineering for the production of a modified phospholipase C," *Process Biochemistry*, vol. 51, no. 12, pp. 1934–1944, 2016.
- [32] F. Segato, M. Wilkins, R. Prade et al., "Cellulase immobilization on superparamagnetic nanoparticles for reuse in cellulosic biomass conversion," *AIMS Bioengineering*, vol. 3, no. 3, pp. 264–276, 2016.

Research Article

Detection of L-Proline-Catalyzed Michael Addition Reaction in Model Biomembrane

Masanori Hirose, Shigenori Sugisaki, Keishi Suga , and Hiroshi Umakoshi 

Division of Chemical Engineering, Graduate School of Engineering Science, Osaka University, 1-3 Machikaneyama-cho, Toyonaka, Osaka 560-8531, Japan

Correspondence should be addressed to Hiroshi Umakoshi; umakoshi@cheng.es.osaka-u.ac.jp

Received 3 October 2018; Revised 26 December 2018; Accepted 10 January 2019; Published 26 February 2019

Academic Editor: Josefina Pons

Copyright © 2019 Masanori Hirose et al. This is an open access article distributed under the Creative Commons Attribution License, which permits unrestricted use, distribution, and reproduction in any medium, provided the original work is properly cited.

A method to detect the L-proline- (L-Pro-) catalyzed Michael addition reaction in model biomembranes has been established, using *N*-[*p*(2-benzimidazolyl)phenyl]maleimide and acetone as reactants. The effect of liposome membranes on this reaction was kinetically analyzed using fluorescence spectroscopy. The kinetics of the reaction were different from those of the constituent lipids of the liposomes. Zwitterionic 1,2-dipalmitoyl-*sn*-glycero-3-phosphocholine liposome, which is in the solid-ordered phase, had a better value of reaction rate, suggesting that the reaction rate constants of this reaction in liposome membrane systems could be regulated by the characteristics of the liposome membrane (i.e., the phase state and surface charge). Based on the results obtained, a plausible model of the L-Pro-catalyzed Michael addition reaction was discussed. The obtained results provide us with an easily detectable method to assess the reactivity of L-Pro in biological systems.

1. Introduction

L-Proline (L-Pro) is one of the principle amino acids that are the building blocks of proteins. L-Pro is known to elucidate various kinds of physiological activities though its interference in the metabolic pathway, such as in the enhancement of growth of epidermal cells, activation of collagen biosynthesis, repair of damaged collagen, and moisture of the stratum corneum [1]. Considering these physiological activities, the use of L-Pro as a possible key material in food engineering has become significant.

As another significant aspect of L-Pro, it is gaining attention as an organocatalyst [2, 3]. With respect to safety and high efficiency, the use of L-Pro will prove beneficial in industrial processes, such as in the manufacture of medicine and food. Barbas and coworkers have reported many examples of L-Pro-catalyzed reactions, especially focusing on enantioselectivity [4–6]. The L-Pro-catalyzed reaction is usually achieved through the formation of the “enamine” intermediate, between L-Pro and the ketone substrate. It is known that most of reported reactions have been carried out

in the polar solvent, e.g., dimethyl sulfoxide (DMSO), but not in the high-polar solvent such as water, owing to the stability of the enamine intermediate. Considering the use of L-Pro in food engineering, it is thought that there could be some risks of the side reaction induced by L-Pro, as a less polar (hydrophobic) environment would exist in a biological system (e.g., in the interior of a biomembrane).

Recent studies have also focused on the use of self-assembly systems in organic synthesis because self-assemblies enable insoluble materials dispersed in aqueous media [7]. The liposome, a vesicular envelope composed of a phospholipid bilayer membrane, is known as a model of biomembranes. It can also be utilized as a platform of organic synthesis in aqueous media [8–11]. The liposome surface properties can be customized by modifying the lipid composition [12]. The combined use of small molecules with liposomes would lead to a cooperative alteration in the membrane properties, which can contribute to providing improved functions such as chiral recognition [13]. While the liposome structure has to be disrupted to recover the reaction product for its analysis, the use of the fluorescent

reactant, for example, *N*-[*p*(2-benzimidazolyl)phenyl]maleimide (BIPM) [14], enables us to directly determine the reaction rate constant.

Previously, we have observed that L-amino acids, including L-Pro, can bind onto liposomal membranes [13]. Thereby, the L-Pro-catalyzed reactions can proceed on liposome membranes in aqueous media [9, 11]. However, some challenges are still encountered in directly monitoring the kinetics of L-Pro-catalyzed reactions in the aqueous medium because the product is basically analyzed after extraction and purification. In this study, the L-Pro-catalyzed Michael addition reaction of BIPM and acetone was employed because BIPM is reported to be a good substrate to monitor L-Pro-catalyzed reactions through the fluorescence of the product [14]. The effect of liposome membranes on this reaction was kinetically analyzed using fluorescence spectroscopy. Based on the results obtained with previous findings, finally, a plausible model of the L-Pro-catalyzed Michael addition reaction was discussed. The obtained results provide an easily detectable method to assess the risk of L-Pro in biological systems.

2. Materials and Methods

2.1. Materials. 1,2-Dipalmitoyl-*sn*-glycero-3-phosphocholine (DPPC: C16:0, zwitterionic), 1,2-dioleoyl-*sn*-glycero-3-phosphocholine (DOPC: C18:1, zwitterionic), and 1,2-dipalmitoyl-3-trimethylammonium-propane (DPTAP: C16:0, cationic) were purchased from Avanti Polar Lipids, Inc. (Alabaster, AL, USA). L-Proline (L-Pro) and D-Proline were purchased from Peptide Institute (Osaka, Japan). *N*-[*p*(2-benzimidazolyl)phenyl]maleimide (BIPM) was purchased from Tokyo Chemical Industry co., Ltd. (Tokyo, Japan). Other chemicals were purchased from Wako Pure Chemical Industry Ltd. (Osaka, Japan) and were used as received.

2.2. Liposome Preparation. Liposomes were prepared based on literature [9]. In brief, a chloroform solution of lipids was dried in a round-bottom flask by using a rotary evaporator. The lipid film was dissolved in chloroform, and then the solvent was removed. The obtained lipid thin film was kept in a vacuum chamber for at least three hours, to remove the solvent completely. The dried lipid film was hydrated with ultrapure water at 60°C. The liposome suspension was frozen at -80°C for 15 min and was thawed at 60°C for 15 min. This freeze-thaw cycle was repeated for five times. The liposome suspension was finally treated by using the extrusion device (Lipofast; Avestin Inc., Ottawa, Canada), with two layers of polycarbonate membranes with a mean pore diameter of 100 nm. The size distributions of liposomes were determined by dynamic light scattering (DLS, Zetasizer Nano ZS, Malvern Panalytical, Grovewood Rd, UK). The average size of DPPC liposome just after preparation was 172.9 nm (PDI: 0.224). The average sizes of acetone added liposomes after 0 and 2 h were 143.3 and 247.3 nm, respectively, revealing that the addition of acetone resulted in only small influences on the liposome structures.

2.3. Kinetics of L-Pro-Catalyzed Reaction in DMSO/Water System. L-Pro-catalyzed Michael addition of BIPM (BIPM: 28.9 μg (0.1 μmol)) with acetone (0.2 mL (2.7 mmol)) was conducted in DMSO or aqueous solution. L-Pro-catalyzed reaction was initiated by adding 10 μl of stock solution of BIPM (10 mM) in acetonitrile (CH₃CN)/DMSO (1/1 v/v) mixture and 10 μl of stock solution of L-Pro in water (0–8 mM) and acetone (200 μl) to 780 μl of DMSO or aqueous solution. The reaction was carried out in a quartz cell for measurement without stirring. The background fluorescence (before the reaction) was weak enough, and the increased fluorescence intensities were measured by the fluorescence spectrophotometer FP-8500 (JASCO, Tokyo, Japan) at 25°C. The samples were excited with 315 nm and measured at 362 nm. The reaction kinetic was considered by first-order kinetics, and the reaction rate constant, *k*, was determined by following equation:

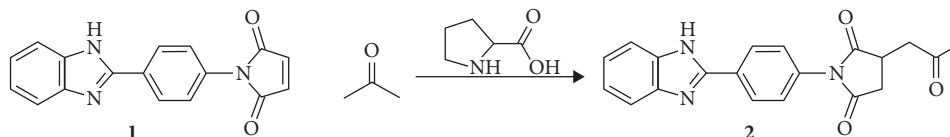
$$-\ln\left(1 - \frac{\Delta I}{\Delta I_{\max}}\right) = kt, \quad (1)$$

where ΔI and ΔI_{\max} represent the fluorescence at arbitral time (*t*) and the final fluorescence intensity, respectively. The products were analyzed by HPLC (Waters 1500 HPLC System (Waters, Milford, MA, USA) equipped with the ODS2 column (25 cm) (GL Science Inc., Tokyo, Japan)). Mobile phase was prepared with CH₃CN/0.1% aqueous trifluoroacetic acid (15 : 85) at a flow rate of 1.0 mL/min, with detection at 310 nm. The retention times of BIPM and product are 30.1 and 28.9 min, respectively.

2.4. L-Pro-Catalyzed Reaction in Liposome Membrane. L-Pro-catalyzed reaction in the liposome membrane was initiated by adding 10 μl of stock solution of BIPM (5 mM) in CH₃CN/DMSO (1/1 v/v) mixture and acetone (200 μl) to a 790 μl of mixture of liposome and L-Pro. A mixture of liposome and L-Pro was preincubated by mixing 780 μl of the liposome membrane (5 mM) and 10 μl of L-Pro stock solution of water (100 mM). The reaction was carried out in 5 ml of the screw vial with stirring and light shielding. A sample for fluorescence measurement was prepared by diluting the reaction solution 50-fold with water. HPLC analyses were carried out as described above.

3. Results and Discussion

3.1. L-Pro-Catalyzed Reaction in DMSO and Water. BIPM is reported to be a good molecular probe to monitor the L-Pro-catalyzed reaction because its product shows fluorescence [14]. First, the L-Pro-catalyzed Michael addition reaction of BIPM and acetone (Scheme 1) was performed in DMSO. In the available literature, the reaction rate of the Michael addition reaction of BIPM and acetone, catalyzed by L-Pro, has been reported as 0.005 μM/min [14]. The 24-hour incubation period could be long enough to reach saturation in these reaction media. Figure 1 shows the fluorescence spectra of the products obtained in DMSO and water with an incubation period of 24 hours. The emission peak wavelength of the product could be dependent on the



SCHEME 1: Michael addition reaction of BIPM and acetone: (1) BIPM; (2) product.

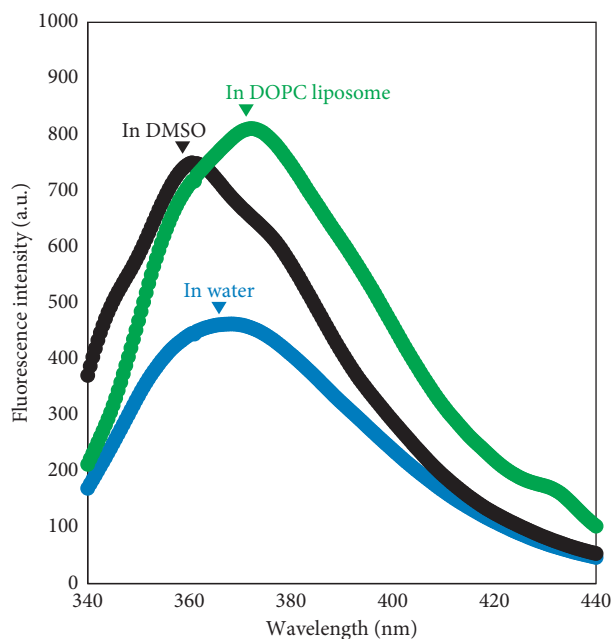


FIGURE 1: Fluorescence spectra of the products in DMSO, in water, and in DOPC liposome systems.

solvent; the wavelengths in DMSO and water were 360 nm and 368 nm, respectively. In the 1,2-dioleoyl-*sn*-glycero-3-phosphocholine (DOPC) liposome system, the emission peak was observed at 372 nm and the fluorescence intensity was slightly higher than that obtained in water. The fluorescent properties of the products are further discussed in Section 3.4. These results revealed that the product can emit strong fluorescence in these media.

In general, the L-Pro-catalyzed Michael reaction is faster in DMSO [3, 9]. The dependence of amount of the catalyst in this reaction was then investigated by varying the amount of L-Pro. Figure 2(a) shows the time course of the fluorescence intensity at different concentrations of L-Pro in DMSO. The reaction rate constants (k) were calculated based on first-order kinetics (equation (1)) (Figure 2(b)), suggesting that the reaction could proceed by following first-order kinetics, because the reaction rate and amount of L-Pro (catalyst) were almost in a linear relationship at L-Pro concentrations below $40 \mu\text{M}$.

To investigate the effect of solvent polarity, the reaction was further conducted in the system of DMSO/water mixture. Figure 3 shows the time course of the fluorescence intensities, wherein the fluorescence intensities were monitored at 362 nm. The presence of water significantly decreased the reaction rate. In general, the enamine formation can be inhibited by the solvent water [4]. It is suggested that water molecules also play an inhibitory role in this reaction. Common to the reaction mechanisms of the

L-Pro-catalyzed reactions, the formation of the enamine intermediate is the key to achieve efficiency and enantioselectivity [2, 3, 15], whereby the water molecules could decrease the stability of the enamine intermediate. During the formation of the enamine of L-Pro and acetone, unstable intermediates can be formed [16]. When the reaction is carried out in liposome membranes, such intermediates could be stabilized by interaction with phospholipid molecules [11]. These results clearly indicate that the efficiency of the L-Pro-catalyzed reaction of BIPM and acetone can be inhibited in an aqueous solution, owing to the lack of hydrophobic (dehydrated) environment. The reactions catalyzed by D-Proline (D-Pro) were also investigated, but the catalytic activity of D-Pro might be lower than that of L-Pro (Figure 3). In most cases, L-Pro and D-Pro show similar catalytic performances except for the enantioselectivity of the product [17]. However, in some examples, the yield of the product differed depending on the proline structure [18]. In the case of direct asymmetric aldol reaction between *p*-nitrobenzaldehyde (*p*NBA) and acetone, the D-Pro derivative drastically decreased the reaction yield [2]. The carboxyl group of L-Pro also produced a good yield [2]. It is assumed that L-Pro can improve the reactivity of the enamine intermediate, suggesting that the enamine composed by L-Pro (or its derivatives) shows higher reactivity as compared to D-Pro derivatives, but further determinations are needed to investigate their differences. In addition, as D-Pro is hardly adsorbed onto liposomes [13], it was difficult to perform the D-Pro-catalyzed reactions at the liposome membrane. In this study, the L-Pro-catalyzed Michael addition reactions of BIPM and acetone are further investigated in the following sections.

3.2. Coexistence Effect of Liposome Membrane L-Pro-Catalyzed Reaction in an Aqueous Solution. The coexistence effect of the liposome membrane on the L-Pro-catalyzed reaction of BIPM and acetone was investigated in water. Although L-Pro is a water-soluble molecule, it has been reported that L-Pro can be adsorbed onto the liposome surface by incubation for 48 hours [13]. After L-Pro was preincubated with the DPPC liposome for 24 or 48 hours, the Michael addition reaction was initiated by adding BIPM and acetone. Figure 4(a) shows the fluorescence spectra of the products at different incubation times. In the case of 24-hour preincubation, the spectra were not changed significantly, indicating that the reaction did not proceed. On the contrary, after 48-hour preincubation, the fluorescence intensities were drastically increased, showing that the L-Pro-catalyzed reaction of BIPM and acetone was achieved in the aqueous medium when the liposome was coexisting. The adsorption

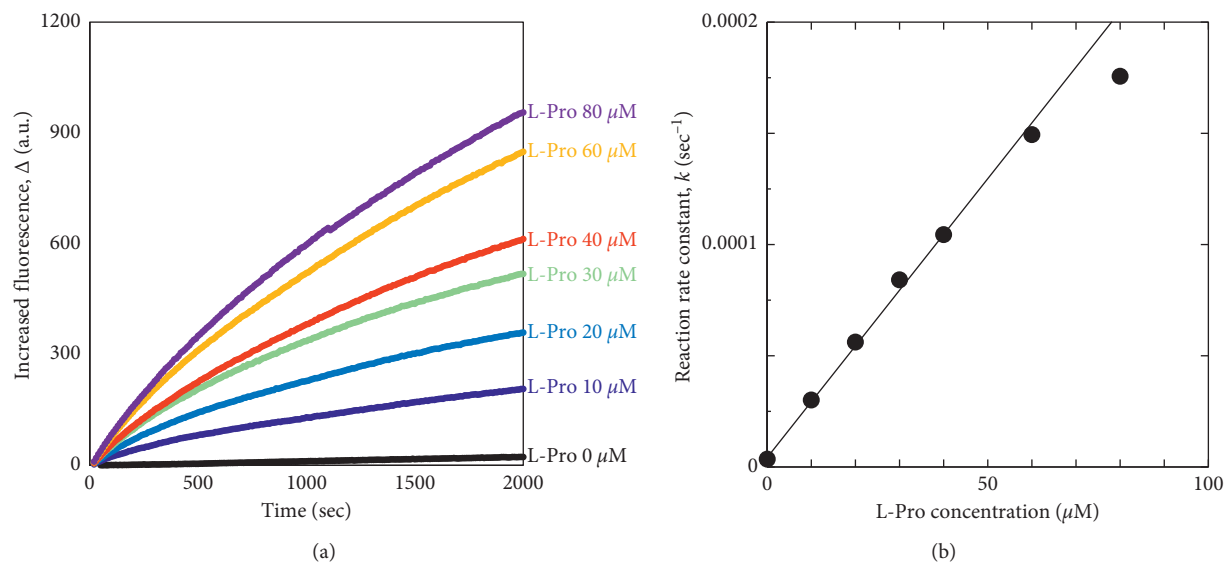


FIGURE 2: (a) Time course of the fluorescent intensity from the reaction product, at different L-Pro concentrations. (b) Relationship between L-Pro concentration and reaction rate constant.

amounts of L-Pro onto liposomes were approximately 10% of the total L-Pro—8.3% for the DOPC liposome, 10.8% for the DPPC liposome, and 11.4% for the DPPC/DPTAP liposome, at 48-hour incubation. We assume that only the adsorbed L-Pro possesses high catalytic activity, whereas the unadsorbed L-Pro can behave as free L-Pro. Although we have not estimated the L-Pro adsorption amount at 24 hours, in almost all cases, the adsorption amount at 24 hours is less than 20% of the maximum adsorption amount (at 48 hours). Considering these results and findings, the adsorption amounts of L-Pro could be estimated as $<100 \mu\text{M}$ for 48 hour preincubation and $<20 \mu\text{M}$ for 24-hour preincubation. This could be the reason why the reaction rate constants in liposome systems turn out to be lower than those in the DMSO solvent.

Figure 4(b) shows the time course of the fluorescence intensity, showing that the k value at 48-hour preincubation was five times higher than that of 24 hour preincubation. It has been reported that the L-amino acid adsorption did not proceed until 24 hours and then dramatically proceeded within 24- to 48 hour preincubation [13], in which the liposome surface properties could be varied by the adsorption of L-amino acids and then concerted binding could be initiated. The obtained results show that the Michael addition reaction of BIPM and acetone was promoted by the L-Pro that was adsorbed onto the membrane surface. Considering the facts that (1) water molecules principally inhibit the L-Pro-catalyzed reaction and (2) the liposome membrane provides a hydrophobic environment in the aqueous medium, the L-Pro-catalyzed reactions can be carried out in an aqueous medium, owing to the presence of the liposome membranes. The potential roles of the liposome membrane are to carry the hydrophobic reactant (BIPM) in the interior region of the membrane and to accumulate reactants and a catalyst in the dehydrated environment.

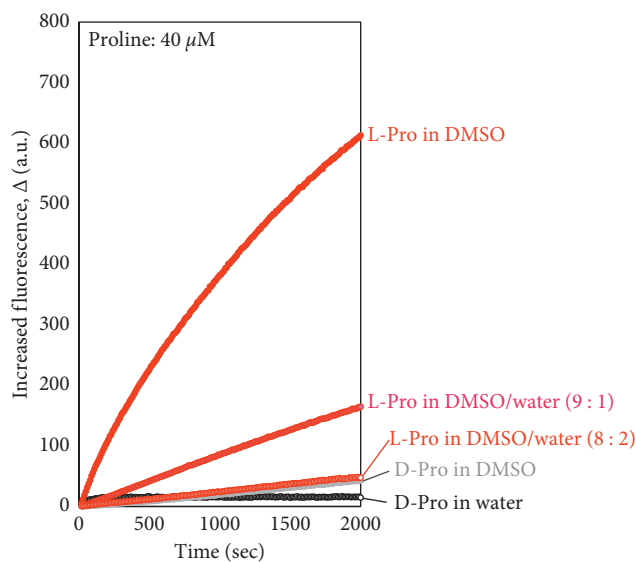


FIGURE 3: L-Pro-catalyzed Michael addition reaction of BIPM and acetone in DMSO/water solutions.

3.3. Effect of Type of Liposome Membrane on the L-Pro-Catalyzed Reaction. Biological membranes consist of various kinds of lipids and proteins. Among the naturally occurring zwitterionic phospholipids, DOPC and 1,2-dipalmitoyl-*sn*-glycero-3-phosphocholine (DPPC) were selected to investigate the effect of membrane properties on this reaction. At room temperature, DOPC and DPPC liposomes are in the fluid state (liquid-disordered, L_d , phase) and rigid state (solid-ordered, s_o , phase), respectively. It is also reported that the cationic liposome DPPC/DPTAP (1,2-dipalmitoyl-3-trimethylammonium-propane) can improve the L-Pro-catalyzed Michael addition reaction [9]. After L-Pro preincubation for 48 hours, the reaction of BIPM and acetone was carried out in the presence of the abovementioned liposomes (Figure 5). The initial reaction

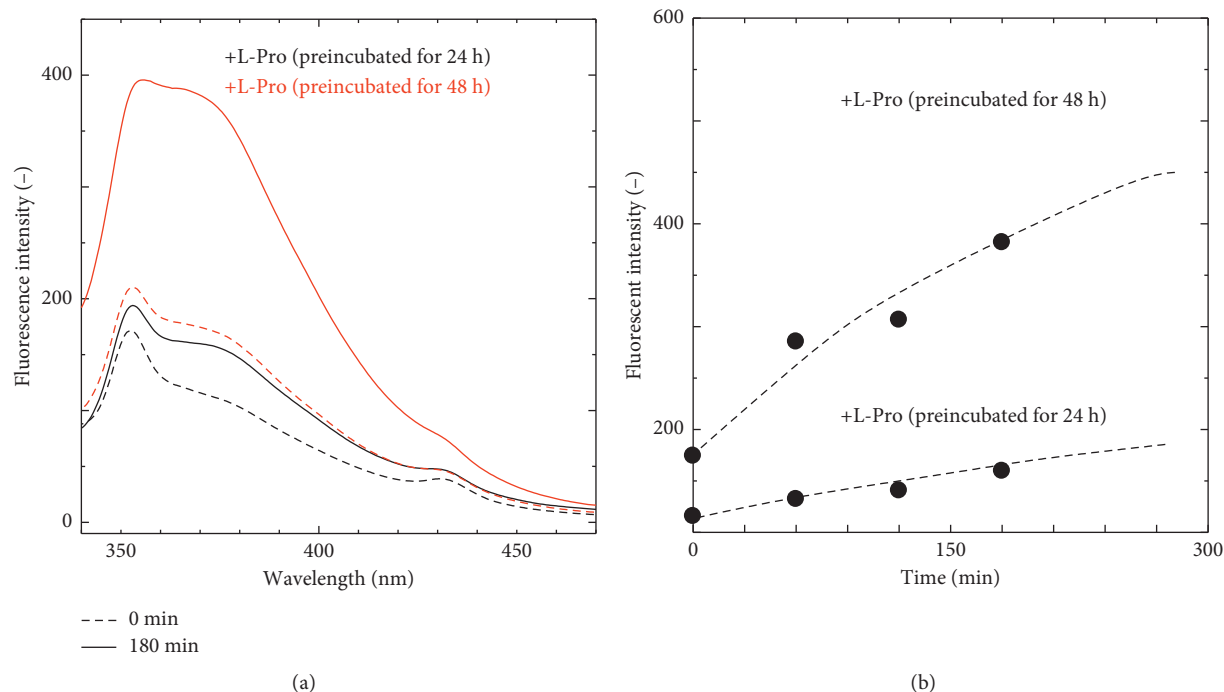


FIGURE 4: Coexistence effect of DPPC liposomes on L-Pro-catalyzed Michael addition reaction of BIPM and acetone: (a) fluorescence spectra of products; (b) time course of fluorescence emission peaks at 370 nm. L-Pro was preincubated with DPPC liposome for 24 hours and 48 hours, before initiation of the reaction.

rate was herein analyzed by the slope of the approximately straight line of the plot of fluorescence intensity at 372 nm against time, as the fluorescence intensity increased proportionally with time. The initial reaction rate in DPPC (s_o phase) was 2.5 times higher than that in DOPC (L_d phase). Furthermore, the addition of cationic DPTAP decreased the initial reaction rate, although both the DPPC and DPPC/DPTAP liposomes are in rigid membrane states (s_o phases) [9].

The membrane surface of the DPPC liposome is known to be in a dehydrated state as compared to that of the DOPC membrane [9], which could be favorable to stabilize the enamine intermediate of L-Pro and acetone. In addition, the “ordered” state of the DPPC membrane could contribute to promote the adsorption of the L-amino acid (including L-Pro), whereas L-amino acid adsorption can decrease when the membrane is in disordered states [13]. The adsorption of L-Pro was slightly increased by the positively charged liposomes [9], whereas the membrane property differences between DPPC and DPPC/DPTAP could be negligible. Thus, the inhibitory effect of the DPTAP on the reaction could be because of the positive charge of the membrane. Furthermore, only the positively charged molecules (e.g., propranolol) adsorbed onto the negatively charged liposomes [19]. It is assumed that L-Pro could preferentially adsorb onto the membrane in the s_o phase, in which the less hydrophobic environment contributes both to the adsorption of L-Pro and to the promotion of the Michael addition reaction.

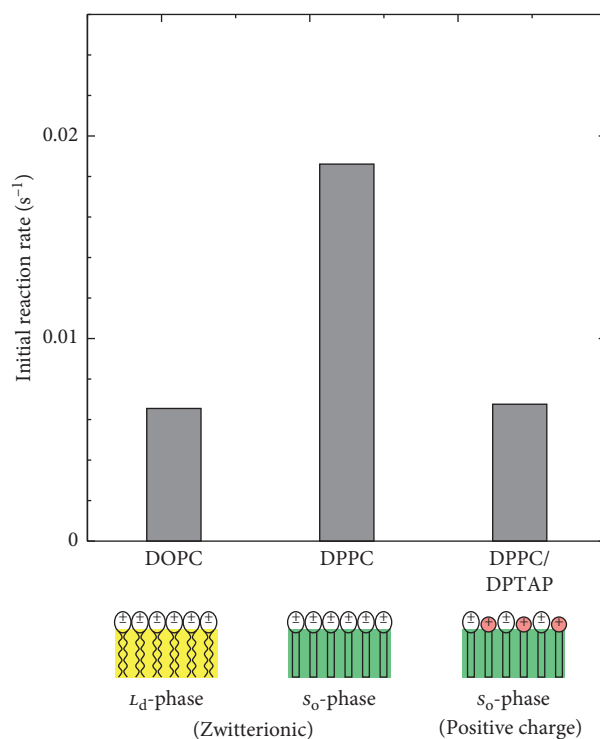


FIGURE 5: Comparison of the liposome phase state and initial reaction rate.

3.4. Plausible Model of L-Pro-Catalyzed Michael Addition Reaction of BIPM and Acetone in Liposome Membrane. Based on the abovementioned results, a plausible model of the L-Pro-catalyzed Michael addition reaction is discussed. To

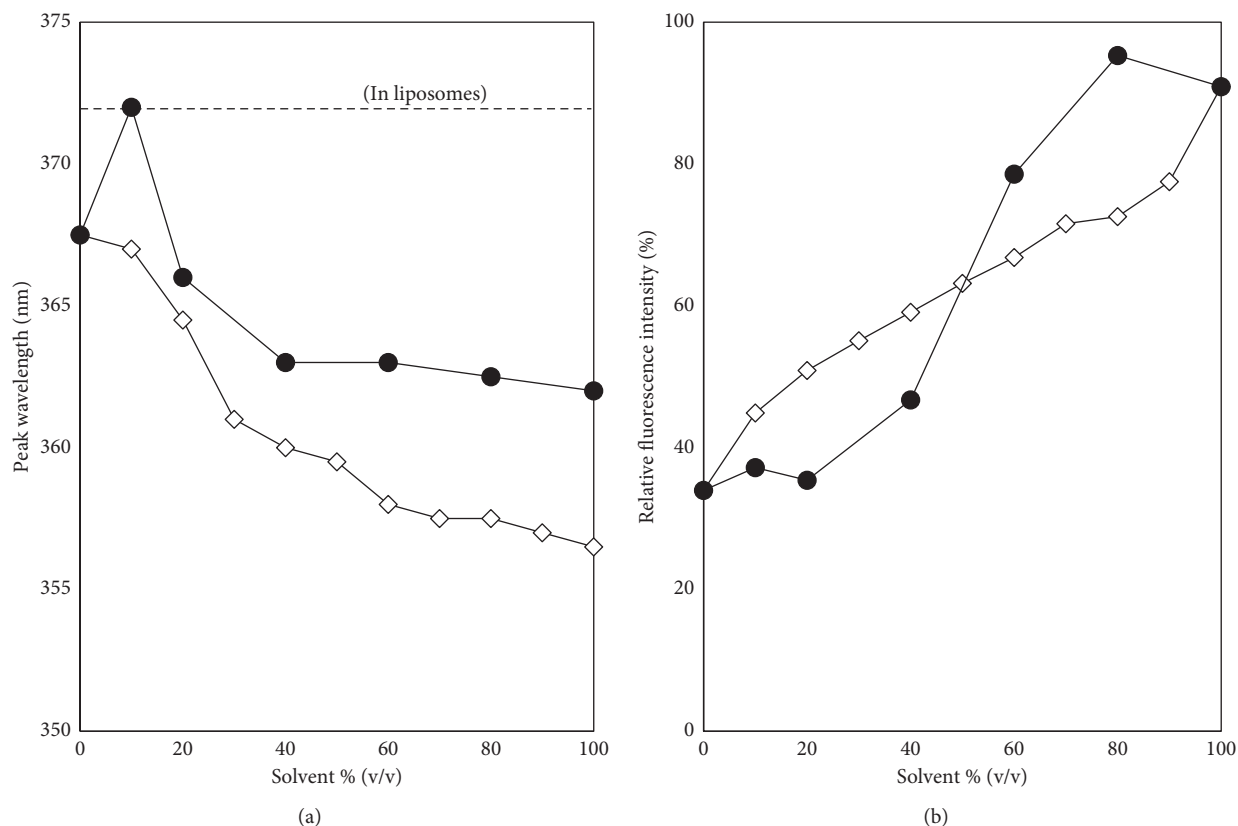


FIGURE 6: Emission peak wavelength (a) and relative emission peak intensity (b) of the reaction products in 1,4-dioxane/water mixtures (open diamond) and in DMSO/water mixtures (closed circle).

assess the location of the product in the liposome membrane, the peak shift of the emission fluorescence of the reaction product was analyzed in various kinds of solvents with different polarities. In the existing literature, it has been reported that the fluorescence intensity of the product in DMSO was slightly higher (~1.6 times) than that in water [14]. To verify the solvatochromism of the product, the product recovered in DMSO solvents after 24 hour incubation was transferred into DMSO/water mixtures for further analysis of its fluorescence. Figure 6(a) shows the emission peak wavelength of the reaction product in both 1,4-dioxane/water systems and DMSO/water systems. The emission peaks gradually redshifted as the water ratio increased. In the liposome systems, the emission peaks were observed at 368.5 nm (we confirmed the emission peaks with three isolated data from DOPC and DPPC). This suggests that the products generated in the liposome tend to locate at the hydrophilic part (near the lipid head groups) although the emission peaks were broader in the liposome systems. The emission peak intensities were decreased in proportion to the water ratio (Figure 6(b)). The fluorescence intensity of the product in water decreased to 40%. In contrast, the presence of water in the reaction mixture drastically inhibited the reaction (Figure 3), suggesting that the formation of the enamine intermediate of L-Pro and acetone could be the key to promote this reaction. The DMSO environment is suitable to stabilize enamine [2, 3], and a

similar effect can be obtained by utilizing the liposome membrane [9, 11].

The possible locations of the molecules related to this reaction are summarized in Figure 7. L-Pro, the enamine intermediate, and acetone could be basically localized at the interface region, near the phosphate and glycerol groups; therefore, the enamine intermediate could be stably trapped there. The reaction could be completed by the attack of the enamine intermediate to BIPM, which could be located in a more hydrophobic region—near the hydrocarbon chains of lipids. Similarly, the reactants *trans*- β -nitrostyrene (*t* β NS) and *p*NBA can be estimated to be located at the hydrophobic site [9, 11]. The obtained results and previous findings suggest that the enamine intermediate, composed of L-Pro and acetone, could preferentially locate in the hydrophobic region of the liposome membrane, which successfully promotes the L-Pro-catalyzed reactions. The efficiency and enantioselectivity can be varied, preferably depending on the property of the reactant—*t* β NS would provide high enantioselectivity; *p*NBA would provide high conversion but low enantioselectivity. For BIPM, although the conversion was lower, the reaction kinetics was directly analyzed in the aqueous medium, revealing that the L-Pro-catalyzed Michael addition of BIPM and acetone was surely performed in the liposomal membrane.

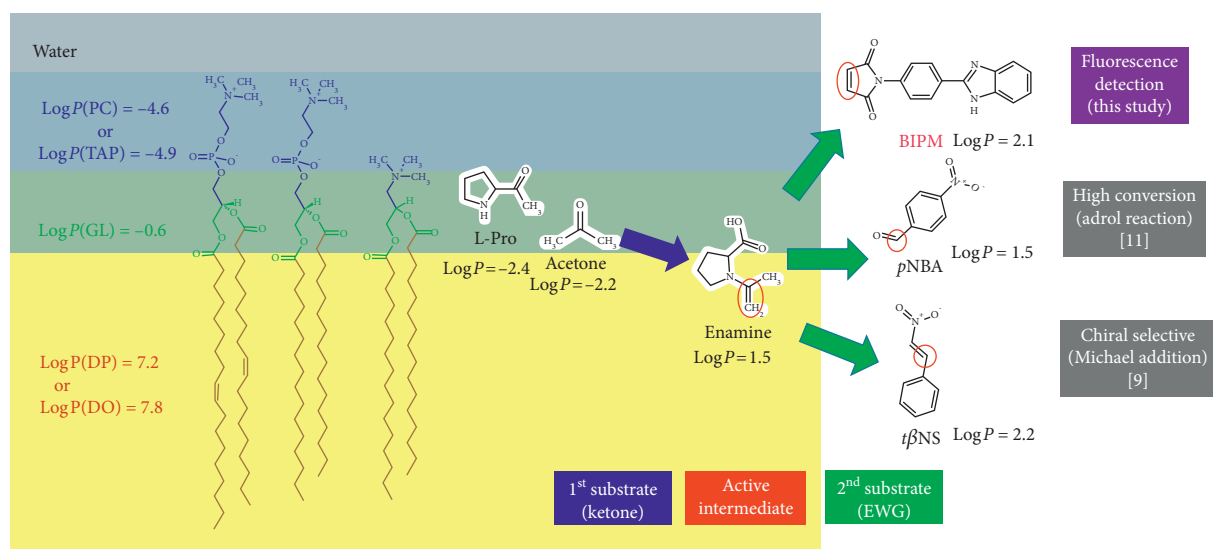


FIGURE 7: Schematic illustration of the location of the molecules related to the L-Pro-catalyzed Michael addition reaction in liposome membranes.

4. Conclusions

The kinetics of the L-Pro-catalyzed Michael addition reaction of BIPM and acetone were analyzed by using fluorescence spectroscopy. The composition of liposomes could be a controlling factor in this reaction—the zwitterionic DPPC liposome displayed the highest reaction rate constant among the liposomes tested in this work. From the point of view of green chemistry, organic synthesis in aqueous media provides various benefits. On the contrary, in food science and engineering fields, our findings provide a warning that the L-Pro distributed into biomembranes (hydrophobic environment) can react with ketones, which might lead to unexpected and inconvenient chemical reactions in the human body. The ketones can be produced by lipid oxidation in biomembranes; thus, ketones in biomembranes would be reactive in the presence of L-Pro, which might result in unexpected products. Thus, *in situ* detection of the L-Pro-catalyzed reactions is necessary. The obtained results provide us with an easily detectable method to assess the risk of L-Pro in biological systems, which can be detected using BIPM as a donor reactant in the L-Pro-catalyzed Michael addition reaction.

Abbreviations

L-Pro:	L-Proline
DMSO:	Dimethyl sulfoxide
BIPM:	<i>N</i> -[<i>p</i> (2-Benzimidazolyl)phenyl]maleimide
DPPC:	1,2-Dipalmitoyl- <i>sn</i> -glycero-3-phosphocholine
DOPC:	1,2-Dioleoyl- <i>sn</i> -glycero-3-phosphocholine
DPTAP:	1,2-Dipalmitoyl-3-trimethylammonium-propane
T_m :	Phase transition temperature
MLV:	Multilamellar vesicle
LUV:	Large unilamellar vesicle
CH ₃ CN:	Acetonitrile
D-Pro:	D-Proline
<i>p</i> NBA:	<i>p</i> -Nitrobenzaldehyde

L _d :	Liquid disordered
s _o :	Solid ordered
<i>t</i> βNS:	<i>trans</i> -β-Nitrostyrene.

Data Availability

The data used to support the findings of this study are included within the article.

Conflicts of Interest

The authors declare that there are no conflicts of interest regarding the publication of this paper.

Acknowledgments

This work was supported by the JSPS Grant-in-Aid for Scientific Research A (26249116), Challenging Exploratory Research (T15K142040), and Sasakawa Scientific Research Grant from the Japan Science Society (29-336). We thank Dr. Takaaki Ishigami and Dr. Yukihiro Okamoto (Graduate School of Engineering Science, Osaka University) for their constructive comments and technical support.

References

- [1] P. Li and G. Wu, "Roles of dietary glycine, proline, and hydroxyproline in collagen synthesis and animal growth," *Amino Acids*, vol. 50, no. 1, pp. 29–38, 2017.
- [2] B. List, R. A. Lerner, and C. F. Barbas, "Proline-catalyzed direct asymmetric aldol reactions," *Journal of American Chemical Society*, vol. 122, no. 10, pp. 2395–2396, 2000.
- [3] B. List, P. Pojarliev, and H. J. Martin, "Efficient proline-catalyzed Michael additions of unmodified ketones to nitro olefins," *Organic Letters*, vol. 3, no. 16, pp. 2423–2425, 2001.
- [4] N. Mase, K. Watanabe, H. Yoda, K. Takabe, F. Tanaka, and C. F. Barbas, "Organocatalytic direct Michael reaction of ketones and aldehydes with β-nitrostyrene in brine," *Journal*

- of *American Chemical Society*, vol. 128, no. 15, pp. 4966-4967, 2006.
- [5] K. Sakthivel, W. Notz, T. Bui, and C. F. Barbas, "Amino acid catalyzed direct asymmetric aldol reactions: a bioorganic approach to catalytic asymmetric carbon-carbon bond-forming reactions," *Journal of the American Chemical Society*, vol. 123, no. 22, pp. 5260-5267, 2001.
- [6] T. Bui and C. F. Barbas, "A proline-catalyzed asymmetric Robinson annulation reaction," *Tetrahedron Letters*, vol. 41, no. 36, pp. 6951-6954, 2000.
- [7] A. E. C. Palmqvist, "Synthesis of ordered mesoporous materials using surfactant liquid crystals or micellar solutions," *Current Opinion in Colloid & Interface Science*, vol. 8, no. 2, pp. 145-155, 2003.
- [8] F. Iwasaki, K. Suga, and H. Umakoshi, "Pseudo-interphase of liposome promotes 1,3-dipolar cycloaddition reaction of benzonitrile oxide and N-ethylmaleimide in aqueous solution," *Journal of Physical Chemistry B*, vol. 119, no. 30, pp. 9772-9779, 2015.
- [9] M. Hirose, T. Ishigami, K. Suga, and H. Umakoshi, "Liposome membrane as a platform for the L-pro-catalyzed Michael addition of trans- β -Nitrostyrene and acetone," *Langmuir*, vol. 31, no. 47, pp. 12968-12974, 2015.
- [10] F. Iwasaki, K. Suga, Y. Okamoto, and H. Umakoshi, "Liposomes can achieve enantioselective C-C bond formation of an α -amino acid derivative in aqueous media," *ACS Omega*, vol. 2, no. 1, pp. 91-97, 2017.
- [11] M. Hirose, S. Fujiwara, T. Ishigami, K. Suga, Y. Okamoto, and H. Umakoshi, "Liposome membranes assist the L-proline-catalyzed aldol reaction of acetone and p-nitrobenzaldehyde in water," *Chemistry Letters*, vol. 47, no. 7, pp. 931-934, 2018.
- [12] K. Suga, K. Akizaki, and H. Umakoshi, "Quantitative monitoring of microphase separation behaviors in cationic liposomes using HHC, DPH, and laurdan: estimation of the local electrostatic potentials in microdomains," *Langmuir*, vol. 32, no. 15, pp. 3630-3636, 2016.
- [13] T. Ishigami, K. Suga, and H. Umakoshi, "Chiral recognition of l-amino acids on liposomes prepared with l-phospholipid," *ACS Applied Materials & Interfaces*, vol. 7, no. 38, pp. 21065-21072, 2015.
- [14] F. Tanaka, R. Thayumanavan, and C. F. Barbas, "Fluorescent detection of carbon-carbon bond formation," *Journal of American Chemical Society*, vol. 125, pp. 8523-8528, 2003.
- [15] B. List, P. Pojarliev, W. T. Biller, and H. J. Martin, "The proline-catalyzed direct asymmetric three-component manich reaction: scope, optimization, and application to the highly enantioselective synthesis of 1,2-amino alcohols," *Journal of American Chemical Society*, vol. 124, no. 5, pp. 827-833, 2002.
- [16] U. I. Tafida, A. Uzairu, and S. E. Abechi, "Mechanism and rate constant of proline-catalysed asymmetric aldol reaction of acetone and p-nitrobenzaldehyde in solution medium: density-functional theory computation," *Journal of Advanced Research*, vol. 12, pp. 11-19, 2018.
- [17] D. Mandalapu, "L-proline and d-proline (chiral amino acid catalysts)," *Synlett*, vol. 26, no. 5, pp. 707-708, 2015.
- [18] E. Conde, D. Bello, A. de C3zar, M. S3nchez, M. A. V3zquez, and F. P. Coss3o, "Densely substituted unnatural l- and d-prolines as catalysts for highly enantioselective stereodivergent (3 + 2) cycloadditions and aldol reactions," *Chemical Science*, vol. 3, no. 5, pp. 1486-1491, 2012.
- [19] T. Ishigami, M. S. Chern, K. Suga, Y. Okamoto, and H. Umakoshi, "Adsorption behavior of propranolol on negatively-charged liposomes and its influence on membrane fluidity and polarity," *Journal of Nanoscience and Nanotechnology*, vol. 17, no. 3, pp. 1721-1728, 2017.

Review Article

Functional Hydration Behavior: Interrelation between Hydration and Molecular Properties at Lipid Membrane Interfaces

Nozomi Watanabe, Keishi Suga , and Hiroshi Umakoshi 

Graduate School of Engineering Science, Osaka University, Toyonaka, Osaka, Japan

Correspondence should be addressed to Hiroshi Umakoshi; umakoshi@cheng.es.osaka-u.ac.jp

Received 31 August 2018; Revised 30 November 2018; Accepted 16 December 2018; Published 13 January 2019

Academic Editor: Ester Chiessi

Copyright © 2019 Nozomi Watanabe et al. This is an open access article distributed under the Creative Commons Attribution License, which permits unrestricted use, distribution, and reproduction in any medium, provided the original work is properly cited.

Water is an abundant commodity and has various important functions. It stabilizes the structure of biological macromolecules, controls biochemical activities, and regulates interfacial/intermolecular interactions. Common aspects of interfacial water can be obtained by overviewing fundamental functions and properties at different temporal and spatial scales. It is important to understand the hydrogen bonding and structural properties of water and to evaluate the individual molecular species having different hydration properties. Water molecules form hydrogen bonds with biomolecules and contribute to the adjustment of their properties, such as surface charge, hydrophilicity, and structural flexibility. In this review, the fundamental properties of water molecules and the methods used for the analyses of water dynamics are summarized. In particular, the interrelation between the hydration properties, determined by molecules, and the properties of molecules, determined by their hydration properties, are discussed using the lipid membrane as an example. Accordingly, interesting water functions are introduced that provide beneficial information in the fields of biochemistry, medicine, and food chemistry.

1. Introduction

Water is an abundant and interesting molecule that has various functions in biological systems. In this context, it has attracted much interest in a variety of research fields. Water is the only solvent that can be drunk without serious risks to human health, and is therefore indispensable in the food and medical fields. Specifically, the hydration state of food is one of the important and determining factors of its quality. The water (moisture) content of food controls its subtle taste and texture. Accordingly, controlling the amount and state of water is critical for the preservation of the quality of food because the elimination of water drastically reduces the growth of living species (bacteria and fungi). Drying and freezing foods prevent the growth of microorganisms, and they thus constitute useful techniques for food preservation. Conversely, drying and freezing may diminish the taste of food because the characteristics of water (or ice) play very important roles in the organization of the constituent structures of materials in food. Salting and sugaring also

improve food stabilities, while higher concentrations of salt lead to the denaturation of proteins. The colloidal properties of solution are also sensitive to the amount of water. In systems which only consist of oily components, the phase separation behaviors can be dependent on the composition, temperature, pH, salt concentration, and the presence of surfactants. In the case of agar hydrogels often used as edible polymers, their stiffness can contribute as a determinant of taste, wherein the hydration state is a considerable factor that determines the sponge structure of the formed hydrogel. Considering the above, the quality of food is relevant to the hydration state and to the structure of the component.

Regarding the stability and freshness of food, an important concept relates to the method/approach required to maintain the structure of cells, proteins (or enzymes), and self-assembled compounds in food materials. The capacity of water molecules to functionalize biological molecules and their assemblies has been investigated for many years [1]. Water molecules are essential for the maintenance of the physiological cell function and structure. Therefore, it is

required to understand how it behaves as a modulator from various viewpoints, including chemical, physical, and biological. The biological interfaces, e.g., the surfaces of proteins, nucleic acids, and lipid membranes, are usually in well-hydrated states, and the properties of interfacial water have been attracting the interest of researchers for years [2–5]. The functions of proteins are in many cases strongly related to their structure, including the hydration water layer, wherein the hydration state of the protein surface affects the protein conformation [6]. Additionally, the water molecules associated with proteins can work to modulate the conformational properties of protein motifs [7, 8]. In cell systems, the behaviors of water at the lipid membrane surface are directly related to the maintenance of the cell structure and to their interactions with biomolecules [9]. Information on the hydration properties of the lipid membrane is also useful in the medical and biological fields. Furthermore, the polarity of the lipid membrane (hydrophilicity) is an important indicator in the targeting of nutrients and drugs to cells, both in terms of the estimation of biocompatibility and modulation of bioavailability [10, 11]. Therefore, a precise understanding of the fundamental hydration properties of the lipid membrane is required.

The lipid bilayer membrane is organized based on the hydrophobic interactions between amphiphilic molecules that constitute the hydrophobic-hydrophilic interface in an aqueous system. The lipid bilayers, usually found in cell membranes and a part of the outer membranes of intracellular compartments, act as physical barriers to prevent the free permeation of water and water-soluble compounds, thus playing an essential role in the maintenance of cellular homeostasis. In the various types of biological interfaces (including lipid membranes), the key aspects pertaining to the roles of water molecules are as follows: (1) hydration properties that can be influenced by the formation of hydrogen bonds between the hydration water molecules and the substance of interest and (2) classification of water molecules according to their hydration characteristics, such as the strong hydration properties/characteristics exhibited at the interface or in the bulk. Although the hydration properties of food are complicated, the hydration water layer of each component (proteins, nucleic acids, membranes, and other small molecules) is still relevant from the viewpoints of chemistry, biology, medicinal chemistry, and so on (Figure 1).

In systems, such as proteins, lipid membranes, and polymer surfaces, the interfacial water molecules exist as hydration water layers and exhibit different properties compared to those in bulk water. In the case of the hydration water in a phospholipid bilayer membrane system, the binding state of the hydration water varies, depending on the binding position [12]. The water group that binds directly at the interface can be considered as a first-order hydration water group. Additionally, the associating water molecules around the first group can be more flexible, and these groups can be regarded as second-order hydration water groups. Recently, an increased focus has been documented on the classification of the interfacial hydration water on such groups because each hydration water group can play

important roles in (a) modulating protein structure and function and (b) regulating adhesion among (bio)materials [13]. It is also important to evaluate the thermodynamic properties of hydration instead of observing the binding properties. The classification of interfacial water molecules into several groups allows us to understand their contributions. The understanding of the hydration properties is essential for food materials from the viewpoint of the structural stability and function of each component, including the lipid membranes. In this review, the recent approaches adopted for the investigation of water properties, and the fundamental interrelation between hydration and molecular properties, are summarized with a special focus on lipid membrane properties.

2. Basic Properties of Water Molecules/Observation of Water

Water molecules thermally diffuse in liquid to perform certain functions by assuming certain structures: Eisenberg and Kauzmann assumed that the structure of water molecules is classified according to the observation time (Figure 2) [14].

- (a) I, structure at each instant ($t < \tau_v$)
- (b) V, structure averaged with respect to vibration ($\tau_v < t < \tau_D$)
- (c) D, structure averaged with regard to the orientation and movement of molecules ($\tau_D < t$)

The orders of τ_v and τ_D are 10^{-13} s and 10^{-12} s, respectively. Most of the water properties are investigated to relate to the D-structure, whereas there are few measurement methods relevant to the V-structure. The evaluation of the hydration water behaviors can be dependent on the measurement method in accordance with the characteristics of the target water.

2.1. Experimental Approach: Observations of Direct Motion of Water Molecules. X-ray and neutron diffraction spectroscopy are representative experimental methods that have been used to evaluate water molecules on nucleic acids, proteins, lipid membranes, reverse micelles, etc. The orientations of the water molecules within the hydration layer have also been discussed [15–19]. The properties of the hydration layer are not simple. Accordingly, related studies on hydration layers are discussed in Section 3. Given that X-ray diffraction and neutron diffraction measurements require crystallized samples, the molecular structure and patterns might be different compared to those in aqueous solution systems. Specifically, these approaches are effective in identifying potential properties, such as the stereoscopic characteristics at the interface (including the hydration water). Small-angle X-ray scattering (SAXS) and small-angle neutron scattering (SANS) have been adopted to evaluate molecular structures at the nanometer scale, and they are often used for the investigation of the hydration layer [20–23]. A molecular distribution analysis suggests that the density of water in the hydration layer on the protein is

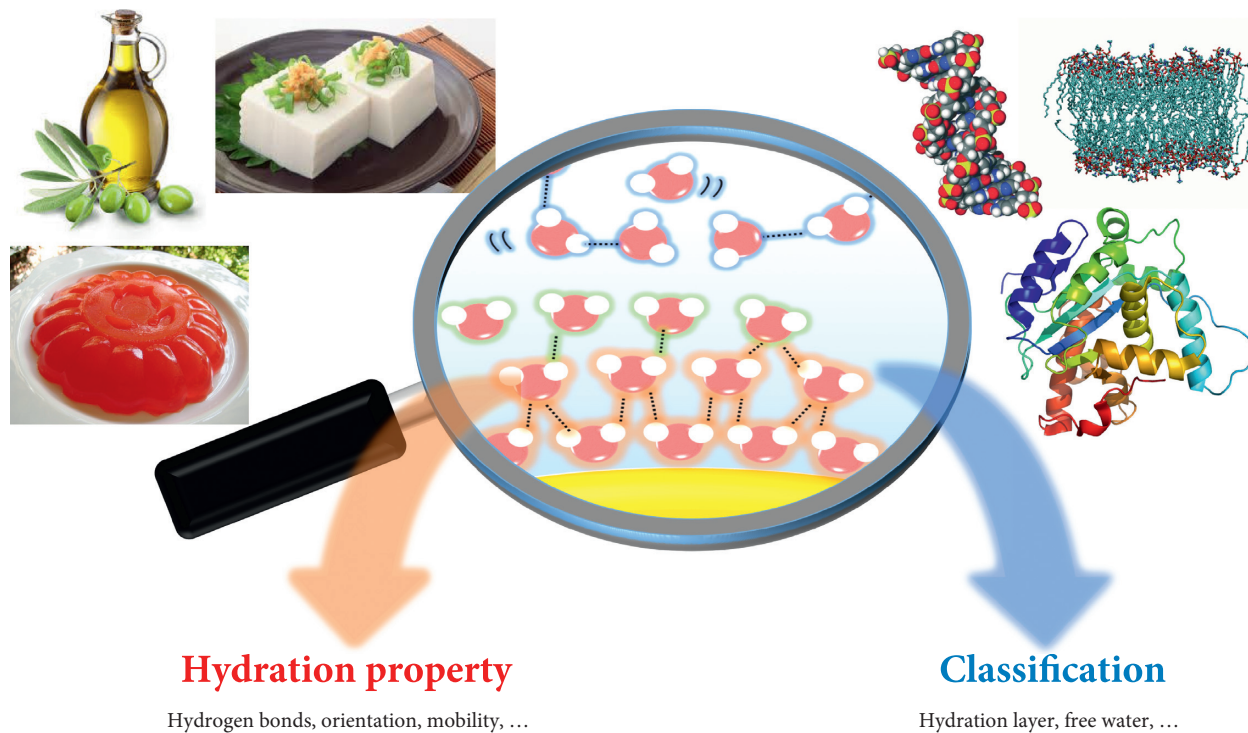


FIGURE 1: Possible role of water in various fields.

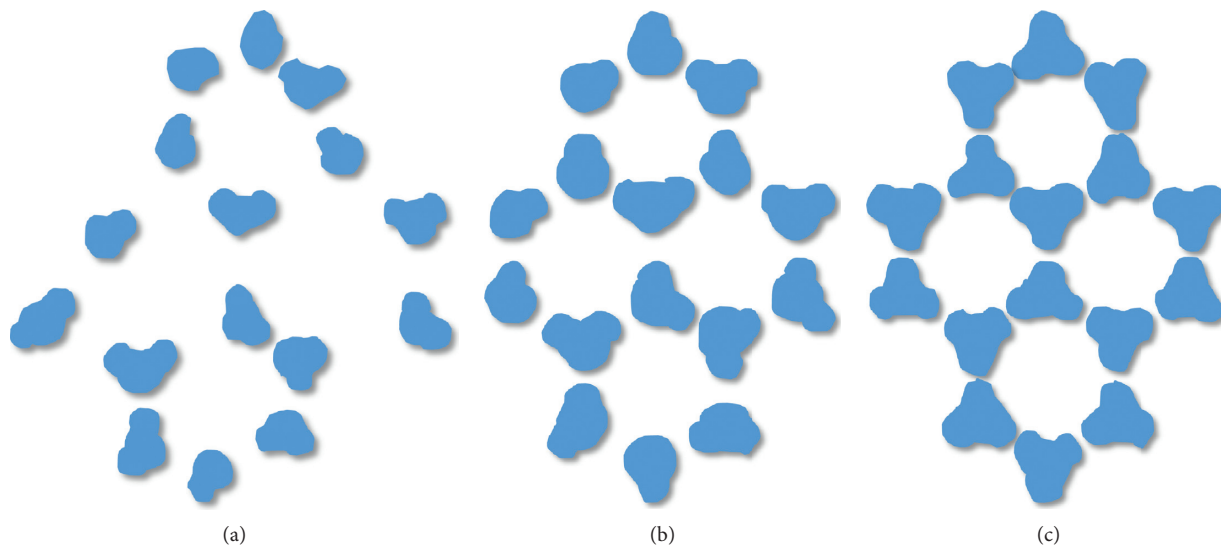


FIGURE 2: Classification of water molecules. Illustration was drawn according to Eisenberg and Kauzmann [14]. (a) I-structure. (b) V-structure. (c) D-structure.

approximately 15% higher than the water density in the bulk [21, 23]. Additionally, in lipid bilayer systems, the excess number of water molecules can be distributed at the membrane-bulk interface region [24]. By employing SAXS, the structural properties of food can be evaluated. From a scientific viewpoint, the self-organized structure of mayonnaise can be categorized in emulsion gels (oil-in-water emulsions) or in bicontinuous cubic phases [25].

Infrared (IR) and Raman spectroscopy can be utilized to investigate the behaviors of hydration water at interfaces

[26–29]. Nonhydrogen bonding water molecules have been reported by many researchers based on Raman spectroscopic analyses [29–31]. Typically, H_2O or D_2O is employed as solvents for biological species, and the contribution of the O-H or O-D vibration stretching modes from target molecules is analyzed. Walrafen et al. observed the isosbestic point in the O-D vibrational modes measured at different temperatures. In overlays of these spectra, each spectrum yielded a cross point at a specific frequency. By varying the temperature, the frequencies derived from pure α^2 and pure

β^2 (whereby α and β correspond to polarizability and anisotropy, respectively) yielded the isosbestic point. This suggests that the hydrogen-bonded and nonhydrogen-bonded water are in a thermodynamically equilibrium state [32, 33]. The ΔH° value of the OH–O bond was estimated to be -2.6 kcal/mol [34]. In Raman and IR measurements, several types of vibrational peaks are summed in one spectrum, and peak deconvolution is thus an effective tool in assigning the contribution of each molecule or bond [35–37]. These methods are very useful for evaluating the dynamic behaviors of water molecules.

Flexible molecules, such as solutes in aqueous systems, or molecules in self-assembly systems, exhibit dynamic behaviors in response to external stimuli. This is derived from the reorientation of the associated water molecules. Spin relaxation of hydrogen or oxygen isotopes can be measured as a function of time [38]. In general, the molecular dynamics can be evaluated at the order of nanoseconds to investigate the behaviors of proteins and nucleic acids [39–41]. Accordingly, the net rotational correlation time of water molecules is obtained based on magnetic relaxation dispersion (MRD) to monitor the slow dynamics associated with biomolecules. In experimental approaches, it is difficult to distinguish the molecular behaviors of water molecules because the physicochemical property differences between free water (bulk water) and hydration water are extremely small. Correspondingly, computer simulation approaches have been extensively employed (e.g., MD simulations, etc.) [42–44]. Furthermore, NMR measurements reflect the information of all the molecules from the entire system. However, it could be difficult to identify the signals of the hydration water and solvent water in solution NMR measurements. By contrast, the MRD analysis has been extensively studied to monitor the dynamic behavior of the molecules and has been shown to elicit results that are highly correlated with the outcomes of simulation studies [45–47].

The sum-frequency generation (SFG) vibrational spectroscopy can observe an asymmetric molecular fraction in the vicinity of the interface [48]. It is mainly used for analyzing the hydration state to the lipid membrane at an air-water interface [43], and it is applied to monitor the direction at which the water molecules orient themselves around the lipid head group (H-up, H-down) [49, 50]. Although there are limitations associated with the directionality at the interface and with the experimental conditions, SFG is a powerful tool used to evaluate the orientation of water molecules at the molecular surface.

2.2. Experimental Approach: Observations of Water Molecules as a Group. In dielectric relaxation spectroscopy, it is possible to observe the behavior of the dipole moments of water molecules [51–54]. If the system is swept by an alternating electric field, the dipole of the water molecule exhibits a Debye relaxation. Given that the relaxation time of water is relevant to the hydration characteristics, its value depends on the reorientation time of individual molecules [55]. The precise definition of the scale of each water group is still under discussion. In addition, the bulk water molecules

affect the hydrated water molecules in the vicinity of the target molecule [41, 56, 57]. Therefore, it is necessary to consider the fact that the observed dynamics of water are cooperatively restricted compared to its original characteristics. As an improvement of the experimental method, the number of hydration water molecules can be estimated based on the deconvolution of the multiple relaxation peaks [44].

Dynamic light scattering (DLS) and the optical Kerr effect are sensitive to the refractive index of the solvent. Similar to the dielectric relaxation analysis, the polar tensor relaxation can be measured using these methods. Given that the molecular polar tensor of water is almost isotropic, these techniques essentially probe the collective translational rearrangements of the water molecules [56, 57]. Terahertz spectroscopy can measure the physical properties corresponding to the distortion of the hydrogen bond network in the far IR range. By comparing the bands near the bulk and the molecule, the hydrogen bond in the vicinity of the molecule can be detected. Utilizing this technique, the existence of a dynamic hydration shell with a thickness of 20 \AA has been observed around proteins [58–61]. There are some assumptions in this definition pertaining to the restriction of this shell, including its uniform distribution, for example. Dielectric properties relate to the water activity (a_w) that constitutes a representative index for the water affinity on food material. There are some reports on the application of the dielectric analysis mentioned above for the purpose of the investigation and monitoring of the quality of the food products [62, 63].

2.3. Experimental Approach: Indirect Observation of Water Behavior. Highly sensitive and specific information on the biological interface can be obtained from molecular probe methods. To evaluate the hydration environment at biological interfaces, numerous fluorescent molecules have been developed in which the probes are sensitive to their local environment [64]. Various probe molecules have been designed and optimized: herein the probe preferentially binds to the target molecule and elicits strong fluorescence signals reflecting their microscopic surroundings. Usually, the internal part of biomolecules (core of proteins, strand regions of nucleic base-pairs) is hydrophobic compared to water, and the inserted fluorescent probe can thus emit a stronger fluorescence signal. For example, the exposed hydrophobic site in the denatured protein or the self-assembly surface, such as the lipid membrane, can be detected by polarity-sensitive probes, such as the 8-anilino-1-naphthalenesulfonic acid (ANS) and 6-(p-toluidino)naphthalene-2-sulfonate (TNS) [65–69]. Solvent-sensitive fluorescent probes, such as 6-propionyl-2-dimethyl-aminonaphthalene (prodan), 6-dodecanoyl-2-dimethylaminonaphthalene (laurdan), ANS, and TNS, are extensively used for the characterization of the lipid membrane [70–73]. These molecules have a dipole moment following their excitation and induce the relaxation of the surrounding water molecules. Hence, they exhibit various fluorescence characteristics

according to the degree of solvent relaxation [74, 75]. The specificity of the fluorescent probe's location in the lipid membranes has advantages and disadvantages. An advantage is the fact that the choice of a specific probe enables us to analyze more localized information toward the lipid bilayer, such as the membrane surface region monitored by 1-(4-trimethylammoniumphenyl)-6-phenyl-1,3,5-hexatriene (TMA-DPH), for example. The membrane inner region can be monitored by 1,6-diphenyl-1,3,5-hexatriene (DPH) [76]. A disadvantage is the fact that the fluorescence property (quantum yield) can be varied depending on the polarity and viscosity of the solvent. Thus, the information obtained from a single fluorescence probe could include multiple factors. Accordingly, the alteration of the membrane property can be induced by an external molecule (e.g., protein binding) and vice versa. The use of multiple fluorescence probes can solve these problems. Therefore, it is recommended that several types of probes be used such that the interfacial polar environment can be systematically investigated [77–79].

The type and quantity of water molecules can be identified by using differential scanning calorimetry (DSC) based on the heat balance of the water freezing/thawing processes. In the polymer systems, the water molecules can be classified into the intermediate and free water types and can be observed with (a) endothermal peak temperatures $>0^{\circ}\text{C}$ and (b) $<0^{\circ}\text{C}$, respectively [80, 81]. Because the water in polymers does not freeze at temperatures less than 0°C , it can be distinguished from free water (bulk water). Therefore, the amount of nonfreezing water can be evaluated by identifying the difference between the amount of intermediate water and free water obtained from the entire system. This is a very effective method because the heat capacity can be evaluated from the dilution/melting peak. Regarding the evaluation of water in the biomolecules, the structure of the molecule largely affects the hydration characteristics. Thus, the differentiation of the type of water constitutes a significant problem. Each experimental approach has limitations regarding the observable time allotted to the dynamics of the target molecule. According to previous reports, the experimental approaches used for the investigation of water dynamics are summarized in Figure 3.

2.4. Simulation Approach of Water Behavior. For the computational simulation of water dynamics, it is essential to set the force fields of water and coexisting molecules. Until now, many potential functions have been proposed to produce the molecular behaviors in simulation approaches [83]. Given that the most extensively used approaches are based on the theoretical and experimental results, various models of water molecules have been developed, such as TIP3P, TIP4P, SPC, etc. [84–87]. The average number of nearest neighboring molecules was increased to almost five in liquid water. Additionally, the average number of hydrogen bonds per molecule decreased to three in comparison to the state of ice. Recent studies revealed the possible structures of water clusters composed of four or eight molecules, and the

mechanism responsible for the density fluctuations is well supported by simulation results [88]. Some representative water clusters, such as the cyclic pentamer, bicyclo-octamer, and tricyclo-decamer, are relatively stable, and the dynamic behavior exchanging continuous formation of hydrogen bonding networks has also been studied [89].

Considering the behavior of water as solvent, simulation calculations at the hydration layer must be conducted. The hydration shell can be defined as a group of water molecules in which the orientation of the dipole moment is in a good arrangement in the first layer (with a thickness which is approximately equal to 3.5 \AA). However, the definition of the hydration shell (or layer) is controversial because the water molecules in these layers exhibit different properties depending on their interaction states with other molecules [13, 42, 59, 60]. The distance to the first minimum value in the radial distribution function can be defined as hydration shell including whole contributions of the motional properties of water molecules such as rotation, translation, and hydrogen bonds [82, 87, 90, 91]. Finally, the mechanical properties of the water molecules present in the hydrated shell can be investigated [92].

3. Hydration Layer

The water molecules randomly distribute depending on their dipole-dipole interactions and form a hydrogen bond network among water molecules via electrostatic interactions. Ultimately, a layer of water molecules is formed from a hydrophobic interface with a thickness that spans several nanometers [93, 94]. Although the definition of the hydration layer varies depending on the interface to be targeted, a similar tendency can be observed within biological interfaces. Uedaira et al. suggested a concept of structured hydration layers based on studies using the ^{17}O NMR spin-lattice relaxation [95]. The authors defined the dynamic hydration number n_{DHN} that represents the dynamic characteristics of hydration. The thickness of the structured water is at least several nm irrespective of the type of material constituting the interface, that is, the hydration layers comprising approximately 10 water molecules are structured [95].

Israelachvili et al. measured the intermolecular forces between mica plates in dilute KCl solutions [96]. The interaction of the two interfaces was well explained by the DLVO theory using distances of 10 nm or less. When the distance of the interfaces was less than 1.5 nm, the oscillations appeared at every $0.25 \pm 0.03 \text{ nm}$ [97]. In this case, 6–7 oriented water molecules existed between the mica plates. The short-range hydration force between the smooth rigid surfaces was always oscillatory as water molecules attached to the hydrated surface groups and formed an ordered layer [97]. This repulsive force is a synergistic hydrogen bond (polarized) interaction that attenuates as a function of distance from the surface [98, 99]. Interestingly, in flexible surfaces, such as lipid membranes, these vibrations are averaged into a monotonous repulsive force because of the roughness of the head group of lipid molecule and the repulsive thermal

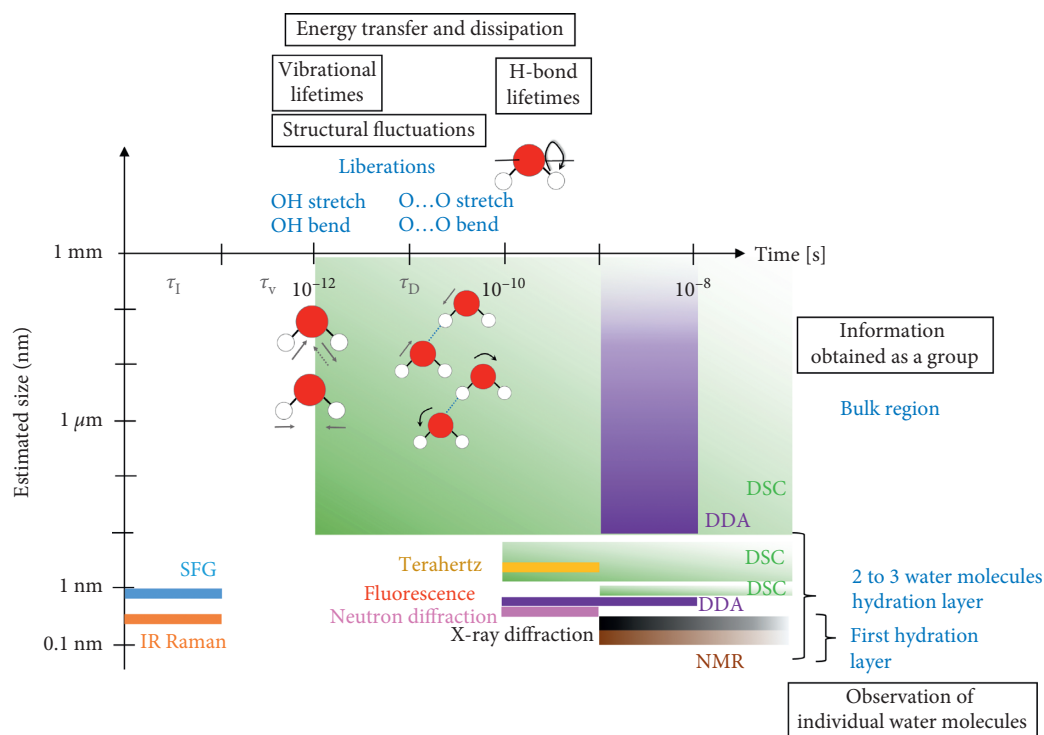


FIGURE 3: Experimental approach for the investigation of water dynamics. The molecular properties of water are summarized according to Fogarty and Laage [82].

fluctuation force that arises from the dynamic nature of the lipid membrane surface [100–102].

The hydration layer on the MgO solid surface is consistent of approximately 10 molecules (with single-molecule layers and layers with thicknesses spanning two or three molecules) [103]. The first water molecules orient in such a way that (a) one hydrogen atom faces the oxygen atom of MgO and (b) the OH groups are aligned parallel to the MgO plane. The thickness of the first layer is in the range of 0.2–0.3 nm, while the second layer is a more distributed alignment of the water molecules with thickness values in the range of 0.4–0.6 nm. Thicknesses equal to three or more layers are equivalent to bulk water, and the orientation anisotropy disappears. According to Zhang et al., the self-diffusion coefficient of water in the wall of the capillary ($\epsilon = 5$) ranges from 4.5 to $4.9 \times 10^{-9} \text{ m}^2 \cdot \text{s}^{-1}$ and that of bulk water is two times smaller and equal to $2.7 \times 10^{-9} \text{ m}^2 \cdot \text{s}^{-1}$ [104]. A group of water molecules in the form of a layer on such an interface has been extensively studied as functional water [13, 61].

In the polymer system, the water layer, commonly referred to as an intermediate layer, is assumed to adjust the accumulation of proteins [59, 82]. In a separation system using a polymer, such as in artificial dialysis, grasping the activity of water molecules in this intermediate layer leads to the design of a high-performance separation membrane. The water molecules at these intermediate layers are measured by using DSC, dielectric spectroscopy, NMR, and so on. In the case of biopolymers, it is argued that a layer comprising a single molecule is defined as the first hydration layer, while a second hydration layer has a thickness that spans 2–10

molecules [13]. In biomolecules, some polar or charged sites appear on the surface that can strongly interact with the first layer of water molecules via hydrogen bonds or electrostatic interactions. These heterogeneous states in the hydration properties can result in the generation of electric fields. However, these properties have not been well clarified. The concepts related to the hydration layer according to the reviewed studies are summarized in Figure 4. The food materials derived from animals or plants can be considered as the assembled cell tissue, wherein the front part of the food material surface can consist of cell membranes. In the following sections, the correlation between the hydration behavior and molecular properties is discussed, especially focusing on the lipid membranes as representatives of the potential functions of biological interfaces.

4. Hydration Properties in Lipid Membranes

The lipid bilayer membrane provides different polar environments, whereby the surface regions from the lipid head group to the glycerol group are hydrophilic. In contrast, the inner membrane region is hydrophobic owing to the accumulated hydrocarbon chain [105]. For the experimental study of lipid bilayer membranes, the “liposome” can be used as the artificial self-assembled entity with a phospholipid membrane (Figure 5). The hydration layer is formed between bulk and hydrophobic core regions. Herein, the word “membrane surface” indicates the hydrophilic region of the lipid bilayer, which acts as the interface of interaction with the surrounding solvent water. The “membrane interface” indicates the border between the hydrophilic and the

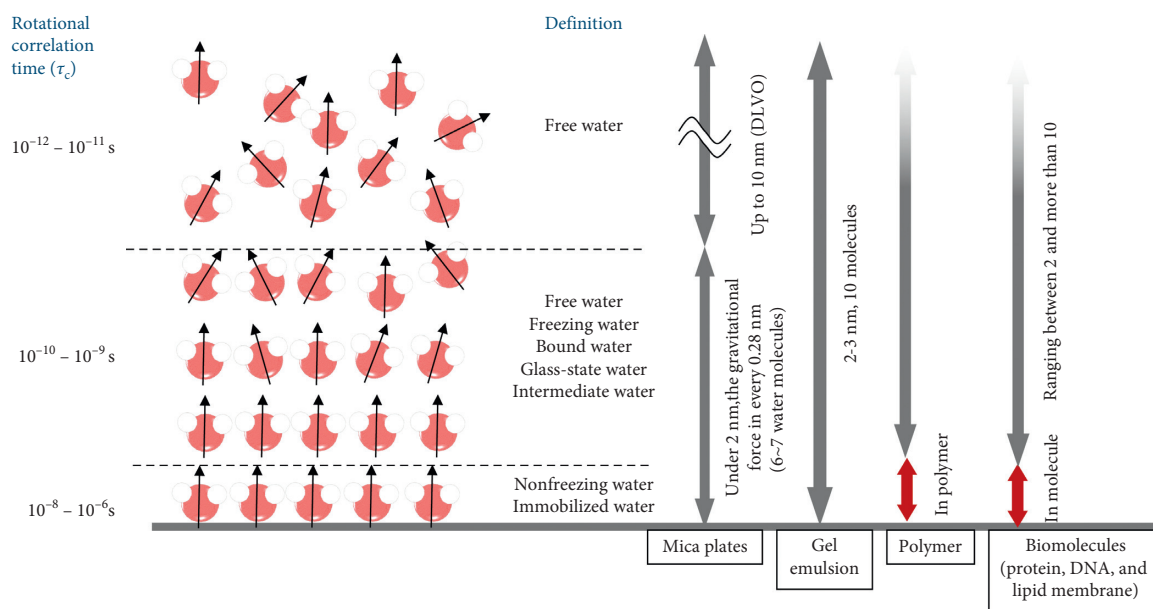


FIGURE 4: Concepts of hydration layer.

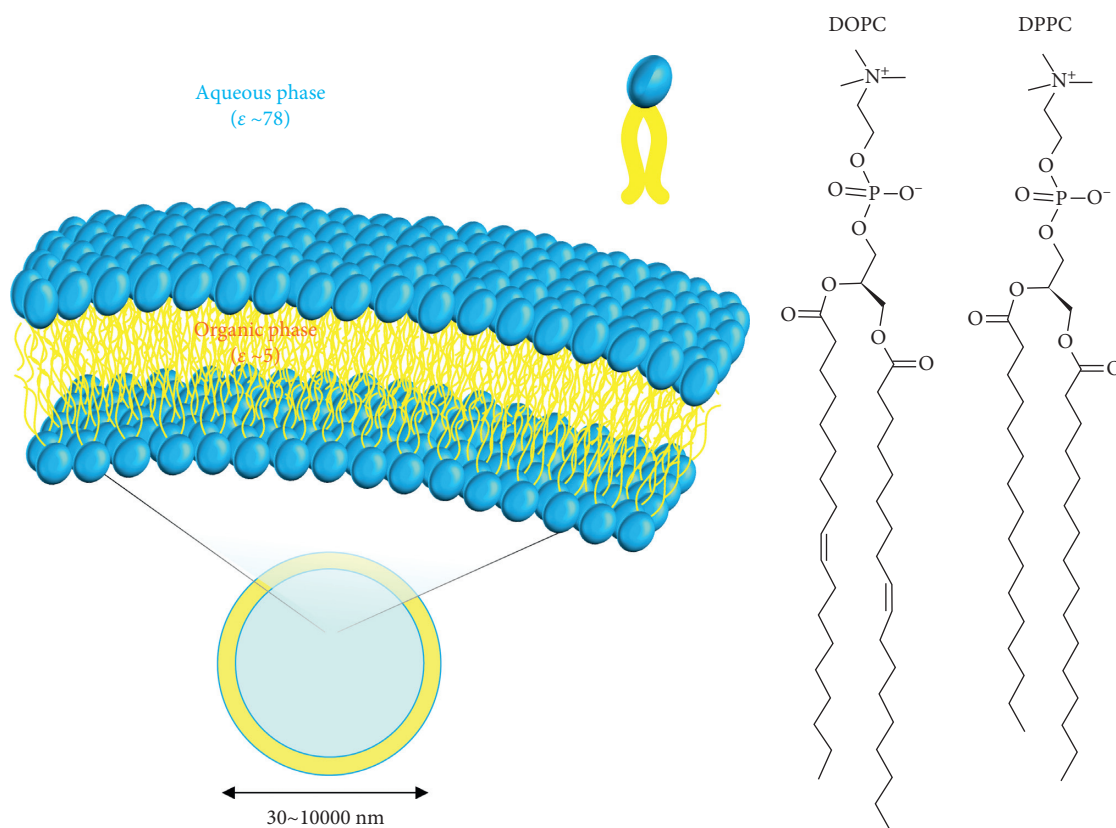


FIGURE 5: Schematic illustration of liposome and typical structures of PCs (DOPC, DPPC). Liposomes can be prepared by the thin-film hydration method [109].

hydrophobic regions of the membrane, that is, the region around the carbonyl group of the lipid molecules. The hydration state of the lipid membrane is complicated (cannot be simply defined) owing to the various contributing factors, such as for example, the chemical structure of the lipid head

group, acyl chain packing state, lateral interaction between lipids, etc. A typical zwitterionic phospholipid, e.g., diacylglycerophosphocholine (PC), known as lecithin, possesses both a negatively charged phosphate group and a positively charged choline group. These zwitterionic head

groups are strongly hydrated via hydrogen bonds with solvent water. In a phosphate group, the bound water molecules are retained in a tetrahedral structure around the oxygen atoms [106–108]. The water molecules associated with the positively charged choline group are weakly connected to each other in a clathrate hydration state [106, 107]. As shown in the 1,2-dipalmitoyl-*sn*-glycero-3-phosphocholine (DPPC) membrane, the water molecules around the CH₂ moieties in the choline group are distributed according to the Gaussian distribution, regardless of the membrane phase state. Hence, their existence cannot be ignored [82].

In general, the hydration layer formed on the surface of the PC membrane prevents the access of water-soluble molecules, despite the existence of the thin hydration layer which has a thickness of approximately 1 nm [24]. It is still unclear how such a hydration layer can inhibit the access to external molecules. A thicker hydration layer can stabilize the self-assembled structure of the membrane, which is one of the important topics related to the design of drug carriers [110]. The hydration property of the membrane can be varied depending on the lipid head group. In addition, the lipids modified with polyethylene glycol (PEG) and glycolipids allow the existence of large numbers of water molecules in the form of a hydrated sponge [111]. In consideration of other factors that influence the hydration behaviors, the simulation study on the associated dynamics has investigated the fact that the hydrogen bonds between the water molecules are strengthened on the lipid membrane that is composed of phosphoethanolamine (PE) lipids [107]. The PE has a small head group which creates a flat membrane surface, thus resulting in the enclosure of lipid molecules. From this point-of-view, it is considered that the uniformity of the charge characteristics of the surface layer also contributes to the stability of the bonds between the water molecules [112].

In research studies using SFG, the direction and hydration characteristics of the water molecules at the hydrophilic/hydrophobic interface were evaluated. One of the advantages of SFG measurements is the observation of the orientation of molecules localized at the bulk-membrane interface [48, 106]. In the lipid monolayer system formed at the air-water interface, the water molecules in anionic lipid membranes, such as 1,2-dipalmitoyl-*sn*-glycero-3-phospho-(1'-*rac*-glycerol) (DPPG), are oriented to direct the hydrogen atoms toward the lipid head, while the water molecules exceeding the phosphate group are oriented so that the hydrogen atoms are directed in the opposite direction [48]. For cationic lipid membranes, such as 1,2-dipalmitoyl-3-trimethylammonium-propane (DPTAP), the orientation of the hydration water layer is opposite to that in the case of DPPG, wherein the water on the bulk side and inside the membrane directs oxygen atoms toward the head group [48]. Such orientations of water are very important for the understanding of the complex hydration environment at the lipid membrane surface.

From the structural point-of-view, it has also been suggested that the water molecules existing among acyl chains contribute to the stability of the structure of the

molecule, based on simulation and FTIR studies [113, 114]. Alarcón et al. analyzed the hydration state of DPPC using simulations, and confirmed that the water molecules between the acyl chains formed a chain-like configuration which was stabilized in the acyl chain pocket. Additionally, these results were consistent with the experimental results [19]. In the case of lipid molecules which possess hydrogen bond donor or acceptor groups, such as sphingomyelin, the water molecules can align with respect to the NH group of the backbone structure as well as with respect to the phosphate and choline groups because of the strong hydrogen bond acceptors of oxygen atoms in water. Comparison of PC and sphingomyelin with the same acyl chain lengths indicates that the sphingomyelin membranes have multiple hydration layers owing to the hydrogen bond with solvent waters, as confirmed by NMR measurements [115]. Regarding the unsaturated sphingomyelin, the possibility of intermolecular hydrogen bond interactions can be replaced by the hydrogen bonds formed with water molecules that increase molecular flexibility according to quantum chemistry approaches [116]. It is suggested that the subtle configuration differences, such as saturated and unsaturated configurations, could affect the hydration behavior.

Generally, the lipid membranes composed of unsaturated acyl chain lipids exhibit a hydrophilic property owing to their loosely packed lipid orientation. By contrast, the lipid membrane—composed of saturated lipids—elicits rather hydrophobic properties owing to the high-packing-lipid density at the temperature below the phase transition temperature. The lipid rafts, mainly composed of sphingomyelin and cholesterol, are hydrophobic because of their highly packed membrane states [117]. The configuration of the “umbrella model,” whereby the head group of sphingomyelin covers cholesterol and the shielded inner membrane region, may contribute to the dehydrated inner membrane environment [118]. It is considered that this umbrella structure moves the hydration water layers around the head group out. Finally, the expelled water molecules can be accumulated like a shell, which might be observed as high-density water molecule layers at the membrane surface.

As shown in the examples above, the hydration state in the lipid membrane is very complicated, and mechanisms of stabilization of each hydration can be varied by different molecules. However, it is a very interesting task to ascertain whether the membrane properties determine the hydration characteristics, or whether the hydration characteristics determine the membrane properties, and how this works for the interaction with biomolecules. In the next section, the membrane characteristics determined by the hydration properties are introduced.

5. Membrane Properties Determined by Hydration

Considering the interfacial interaction, electrostatic interactions operate at longer distances. By contrast, the hydration waters provide a strong repulsion (referred to as a hydration force, as already mentioned in Section 3), which applies at very short distances [119]. Based on the

measurements of surface forces developed between bilayer membranes, it was confirmed that there was an additional repulsive force derived from the hydration force for hydration thicknesses of approximately 2 nm or less [120]. Additional energy is required to induce the dehydration of the head group region. Additional approaches increase the repulsion force at distances within the range of 0.2–0.3 nm [121]. This repulsive force prevents the adhesion of each lipid membrane. Therefore, it is interesting to know how lipid membranes interact with other biomolecules, such as enzymes, beyond this hydration wall.

In the zwitterionic lipid bilayer, the lipid molecules have a net charge that is equal to zero. Surface charge properties are determined by the hydration shell. The carbonyl and phosphate groups possess lone-pair electrons, and the water molecules bound to them can be polarized. The charge properties of the fixed layer (lipid) are shielded by anions (van der Waals interactions rather than electronegativity) and cations [122]. The width of this layer is defined by the slip plane which determines the ζ potential [123]. Given that PC groups have phosphate groups oriented outward, it can be assumed that slip planes from phosphate groups can be considered. However, attention should be paid to interfaces where unevenness occurs on the surface layers, such as negatively charged phosphatidylserine (PS) and hydrogen donor phosphatidylinositol (PI) moieties. Thus, the heterogeneity in the lateral lipid distribution can be an important factor to generate a potential field for the interaction.

The degree of water saturation also affects the orientation of the dipole moment of the lipid head group. In the highly hydrated interfacial region, the orientation of hydration water molecules around the carbonyl and phosphate moieties could modulate the orientation of the head group [114, 124]. For low degrees of hydrations, the direction of the dipole potential in the head group is reversed, and the surface charge potential of the membrane thus exhibits negatively charged properties [125, 126]. The increase in the mean head area can be induced by hydration swelling. For example, the mean head group area of a lecithin molecule and the distance between neighboring lipids molecules on its membrane surface are 0.7 nm² and 2.7 nm, whereas 0.45–0.55 nm² and 1.3 nm for PE lipids, respectively. Thus, the repulsive force between the PE head groups is quite small [122]. Water molecules in the hydration shell of the membrane strongly bind to polyhydroxyl compounds, such as trehalose, sucrose, and arbutin, thus affecting the dipole potential of the lipid [127–132]. The direct correlation between the polarized water among the polar head group and the dipole potential can be explained by water displacement by trehalose and phloretin [127]. The hydration may support the alignment of the dipole moment of the lipid head group and results in the adjustment of the electrochemical property of the lipid membrane.

The permeability of water molecules affects the packing of the membrane plane and domain formation [125, 133–135]. According to a prior review that summarized the membrane structure and its repulsion against permeability, the number of water molecules that stabilize the inner membrane plane is considered to be 10 per PC [136].

Water molecules directly hydrating the carbonyl and phosphate groups are impermeable, and the indirectly hydrated water molecules are regarded as permeable. When the population of water molecules exceeds the referred number, the lipid-lipid interactions can be affected by the existence of water. As the packing density in the hydrophilic part of the membrane decreases, the water penetration increases. It also relates to the ability of water molecules to be exchanged because the water molecules could strongly interact with the polar groups of other molecules that could prevent the water penetration via hydrogen bonds. For example, in the presence of the dextran or PEG, water molecules in the hydration shell of the lipid membrane can be extruded owing to the strong affinity with the polar molecules [137, 138]. Dehydration based on the outward penetration compresses the membrane and reduces its volume [139]. Structural changes would occur in an energetically favorable manner by adjusting some parameters, such as the membrane packing density, or the orientation of the lipid head group. These behaviors are elicited in the membranes and in the interactions between individual molecules. Therefore, a configuration defect caused by water extrusion can be a target to replace other molecules, such as the lipid head group or the penetration of other molecules [107, 140].

The water exchange between the inner part of the lipid membrane and the bulk region was observed in NMR experiments [141]. The orientation of the hydrophilic group could influence the water exchange. The amount of hydration water will either tend to decrease as the orientation tilts, or the hydration layer around the head groups will prevent the exchange of water [142–144]. This exchange could be the important concept to consider the activity of hydrated water. When the water enters the membrane from the bulk, the lateral surface tension increases [107]. The increase in the surface pressure would occur in the penetration of the peptide. Specifically, for the analysis of the interaction with peptides in the monolayer system, the “cut off” surface pressure is used in which the surface pressure becomes insensitive to the peptide penetration [122, 145]. The “cut off” surface pressures for PCs and for PEs are approximately 40 mN/m and 30.6 mN/m, respectively. Considering the surface pressure of the saturated PC monolayer, which is approximately in the range of 46.6–48.0 mN/m, the surface pressure of the PC monolayer at which is insensitive to the peptide penetration is relatively lower. From these results, it is suggested that the protein does not penetrate at pressures that are much lower than the pressures at which the head group is filled. This indicates that an extra free energy is required to adsorb the protein, thus suggesting that the thermodynamically active water exceeds that within the hydrated shell. The significantly lower “cut off” surface pressure of the PE monolayer indicates the existence of a smaller amount of thermodynamically active water. In other experiments, lipid membranes composed of PEs interact with protease at remarkably lower rates compared to PC [146]. The difference between the restricted hydrated water molecules around carbonyl or phosphate groups, and water molecules freely dispersing among the head group region, could determine the surface active

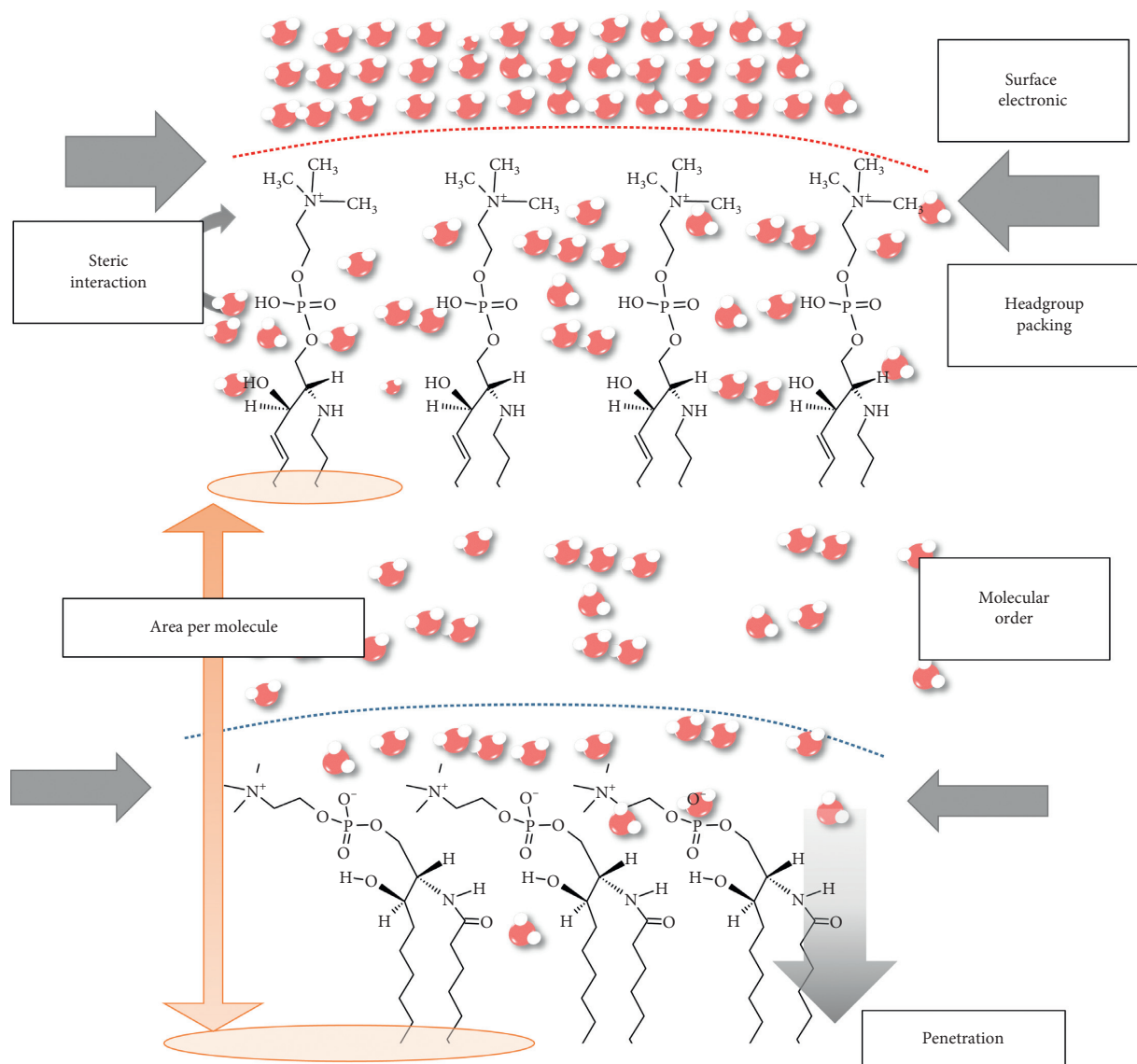


FIGURE 6: Hydration properties at the lipid membrane surface.

energy to interact with other molecules by replacing the hydrogen bonds [146]. The high free energy among lipids implies that these free water molecules could also affect the surface pressure [107]. According to the studies introduced in this review, the correlation of the hydration properties and lipid molecules are summarized in Figure 6.

6. Conclusions

Water is one the most basic and fundamental molecule in nature. It exists in various materials and modulates their unique and interesting properties, yet its actual function and role are still ambiguous. In this review, we introduced the characteristics of molecules hydrated with water by considering the hydration behavior at the lipid membrane interface as an example of a self-assembly system. As mentioned in the Introduction section, it becomes important to understand the science of water to clarify the hydrogen-bonding properties of water (what is and how it is

hydrogen bonded) and the classification (how much water of each type is present) around the biomaterial. Specifically, in food chemistry, the structural stability of the cell membrane and the homeostasis of the cell function or protein activity are significant issues in the preservation of the freshness of the material. Given that the number of consumers interested in fine food has been growing in search of healthy, tasty, and antiaging products, the design of food materials with improved performances is required. To deal with these demands, many chemical approaches have been attempted. Some require increased nutrient permeability, while others need to maintain enzyme activity. Therefore, the fundamental behavior of the cell and its activity should be understood properly in order to functionalize and sustain its physiological values.

As shown in the case of lipid membranes, the hydration property of water determines the orientation of the head group of the lipid membrane, the lipid area, the exchangeability with bulk water, and the repulsion forces.

Additionally, water molecules themselves adjust their population depending on the clustering properties in the most energetically favorable ways. The characteristics determined by hydration could lead to the surface charge characteristics of the entire system, interaction with other molecules, and the fusion of lipid membranes. This functional adjustment induced by water is not limited to lipid membranes, but contributes to a basic structure for other molecules, such as proteins, nucleic acids, and others. Various promising prospects can be expected for the health or medicinal efficacy from the synthetic chemistry viewpoint. However, the safety is always challenging. Water is an abundant molecule, and controlling its functional activities aspires to use methods with the lowest energy cost and highest safety responses. Based on the use of simulation calculations and advanced experimental techniques, steady understanding of the function of the water molecule has been accomplished. Future tasks will include the classification based on hydration characteristics that will be further required to comprehend the various systems, to understand the trends, and to grasp the original characteristics of water that could ultimately lead to the engineering of water functions.

Conflicts of Interest

The authors have no conflicts of interest to declare.

Acknowledgments

This work was primarily supported by the Japan Society for the Promotion of Science (JSPS) KAKENHI Grant-in-Aids for Scientific Research (A) (26249116), Grant-in-Aids for Young Scientists (B) (16K18279), Grant-in-Aids for Challenging Exploratory Research (T15K142040), and Grant-in-Aids for Research Fellow (JP18J11666).

References

- [1] M. L. Barkowitz, D. L. Bostick, and S. Pandit, "Aqueous solutions next to phospholipid membrane surfaces: insights from simulations," *Chemical Reviews*, vol. 106, no. 4, pp. 1527–1539, 2006.
- [2] T. Wyttenbach and M. T. Bowers, "Hydration of biomolecules," *Chemical Physics Letters*, vol. 480, no. 1–3, pp. 1–16, 2009.
- [3] W. Drost-Hansen, *Cell-Associated Water*, Academic Press, New York, NY, USA, 1979.
- [4] M. Chaplin, "Do we underestimate the importance of water in cell biology?," *Nature Reviews Molecular Cell Biology*, vol. 7, no. 11, pp. 861–866, 2006.
- [5] P. Ball, "Water as an active constituent in cell biology," *Chemical Reviews*, vol. 108, no. 1, pp. 74–108, 2008.
- [6] B. W. Zhang, D. Cui, N. Matubayasi, and R. M. Levy, "The excess chemical potential of water at the interface with a protein from end point simulations," *Journal of Physical Chemistry B*, vol. 122, no. 17, pp. 4700–4707, 2018.
- [7] M. Nakasato, "Water-protein interactions from high-resolution protein crystallography," *Philosophical Transactions of the Royal Society of London. Series B: Biological Sciences*, vol. 359, no. 1448, pp. 1191–1206, 2014.
- [8] O. Carugo, "Statistical survey of the buried waters in the protein data bank," *Amino Acids*, vol. 48, no. 1, pp. 193–202, 2015.
- [9] R. P. Rand and V. A. Parsegian, "Hydration forces between phospholipid bilayers," *Biochimica et Biophysica Acta (BBA)-Reviews on Biomembranes*, vol. 988, no. 3, pp. 351–376, 1989.
- [10] R. Rajera, K. Nagpal, S. K. Singh, and D. N. Mishra, "Niosomes: a controlled and novel drug delivery system," *Biological & Pharmaceutical Bulletin*, vol. 34, no. 7, pp. 945–953, 2011.
- [11] A. Samad, Y. Sultana, and M. Aqil, "Liposomal drug delivery systems: an update review," *Current Drug Delivery*, vol. 4, no. 4, pp. 297–305, 2007.
- [12] T. Shimanouchi, M. Sasaki, A. Hiroiwa et al., "Relationship between the mobility of phosphocholine headgroups of liposomes and the hydrophobicity at the membrane interface: a characterization with spectrophotometric measurements," *Colloids and Surfaces B: Biointerfaces*, vol. 88, no. 1, pp. 221–230, 2011.
- [13] D. Laage, T. Elsaesser, and J. T. Hynes, "Water dynamics in the hydration shells of biomolecules," *Chemical Reviews*, vol. 117, no. 16, pp. 10694–10725, 2017.
- [14] D. Eisenberg and W. Kauzmann, *The Structure and Properties of Water: 4. Properties of Liquid Water*, Oxford University Press, Oxford, UK, 1969.
- [15] L. Comez, M. Paolantoni, P. Sassi, S. Corezzi, A. Morresi, and D. Fioretto, "Molecular properties of aqueous solutions: a focus on the collective dynamics of hydration water," *Soft Matter*, vol. 12, no. 25, pp. 5501–5514, 2016.
- [16] D. Vlieghe, J. P. Turkenburg, and L. Van Meervelt, "B-DNA at atomic resolution reveals extended hydration patterns," *Acta Crystallographica Section D Biological Crystallography*, vol. 55, no. 9, pp. 1495–1502, 1999.
- [17] R. D. Horace and R. E. Dickerson, "Structure of a B-DNA dodecamer," *Journal of Molecular Biology*, vol. 151, no. 3, pp. 535–556, 1981.
- [18] D. P. Tieleman, S. J. Marrink, and H. J. C. Berendsen, "A computer perspective of membranes: molecular dynamics studies of lipid bilayer systems," *Biochimica et Biophysica Acta (BBA)-Reviews on Biomembranes*, vol. 1331, no. 3, pp. 235–270, 1997.
- [19] L. M. Alarcón, M. de los Angeles Frías, M. A. Morini, M. Belén Sierra, G. A. Appignanesi, and E. A. Disalvo, "Water populations in restricted environments of lipid membrane interphases," *European Physical Journal E*, vol. 39, no. 10, 2016.
- [20] F. Foglia, M. J. Lawrence, C. D. Lorenz, and S. E. McLain, "On the hydration of the phosphocholine headgroup in aqueous solution," *Journal of Chemical Physics*, vol. 133, no. 14, article 145103, 2010.
- [21] D. I. Svergun, S. Richard, M. H. J. Koch, Z. Sayers, S. Kuprin, and G. Zaccai, "Protein hydration in solution: experimental observation by X-ray and neutron scattering," *Proceedings of the National Academy of Sciences*, vol. 95, no. 5, pp. 2267–2272, 1998.
- [22] M. H. J. Koch, P. Vachette, and D. I. Svergun, "Small-Angle scattering: a view on the properties, structures and structural changes of biological macromolecules in solution," *Quarterly Reviews of Biophysics*, vol. 36, no. 2, pp. 147–227, 2003.
- [23] F. Merzel and J. C. Smith, "Is the first hydration shell of lysozyme of higher density than bulk water?," *Proceedings of the National Academy of Sciences*, vol. 99, no. 8, pp. 5378–5383, 2002.

- [24] T. J. Zwang, W. R. Fletcher, T. J. Lane, and M. S. Johal, "Quantification of the layer of hydration of a supported lipid bilayer," *Langmuir*, vol. 26, no. 7, pp. 4598–4601, 2010.
- [25] S. Salentinig, H. Amenitsch, and A. Yaghmur, "In situ monitoring of nanostructure formation during the digestion of mayonnaise," *ACS Omega*, vol. 2, no. 4, pp. 1441–1446, 2017.
- [26] Y. Maréchal, "The molecular structure of liquid water delivered by absorption spectroscopy in the whole IR region completed with thermodynamics data," *Journal of Molecular Structure*, vol. 1004, no. 1-3, pp. 146–155, 2011.
- [27] F. Perakis, L. De Marco, A. Shalit et al., "Vibrational spectroscopy and dynamics of water," *Chemical Reviews*, vol. 116, no. 13, pp. 7590–7607, 2016.
- [28] D. E. Otten and R. J. Saykally, "Spectroscopy and modeling of aqueous interfaces," *Società Italiana di Fisica*, vol. 15, 2015.
- [29] Y. E. Shen, *Fundamentals of Sum Frequency Spectroscopy*, Cambridge University Press, Cambridge, UK, 2016.
- [30] G. E. Walrafen, "The physics and physical chemistry of water," in *Raman and Infrared Spectral Investigations of Water Structure*, F. Franks, Ed., Springer, Boston, MA, USA, 1972.
- [31] N. A. Chumaevskii and M. N. Rodnikova, "Some peculiarities of liquid water structure," *Journal of Molecular Liquids*, vol. 106, no. 2-3, pp. 167–177, 2003.
- [32] G. E. Walrafen, "Raman spectral studies of HDO in H₂O," *Journal of Chemical Physics*, vol. 48, no. 1, pp. 244–251, 1968.
- [33] G. E. Walrafen, "Raman spectral studies of the effects of perchlorate ion on water structure," *Journal of Chemical Physics*, vol. 52, no. 8, pp. 4176–4198, 1970.
- [34] G. E. Walrafen, "Raman spectrum of water: transverse and longitudinal acoustic modes below .apprxeq.300 Cm-1 and optic modes above .apprxeq.300 Cm-1," *Journal of Physical Chemistry*, vol. 94, no. 6, pp. 2237–2239, 1990.
- [35] E. A. Disalvo and M. A. Frias, "Water state and carbonyl distribution populations in confined regions of lipid bilayers observed by FTIR spectroscopy," *Langmuir*, vol. 29, no. 23, pp. 6969–6974, 2013.
- [36] Q. Li, T. Li, J. Wu, and N. Zhou, "Comparative study on the structure of water in reverse micelles stabilized with sodium bis(2-ethylhexyl) sulfosuccinate or sodium bis(2-ethylhexyl) phosphate in n-heptane," *Journal of Colloid and Interface Science*, vol. 229, no. 1, pp. 298–302, 2000.
- [37] C. Choe, J. Lademann, and M. E. Darvin, "Depth profiles of hydrogen bound water molecule types and their relation to lipid and protein interaction in the human stratum corneum in vivo," *Analyst*, vol. 141, no. 22, pp. 6329–6337, 2016.
- [38] A. Abragam, *The Principles of Nuclear Magnetism*, Oxford University Press, Oxford, UK, 1961.
- [39] S. Kaieda and B. Halle, "Internal water and microsecond dynamics in Myoglobin," *Journal of Physical Chemistry B*, vol. 117, no. 47, pp. 14676–14687, 2013.
- [40] R. B. Fenwick, D. Oyen, H. J. Dyson, and P. E. Wright, "Slow dynamics of tryptophan-water networks in proteins," *Journal of the American Chemical Society*, vol. 140, no. 2, pp. 675–682, 2018.
- [41] A. R. Bizzarri and S. Cannistraro, "Molecular dynamics of water at the Protein-Solvent interface," *Journal of Physical Chemistry B*, vol. 106, no. 26, pp. 6617–6633, 2002.
- [42] E. Duboué-Dijon, A. C. Fogarty, J. T. Hynes, and D. Laage, "Dynamical disorder in the DNA hydration shell," *Journal of the American Chemical Society*, vol. 138, no. 24, pp. 7610–7620, 2016.
- [43] R. Abseher, H. Schreiber, and O. Steinhauser, "The influence of a protein on water dynamics in its vicinity investigated by molecular dynamics simulation," *Proteins: Structure, Function, and Genetics*, vol. 25, no. 3, pp. 366–378, 1996.
- [44] D. K. George, A. Charkhesht, O. A. Hull et al., "New insights into the dynamics of zwitterionic micelles and their hydration waters by gigahertz-to-terahertz dielectric spectroscopy," *Journal of Physical Chemistry B*, vol. 120, no. 41, pp. 10757–10767, 2016.
- [45] F. Persson, P. Söderhjelm, and B. Halle, "How proteins modify water dynamics," *Journal of Chemical Physics*, vol. 148, no. 21, article 215103, 2018.
- [46] F. Persson and B. Halle, "Compressibility of the protein-water interface," *Journal of Chemical Physics*, vol. 148, no. 21, article 215102, 2018.
- [47] O. Fiset, C. Päslock, R. Barnes et al., "Hydration dynamics of a peripheral membrane protein," *Journal of the American Chemical Society*, vol. 138, no. 36, pp. 11526–11535, 2016.
- [48] Y. Nojima, Y. Suzuki, and S. Yamaguchi, "Weakly hydrogen-bonded water inside charged lipid monolayer observed with heterodyne-detected vibrational sum frequency generation spectroscopy," *Journal of Physical Chemistry C*, vol. 121, no. 4, pp. 2173–2180, 2017.
- [49] O. Björneholm, M. H. Hansen, A. Hodgson et al., "Water at interfaces," *Chemical Reviews*, vol. 116, no. 13, pp. 7698–7726, 2016.
- [50] E. Tyrode and J. F. D. Liljeblad, "Water structure next to ordered and disordered hydrophobic silane monolayers: a vibrational sum frequency spectroscopy study," *Journal of Physical Chemistry C*, vol. 117, no. 4, pp. 1780–1790, 2013.
- [51] C. Rønne, P. O. Åstrand, and S. Keiding, "THz spectroscopy of liquid H₂O and D₂O," *Physical Review Letters*, vol. 82, no. 14, pp. 2888–2891, 1999.
- [52] K. Arai, N. Sagawa, T. Shikata et al., "Pronounced dielectric and hydration/dehydration behaviors of monopolar poly(N-alkylglycine)s in aqueous solution," *Journal of Physical Chemistry B*, vol. 120, no. 37, pp. 9978–9986, 2016.
- [53] M. Hishida and K. Tanaka, "Long-range hydration effect of lipid membrane studied by terahertz time-domain spectroscopy," *Physical Review Letters*, vol. 106, no. 15, 2011.
- [54] S. Pal, N. Samanta, D. Das Mahanta, R. K. Mitra, and A. Chattopadhyay, "Effect of phospholipid headgroup charge on the structure and dynamics of water at the membrane interface: a terahertz spectroscopic study," *Journal of Physical Chemistry B*, vol. 122, no. 19, pp. 5066–5074, 2018.
- [55] D. van der Spoel, P. J. van Maaren, and H. J. C. Berendsen, "A systematic study of water models for molecular simulation: derivation of water models optimized for use with a reaction field," *Journal of Chemical Physics*, vol. 108, no. 24, pp. 10220–10230, 1998.
- [56] D. Laage, "A molecular jump mechanism of water re-orientation," *Science*, vol. 311, no. 5762, pp. 832–835, 2006.
- [57] D. Laage, G. Stirnemann, F. Sterpone, R. Rey, and J. T. Hynes, "Reorientation and allied dynamics in water and aqueous solutions," *Annual Review of Physical Chemistry*, vol. 62, no. 1, pp. 395–416, 2011.
- [58] K. Meister, S. Ebbinghaus, Y. Xu et al., "Long-range protein-water dynamics in hyperactive insect antifreeze proteins," *Proceedings of the National Academy of Sciences*, vol. 110, no. 5, pp. 1617–1622, 2012.
- [59] S. Ebbinghaus, S. J. Kim, M. Heyden et al., "An extended dynamical hydration shell around proteins," *Proceedings of the National Academy of Sciences*, vol. 104, no. 52, pp. 20749–20752, 2007.

- [60] B. Born, S. J. Kim, S. Ebbinghaus, M. Gruebele, and M. Havenith, "The terahertz dance of water with the proteins: the effect of protein flexibility on the dynamical hydration shell of ubiquitin," *Faraday Discuss*, vol. 141, pp. 161–173, 2008.
- [61] V. Conti Nibali and M. Havenith, "New insights into the role of water in biological function: studying solvated biomolecules using terahertz absorption spectroscopy in conjunction with molecular dynamics simulations," *Journal of the American Chemical Society*, vol. 136, no. 37, pp. 12800–12807, 2014.
- [62] S. Clerjon, J.-D. Daudin, and J.-L. Damez, "Water activity and dielectric properties of gels in the frequency range 200 MHz–6 GHz," *Food Chemistry*, vol. 82, no. 1, pp. 87–97, 2003.
- [63] S. Stevan Jr., L. Paiter, J. Galvão, D. Roque, and E. Chaves, "Sensor and methodology for dielectric analysis of vegetal oils submitted to thermal stress," *Sensors*, vol. 15, no. 10, pp. 26457–26477, 2015.
- [64] J. R. Lakowicz, *Principles of Fluorescence Spectroscopy*, Kluwer Academic/Plenum Publishers, New York, NY, USA, 1999.
- [65] A. Hawe, M. Sutter, and W. Jiskoot, "Extrinsic fluorescent dyes as tools for protein characterization," *Pharmaceutical Research*, vol. 25, no. 7, pp. 1487–1499, 2008.
- [66] G. M. Edelman and W. O. McClure, "Fluorescent probes and the conformation of proteins," *Accounts of Chemical Research*, vol. 1, no. 3, pp. 65–70, 2002.
- [67] Z. Guo, H. Rügger, R. Kissner, T. Ishikawa, M. Willeke, and P. Walde, "Vesicles as soft templates for the enzymatic polymerization of aniline," *Langmuir*, vol. 25, no. 19, pp. 11390–11405, 2009.
- [68] K. Suga, T. Tanabe, H. Tomita, T. Shimanouchi, and H. Umakoshi, "Conformational change of single-stranded RNAs induced by liposome binding," *Nucleic Acids Research*, vol. 39, no. 20, pp. 8891–8900, 2011.
- [69] T. Ishigami, K. Suga, and H. Umakoshi, "Chiral recognition of l-amino acids on liposomes prepared with l-phospholipid," *ACS Applied Materials & Interfaces*, vol. 7, no. 38, pp. 21065–21072, 2015.
- [70] L. Cwiklik, A. J. A. Aquino, M. Vazdar et al., "Absorption and fluorescence of PRODAN in phospholipid bilayers: a combined quantum mechanics and classical molecular dynamics study," *The Journal of Physical Chemistry A*, vol. 115, no. 41, pp. 11428–11437, 2011.
- [71] L. A. Bagatolli, "LAURDAN fluorescence properties in membranes: a journey from the fluorometer to the microscope," in *Fluorescent Methods to Study Biological Membranes*, pp. 3–35, Springer, Berlin, Heidelberg, 2012.
- [72] O. K. Gasymov and B. J. Glasgow, "ANS fluorescence: potential to augment the identification of the external binding sites of proteins," *Biochimica et Biophysica Acta (BBA)-Proteins and Proteomics*, vol. 1774, no. 3, pp. 403–411, 2007.
- [73] J.-R. Albani, "Fluorescence origin of 6,p-toluidinyl-naphthalene-2-sulfonate (TNS) bound to proteins," *Journal of Fluorescence*, vol. 19, no. 3, pp. 399–408, 2008.
- [74] L. A. Bagatolli and E. Gratton, "Two photon fluorescence microscopy of coexisting lipid domains in giant unilamellar vesicles of binary phospholipid mixtures," *Biophysical Journal*, vol. 78, no. 1, pp. 290–305, 2000.
- [75] L. Malacrida, S. Astrada, A. Briva, M. Bollati-Fogolin, E. Gratton, and L. A. Bagatolli, "Spectral phasor analysis of LAURDAN fluorescence in live A549 lung cells to study the hydration and time evolution of intracellular lamellar body-like structures," *Biochimica et Biophysica Acta (BBA)-Biomembranes*, vol. 1858, no. 11, pp. 2625–2635, 2016.
- [76] T. T. Bui, K. Suga, and H. Umakoshi, "Roles of sterol derivatives in regulating the properties of phospholipid bilayer systems," *Langmuir*, vol. 32, no. 24, pp. 6176–6184, 2016.
- [77] H. Umakoshi and K. Suga, "Use liposome as a designable platform for molecular recognition~from statistical separation to cognitive separation ~," *Solvent Extraction Research and Development, Japan*, vol. 20, pp. 1–13, 2013.
- [78] K. Suga and H. Umakoshi, "Detection of nanosized ordered domains in DOPC/DPPC and DOPC/Ch binary lipid mixture systems of large unilamellar vesicles using a TEMPO quenching method," *Langmuir*, vol. 29, no. 15, pp. 4830–4838, 2013.
- [79] J. Han, K. Suga, K. Hayashi, Y. Okamoto, and H. Umakoshi, "Multi-level characterization of the membrane properties of resveratrol-incorporated liposomes," *Journal of Physical Chemistry B*, vol. 121, no. 16, pp. 4091–4098, 2017.
- [80] M. Tanaka and A. Mochizuki, "Effect of water structure on blood compatibility? thermal analysis of water in poly(meth)acrylate," *Journal of Biomedical Materials Research*, vol. 68A, no. 4, pp. 684–695, 2004.
- [81] M. Tanaka, A. Mochizuki, N. Ishii, T. Motomura, and T. Hatakeyama, "Study of blood compatibility with poly(2-methoxyethyl acrylate). Relationship between water structure and platelet compatibility in poly(2-methoxyethylacrylate-co-2-hydroxyethylmethacrylate)," *Biomacromolecules*, vol. 3, no. 1, pp. 36–41, 2002.
- [82] A. C. Fogarty and D. Laage, "Water dynamics in protein hydration shells: the molecular origins of the dynamical perturbation," *Journal of Physical Chemistry B*, vol. 118, no. 28, pp. 7715–7729, 2014.
- [83] A. Rahman and F. H. Stillinger, "Molecular dynamics study of liquid water," *Journal of Chemical Physics*, vol. 55, no. 7, pp. 3336–3359, 1971.
- [84] F. H. Stillinger and A. Rahman, "Improved simulation of liquid water by molecular dynamics," *Journal of Chemical Physics*, vol. 60, no. 4, pp. 1545–1557, 1974.
- [85] M. P. Allen and D. J. Tildesley, *Computer Simulation of Liquids*, Clarendon Press, Oxford, UK, 1989.
- [86] B. J. Kirby, *Micro- and Nanoscale Fluid Mechanics: Transport in Microfluidic Devices*, Cambridge University Press, Cambridge, UK, 2010.
- [87] H. J. C. Berendsen, J. P. M. Postma, W. F. van Gunsteren, and J. Hermans, "Interaction models for water in relation to protein hydration," in *Intermolecular Forces*, pp. 331–342, Springer, Dordrecht, Netherlands, 1981.
- [88] A. Mogelhøj, A. K. Kelkkanen, K. T. Wikfeldt et al., "Ab initio van der Waals interactions in simulations of water alter structure from mainly tetrahedral to high-density-like," *Journal of Physical Chemistry B*, vol. 115, no. 48, pp. 14149–14160, 2011.
- [89] M. Matsumoto, A. Baba, and I. Ohmine, "Topological building blocks of hydrogen bond network in water," *Journal of Chemical Physics*, vol. 127, no. 13, article 134504, 2007.
- [90] M. Marchi, F. Sterpone, and M. Ceccarelli, "Water rotational relaxation and diffusion in hydrated lysozyme," *Journal of the American Chemical Society*, vol. 124, no. 23, pp. 6787–6791, 2002.
- [91] V. P. Voloshin, N. N. Medvedev, M. N. Andrews, R. R. Burri, R. Winter, and A. Geiger, "Volumetric properties of hydrated peptides: voronoi-delaunay analysis of molecular simulation runs," *Journal of Physical Chemistry B*, vol. 115, no. 48, pp. 14217–14228, 2011.

- [92] H. J. C. Berendsen, J. P. M. Postma, W. F. van Gunsteren, and J. Hermans, "Interaction models for water in relation to protein hydration," in *Intermolecular Forces*, B. Pullman, Ed., pp. 331–342, Springer, Netherlands, 1981.
- [93] L. Fumagalli, A. Esfandiari, R. Fabregas et al., "Anomalously low dielectric constant of confined water," *Science*, vol. 360, no. 6395, pp. 1339–1342, 2018.
- [94] H. Umeyama and K. Morokuma, "The origin of hydrogen bonding. An energy decomposition study," *Journal of the American Chemical Society*, vol. 99, no. 5, pp. 1316–1332, 1977.
- [95] Y. Ishihara, S. Okouchi, and H. Uedaira, "Dynamics of hydration of alcohols and diols in aqueous solutions," *Journal of the Chemical Society, Faraday Transactions*, vol. 93, no. 18, pp. 3337–3342, 1997.
- [96] J. N. Israelachvili and G. E. Adams, "Measurement of forces between two mica surfaces in aqueous electrolyte solutions in the range 0–100 nm," *Journal of the Chemical Society, Faraday Transactions 1: Physical Chemistry in Condensed Phases*, vol. 74, p. 975, 1978.
- [97] J. N. Israelachvili and R. M. Pashley, "Molecular layering of water at surfaces and origin of repulsive hydration forces," *Nature*, vol. 306, no. 5940, pp. 249–250, 1983.
- [98] S. Marčelja and N. Radic, "Repulsion of interfaces due to boundary water," *Chemical Physics Letters*, vol. 42, no. 1, pp. 129–130, 1976.
- [99] D. W. R. Gruen and S. Marčelja, "Spatially varying polarization in water. A model for the electric double layer and the hydration force," *Journal of the Chemical Society, Faraday Transactions 2*, vol. 79, no. 2, pp. 225–242, 1983.
- [100] J. Kurniawan, N.-N. Yin, G.-y. Liu, and T. L. Kuhl, "Interaction forces between ternary lipid bilayers containing cholesterol," *Langmuir*, vol. 30, no. 17, pp. 4997–5004, 2014.
- [101] J. Kurniawan and T. L. Kuhl, "Characterization of Solid-Supported dipalmitoylphosphatidylcholine membranes containing cholesterol," *Langmuir*, vol. 31, no. 8, pp. 2527–2532, 2015.
- [102] B. R. Shrestha and X. Banquya, "Hydration forces at solid and fluid biointerfaces," *Biointerphases*, vol. 11, no. 1, article 018907, 2016.
- [103] M. I. McCarthy, G. K. Schenter, C. A. Scamehorn, and J. B. Nicholas, "Structure and dynamics of the water/MgO interface," *Journal of Physical Chemistry*, vol. 100, no. 42, pp. 16989–16995, 1996.
- [104] L. Zhang, H. T. Davis, D. M. Kroll, and H. S. White, "Molecular dynamics simulations of water in a spherical cavity," *Journal of Physical Chemistry*, vol. 99, no. 9, pp. 2878–2884, 1995.
- [105] M. Luckey, *Membrane Structural Biology with Biochemical and Biophysical Foundations*, Cambridge University Press, Cambridge, UK, 2012.
- [106] J. A. Mondal, S. Nihonyanagi, S. Yamaguchi, and T. Tahara, "Three distinct water structures at a zwitterionic lipid/water interface revealed by heterodyne-detected vibrational sum frequency generation," *Journal of the American Chemical Society*, vol. 134, no. 18, pp. 7842–7850, 2012.
- [107] S. Damodaran, "Water activity at interfaces and its role in regulation of interfacial enzymes," *Colloids and Surfaces B: Biointerfaces*, vol. 11, no. 5, pp. 231–237, 1998.
- [108] C. F. Lopez, S. O. Nielsen, M. L. Klein, and P. B. Moore, "Hydrogen bonding structure and dynamics of water at the dimyristoylphosphatidylcholine lipid bilayer surface from a molecular dynamics simulation†," *Journal of Physical Chemistry B*, vol. 108, no. 21, pp. 6603–6610, 2004.
- [109] F. Szoka and D. Papahadjopoulos, "Comparative properties and methods of preparation of lipid vesicles (Liposomes)," *Annual Review of Biophysics and Bioengineering*, vol. 9, no. 1, pp. 467–508, 1980.
- [110] G. Cevc and D. Gebauer, "Hydration-driven transport of deformable lipid vesicles through fine pores and the skin barrier," *Biophysical Journal*, vol. 84, no. 2, pp. 1010–1024, 2003.
- [111] C. Branca, S. Magazù, G. Maisano, F. Migliardo, P. Migliardo, and G. Romeo, "Hydration study of PEG/water mixtures by quasi elastic light scattering, acoustic and rheological measurements," *Journal of Physical Chemistry B*, vol. 106, no. 39, pp. 10272–10276, 2002.
- [112] F. Lairion and E. A. Disalvo, "Effect of dipole potential variations on the surface charge potential of lipid membranes," *Journal of Physical Chemistry B*, vol. 113, no. 6, pp. 1607–1614, 2009.
- [113] E. A. Disalvo, A. M. Bouchet, and M. A. Frias, "Connected and isolated CH₂ populations in acyl chains and its relation to pockets of confined water in lipid membranes as observed by FTIR spectrometry," *Biochimica et Biophysica Acta (BBA)-Biomembranes*, vol. 1828, no. 8, pp. 1683–1689, 2013.
- [114] E. A. Disalvo, O. A. Pinto, M. F. Martini, A. M. Bouchet, A. Hollmann, and M. A. Frias, "Functional role of water in membranes updated: a tribute to tråuble," *Biochimica et Biophysica Acta (BBA)-Biomembranes*, vol. 1848, no. 7, pp. 1552–1562, 2015.
- [115] C. M. Talbott, I. Vorobyov, D. Borchman, K. G. Taylor, D. B. DuPré, and M. C. Yappert, "Conformational studies of sphingolipids by NMR spectroscopy. II. Sphingomyelin," *Biochimica et Biophysica Acta (BBA)-Biomembranes*, vol. 1467, no. 2, pp. 326–337, 2000.
- [116] T. Ysuda, M. A. Al Sazzad, N. Z. Jäntti, O. T. Pentikäinen, and J. P. Slotte, "The influence of hydrogen bonding on sphingomyelin/colipid interactions in bilayer membranes," *Biophysical Journal*, vol. 110, no. 2, pp. 431–440, 2016.
- [117] G. M'Baye, Y. Mély, G. Duportail, and A. S. Klymche, "Liquid ordered and gel phases of lipid bilayers: fluorescent probes reveal close fluidity but different hydration," *Biophysical Journal*, vol. 95, no. 3, pp. 1217–1225, 2008.
- [118] J. Dai, M. Alwarawrah, and J. Huang, "Instability of cholesterol clusters in lipid bilayers and the cholesterol's umbrella effect," *Journal of Physical Chemistry B*, vol. 114, no. 2, pp. 840–848, 2010.
- [119] J. Israelachvili and H. Wennerström, "Role of hydration and water structure in biological and colloidal interactions," *Nature*, vol. 379, no. 6562, pp. 219–225, 1996.
- [120] P. Claesson, A. M. Carmona-Ribeiro, and K. Kurihara, "Dihexadecyl phosphate monolayers: intralayer and interlayer interactions," *Journal of Physical Chemistry*, vol. 93, no. 2, pp. 917–922, 1989.
- [121] T. J. McIntosh and S. A. Simon, "Hydration force and bilayer deformation: a reevaluation," *Biochemistry*, vol. 25, no. 14, pp. 4058–4066, 2002.
- [122] E. A. Disalvo, F. Lairion, F. Martini et al., "Structural and functional properties of hydration and confined water in membrane interfaces," *Biochimica et Biophysica Acta (BBA)-Biomembranes*, vol. 1778, no. 12, pp. 2655–2670, 2008.
- [123] J. Lyklema, *Physical Chemistry of Biological Interfaces*, Marce Dekker, New York, NY, USA, 2000.
- [124] E. A. Disalvo, M. F. Martini, A. M. Bouchet, A. Hollmann, and M. A. Frias, "Structural and thermodynamic properties of water-membrane interphases: significance for peptide/

- membrane interactions,” *Advances in Colloid and Interface Science*, vol. 211, pp. 17–33, 2014.
- [125] R. J. Mashl, H. L. Scott, S. Subramaniam, and E. Jakobsson, “Molecular simulation of dioleoylphosphatidylcholine lipid bilayers at differing levels of hydration,” *Biophysical Journal*, vol. 81, no. 6, pp. 3005–3015, 2001.
- [126] F. Volke, S. Eisenblätter, J. Galle, and G. Klose, “Dynamic properties of water at phosphatidylcholine lipid-bilayer surfaces as seen by deuterium and pulsed field gradient proton NMR,” *Chemistry and Physics of Lipids*, vol. 70, no. 2, pp. 121–131, 1994.
- [127] F. Lairion and E. A. Disalvo, “Effect of phloretin on the dipole potential of phosphatidylcholine, phosphatidylethanolamine, and phosphatidylglycerol monolayers,” *Langmuir*, vol. 20, no. 21, pp. 9151–9155, 2004.
- [128] F. Lairion and E. A. Disalvo, “Effect of trehalose on the contributions to the dipole potential of lipid monolayers,” *Chemistry and Physics of Lipids*, vol. 150, no. 2, pp. 117–124, 2007.
- [129] J. H. Crowe, L. M. Crowe, J. F. Carpenter, and C. A. Wistrom, “Stabilization of dry phospholipid bilayers and proteins by sugars,” *Biochemical Journal*, vol. 242, no. 1, pp. 1–10, 1987.
- [130] S. Diaz, F. Amalfa, A. C. Biondi de Lopez, and E. A. Disalvo, “Effect of water polarized at the carbonyl groups of phosphatidylcholines on the dipole potential of lipid bilayers,” *Langmuir*, vol. 15, no. 15, pp. 5179–5182, 1999.
- [131] S. Diaz, F. Lairion, J. Arroyo, A. C. Biondi de Lopez, and E. A. Disalvo, “Contribution of phosphate groups to the dipole potential of dimyristoylphosphatidylcholine membranes,” *Langmuir*, vol. 17, no. 3, pp. 852–855, 2001.
- [132] K. Gawrisch, D. Ruston, J. Zimmerberg, V. A. Parsegian, R. P. Rand, and N. Fuller, “Membrane dipole potentials, hydration forces, and the ordering of water at membrane surfaces,” *Biophysical Journal*, vol. 61, no. 5, pp. 1213–1223, 1992.
- [133] P. K. J. Kinnunen, “Lipid bilayers as osmotic response elements,” *Cellular Physiology and Biochemistry*, vol. 10, no. 5–6, pp. 243–250, 2001.
- [134] J. Y. Lehtonen and P. K. Kinnunen, “Changes in the lipid dynamics of liposomal membranes induced by poly(ethylene glycol): free volume alterations revealed by inter- and intramolecular excimer-forming phospholipid analogs,” *Biophysical Journal*, vol. 66, no. 6, pp. 1981–1990, 1994.
- [135] T. Söderlund, J.-M. I. Alakoskela, A. L. Pakkanen, and P. K. J. Kinnunen, “Comparison of the effects of surface tension and osmotic pressure on the interfacial hydration of a fluid phospholipid bilayer,” *Biophysical Journal*, vol. 85, no. 4, pp. 2333–2341, 2003.
- [136] R. N. A. H. Lewis and R. N. McElhaney, *Infrared Spectroscopy of Biomolecules*, Wiley-Liss, New York, NY, USA, 1996.
- [137] M. A. Frías, A. Nicastro, N. M. C. Casado, A. M. Gennaro, S. B. Díaz, and E. A. Disalvo, “Arbutin blocks defects in the ripple phase of DMPC bilayers by changing carbonyl organization,” *Chemistry and Physics of Lipids*, vol. 147, no. 1, pp. 22–29, 2007.
- [138] M. A. Frías, S. B. Díaz, N. M. Ale, A. Ben Altabef, and E. A. Disalvo, “FTIR analysis of the interaction of arbutin with dimyristoyl phosphatidylcholine in anhydrous and hydrated states,” *Biochimica et Biophysica Acta (BBA)-Biomembranes*, vol. 1758, no. 11, pp. 1823–1829, 2006.
- [139] J. Y. Lehtonen and P. K. Kinnunen, “Poly(ethylene glycol)-induced and temperature-dependent phase separation in fluid binary phospholipid membranes,” *Biophysical Journal*, vol. 68, no. 2, pp. 525–535, 1995.
- [140] G. A. Senisterra, E. A. Disalvo, and J. J. Gagliardino, “Osmotic dependence of the lysophosphatidylcholine lytic action on liposomes in the gel state,” *Biochimica et Biophysica Acta (BBA)-Biomembranes*, vol. 941, no. 2, pp. 264–270, 1988.
- [141] T. Lazrak, A. Milon, G. Wolff et al., “Comparison of the effects of inserted C40- and C50-terminally dihydroxylated carotenoids on the mechanical properties of various phospholipid vesicles,” *Biochimica et Biophysica Acta (BBA)-Biomembranes*, vol. 903, no. 1, pp. 132–141, 1987.
- [142] D. A. Pink, S. McNeil, B. Quinn, and M. J. Zuckermann, “A model of hydrogen bond formation in phosphatidylethanolamine bilayers supported by NSERC of Canada (DAP, SM and MJZ) and the UCR St. Francis Xavier University (SM).1,” *Biochimica et Biophysica Acta (BBA)-Biomembranes*, vol. 1368, no. 2, pp. 289–305, 1998.
- [143] H. U. Gally, W. Niederberger, and J. Seelig, “Conformation and motion of the choline head group in bilayers of dipalmitoyl-3-sn-phosphatidylcholine,” *Biochemistry*, vol. 14, no. 16, pp. 3647–3652, 2002.
- [144] G. Hunter and T. Squier, “Phospholipid acyl chain rotational dynamics are independent of headgroup structure in unilamellar vesicles containing binary mixtures of dioleoylphosphatidylcholine and dioleoyl-phosphatidylethanolamine,” *Biochimica et Biophysica Acta (BBA)-Biomembranes*, vol. 1415, no. 1, pp. 63–76, 1998.
- [145] M. F. Martini and E. A. Disalvo, “Superficially active water in lipid membranes and its influence on the interaction of an aqueous soluble protease,” *Biochimica et Biophysica Acta (BBA)-Biomembranes*, vol. 1768, no. 10, pp. 2541–2548, 2007.
- [146] M. F. Martini and E. A. Disalvo, “Effect of polar head groups on the activity of aspartyl protease adsorbed to lipid membranes,” *Chemistry and Physics of Lipids*, vol. 122, no. 1–2, pp. 177–183, 2003.

Research Article

Investigation of the Thermal Performance of Salt Hydrate Phase Change of Nanoparticle Slurry Flow in a Microchannel

Safi A. Memon ¹, M. B. Sajid,² M. S. Malik ³, Awad B. S. Alquaity ⁴,
M. Mohib ur. Rehman,³ Taqi A. Cheema ³, Moon Kyu Kwak ¹ and Cheol Woo Park ¹

¹School of Mechanical Engineering, Kyungpook National University, 80 Daehakro, Bukgu, Daegu 41566, Republic of Korea

²U.S.-Pakistan Center for Advanced Studies in Energy (USPCAS-E), National University of Sciences and Technology (NUST), Sector H-12, Islamabad, Pakistan

³Faculty of Mechanical Engineering, Ghulam Ishaq Khan Institute of Engineering Sciences & Technology (GIKI), Topi, Pakistan

⁴Institute for Combustion Technology, RWTH Aachen University, Aachen 52056, Germany

Correspondence should be addressed to Cheol Woo Park; chwoopark@knu.ac.kr

Received 15 October 2018; Accepted 4 December 2018; Published 3 January 2019

Guest Editor: Hakjin Kim

Copyright © 2019 Safi A. Memon et al. This is an open access article distributed under the Creative Commons Attribution License, which permits unrestricted use, distribution, and reproduction in any medium, provided the original work is properly cited.

Computational study was conducted to investigate the thermal performance of water-based salt hydrate S44 nanoparticles as the phase change material (PCM) in a microchannel heat sink. Constant heat dissipation was applied on the top wall of the heat sink. Forced internal convection of the PCM slurry flow was performed through a homogeneous approach. Three thermal performance parameters, including effectiveness ratio, performance index, and Merit number, were used to quantify the cooling performance of S44 for various concentrations of the PCM nanoparticles. The thermal performance of the salt hydrate S44 slurry was also compared with a similar study conducted for lauric acid nanoparticle slurry found in the literature. Specific operating conditions were identified. The salt hydrate S44 would provide better thermal performance than lauric acid, and vice versa. Finally, Nusselt number correlations have been developed for the microchannel PCM heat sink for Reynolds numbers in the range 12.23 to 47.14 and Prandtl numbers in the range 3.74 to 5.30. A design guideline for manufacturing PCM particles and microchannel heat sinks is provided. With this guideline, the heat absorption ability of the heat sink is maximized, and the pumping power and the losses related to the addition of the particles are minimized.

1. Introduction

The miniaturization of electronic devices coupled with advances in microscale manufacturing technology has prompted studies on increased thermal management and cooling performance in microchannels. Several studies have aimed at solving different problems involving microchannel heat sinks. An emerging problem involving conventional microchannel heat sinks underscores their inability to meet the ever-increasing cooling requirement of modern micro-electronic devices, which can easily reach 10^5 W/cm³ [1]. Electronic devices must remain cool to reduce the logic gate switching time and improve the processing speeds. In an attempt to meet this challenge, phase change material (PCM) particles may be introduced in the fluid flow of microchannel heat sinks to increase their cooling capacity. PCM particles act as the thermal storage device by undergoing a solid-to-liquid

phase transformation when exposed to heat flux, thereby absorbing a large amount of heat. When thermal energy is required, PCM may be solidified, thereby releasing a large amount of energy. The key factor affecting heat transfer when a slurry containing PCM particles is introduced inside the microchannel is PCM's latent heat of fusion. The particles keep absorbing a large amount of heat from the electronic device until they are fully melted. Therefore, introducing PCM slurry inside a microchannel heat sink reduces the temperature difference along the microchannel length and increases the overall heat transfer coefficient.

Research on thermal management using PCM has evolved over the past two decades, as shown by the following studies: Goel et al. [2], Roy and Sengupta [3], Alvarado et al. [4], Hao and Tao [5], Kuravi et al. [6], Sabbah et al. [7], Kuravi et al. [8], Kondle et al. [9], Xing et al. [1], Alquaity et al. [10–12], Stritih [13], Wang et al. [14], Saha and Dutta

[15], and Shatikian et al. [16]. The following studies have been conducted on the PCM micro- and nanoparticle applications in heat exchangers: Goel et al. [2], Roy and Sengupta [3], Alvarado et al. [4], and Hao and Tao [5]. Goel et al. [2] studied microencapsulated particles of *n*-eicosane in a fully developed slurry flow with laminar flow regime in a circular channel that possesses a circular cross section under constant heat flux and temperature at the boundaries. By using slurry instead of pure fluid, a decrease of 50% was observed in the wall temperature. Roy and Sengupta's experiments used four different combinations, which were formed using two microencapsulated PCMs and two wall thicknesses [3]. They studied stability of the PCM heat sinks in thermal and structural terms and concluded that usage of microencapsulated particles in heat sinks is suitable for practical purposes. Alvarado et al. [4] experimentally studied turbulent flow in a copper channel with circular cross section under constant heat flux. The author concluded that concentration significantly contributed to the thermal storage of the microencapsulated PCM particles. Hao and Tao [5] computationally investigated the hydrodynamic characteristics along with the heat transfer of PCM slurry with micro- and nanosized PCM particles. Inclusion of PCM particles resulted in increase of heat transfer in the wall region. The application of PCM to microchannels is motivated by the advancement in microelectronic devices, thereby increasing thermal dissipation requirements of these devices, as indicated in the following studies: Kuravi et al. [6], Sabbah et al. [7], Kuravi et al. [8], Kondle et al. [9], Xing et al. [1], and Alqaity et al. [10–12]. The experimental and computational analyses performed by Kuravi et al. [6] investigated water-based PCM slurry flow containing *n*-octadecane microencapsulated particles through manifold microchannels. Thermal performance decreased in comparison with single fluid flow. However, the performance improved compared with single fluid flow when the hydraulic diameter of the channels decreased, and PCM with higher thermal conductivity was used. Sabbah et al. [7] conducted a 3D computational study of the microchannel PCM heat sink with microencapsulated PCM particles. The thermophysical properties of the slurry were assumed to be temperature dependent, and the thermal resistance of the microchannel walls was considered. The authors concluded that the heat sinks containing PCM slurry resulted in lower and more uniform temperatures across an electronic component when compared with heat sinks containing pure water. Kuravi et al. [8] computationally obtained the velocity and temperature profiles due to nanoencapsulated PCM in a 3D homogenous model of the microchannel with fin effect and longitudinal conduction along the microchannel. Kondle et al. [9] analyzed hydrodynamically developed laminar water-based *n*-eicosane slurry flow in different circular and rectangular microchannels using homogeneous models for the PCM slurry and a latent heat model to determine the effects of the phase change of the PCM on the heat transfer of the microchannel heat sink. Xing et al. [1] investigated the thermal performance of phase change slurry in microchannels with circular cross section. Governing equations were solved for the liquid and solid phases, and the

interactions among the PCM particles were considered. Maximum heat transfer across the microchannel PCM heat sink was found for ranges of heat flux and Reynolds numbers. Alqaity et al. [12] studied two computational models, namely, homogeneous and discrete phase models [17], to identify which one is more suitable for studying PCM slurry flow in microchannels. The discrete phase model incorrectly predicted the pressure drop when the concentration of PCM was increased; hence, the homogeneous model was used for further studies. Alqaity et al. [11] defined the Merit number to account for the irreversibility effects caused by heat transfer and fluid friction. Detailed parametric study was conducted in which the bottom plate heat flux, inlet mass flow rate, and PCM concentration were varied to evaluate the thermal performance of the PCM. Homogenous model was used to model the slurry flow, whereas the thermophysical properties of the bulk fluid were assumed to be constant. The authors concluded that an optimal ratio of heat flux to mass flow rate exists, for which the thermal performance of the heat sink is maximized. Many studies have determined Nusselt number correlations for PCM heat sinks, as follows: Stritih [13], Wang et al. [14], Saha and Dutta [15], and Shatikian et al. [16]. Stritih [13] studied the solidification and melting behaviors of finned paraffin-based PCM thermal storage unit and compared it with a similar unit without fins. The author obtained time-varying temperature distribution and developed Nusselt number correlations as a function of the Rayleigh number for both solidification and melting cases. Wang et al. [14] developed two empirical Nusselt number correlations for 4 mm diameter circular tubes by considering the laminar and turbulent flow of slurries containing 0% to 27.6% bromohexadecane by mass. The correlations predicted the Nusselt number with more than 90% accuracy. Saha and Dutta [15] computationally studied the cooling performance of thermal conductivity enhancers of plate-fin type in PCM heat sinks. The authors conducted in-depth parametric studies by varying the aspect ratio and heat flux associated with the flow channel to obtain thermal performance and Nusselt number correlations for the PCM heat sink. A single Nusselt number correlation was insufficient to account for all aspect ratios. Hence, the authors developed Nusselt number correlations for the PCM heat sink for different aspect ratios. Shatikian et al. [16] computationally studied the PCM behavior in a heat sink with vertical fins on its horizontal base. The PCM was stored between the fins, and a constant heat flux was applied at the horizontal base. Detailed parametric study was conducted. The thickness and height of the fins, thickness of the PCM layer, and heat flux varied. The transient behavior of the phase change was observed. The authors correlated the corresponding melt fractions and Nusselt numbers with Fourier, Stefan, and Rayleigh numbers. The current study aimed at analyzing the thermal performance of the microchannel PCM heat sink with salt hydrate S44 as the PCM [18]. The salt hydrate S44 is manufactured by PCM Products Ltd. in the form of standardized balls, tubes, and slabs stacked in underground or rooftop tanks for macroscale applications, such as refrigeration and free cooling, cryogenics, solar heating, heat

recovery, and industrial heating systems. The present study was aimed at acting as a feasibility study for production of S44 at the nanoscale for application in microchannel heat sinks by analyzing its performance through the computational method before its actual manufacturing.

For thermal performance analysis of the S44 slurries, the heat flux in the range of 8000 W/m^2 to $20,000 \text{ W/m}^2$ was applied. This range of heat flux values corresponds to the thermal dissipation characteristics of the fourth to the seventh generation of Intel® Core™ i3, i5, and i7 processors [19]. Each processor constitutes a $37.5 \text{ mm} \times 37.5 \text{ mm}$ chip and dissipates 8.75 W to 32.50 W of thermal power for each independent CPU embedded inside the chip, thereby resulting in heat flux values ranging from 6222 W/m^2 to $23,111 \text{ W/m}^2$. The aim of the study was achieved by first analyzing the thermal performance of the salt hydrate S44 slurry in a microchannel PCM heat sink under different values of mass flow rate, heat flux, and concentration of the PCM. Then, we compared the thermal performance of the salt hydrate S44 with a similar study from the literature conducted for lauric acid nanoparticle slurry [11]. Finally, we developed Nusselt number correlations for the microchannel PCM heat sink to predict the thermal performance of the slurry using the Reynolds and Prandtl numbers of the fluid.

2. Methodology

Microchannel heat sinks are generally placed at the bottom of the printed circuit boards containing various electrical components on its surface. These electrical elements dissipate heat that must be removed from the circuit board. For this purpose, small-scale heat sinks are attached at the bottom to extract the heat with a circulating fluid. Figure 1(a) shows the schematic of a 3D model of a heat sink with a microchannel at the bottom. The electrical elements act as a source of constant heat flux. The 35 mm long microchannel possesses $2 \text{ mm} \times 50 \mu\text{m}$ cross section. Given that the aspect ratio (B/H) of the cross section is 40, the microchannel PCM heat sink can be considered as having a 2D geometry for the purpose of the investigation [9]. Figure 1(b) shows the schematic of the 2D computational domain used in the present study. Water-based salt hydrate S44 nanoparticle PCM slurry enters the microchannel through an inlet at a specified temperature and mass flow rate. Exchange of thermal energy occurs between the slurry and the top wall of the microchannel before the slurry exits the microchannel through the outlet at a higher temperature.

2.1. Mathematical Modelling and Thermophysical Properties of the Bulk Fluid. The salt hydrate S44 is a PCM produced at the macroscale by PCM Products, Ltd., in the PlusICE range [18]. The present research was a step toward the determination of the performance of salt hydrate S44 at the microscale by computationally developing the Nusselt number correlations when it is used as PCM to improve the cooling performance of microchannel heat sinks. The salt hydrate S44 slurry inside the microchannel was modeled as bulk fluid using the homogeneous approach. Table 1 presents the thermophysical

properties of the homogeneous bulk fluid of S44 [18]. The literature suggests that the pressure drop can undergo significant deviation when the thermophysical properties remain constant with respect to temperature [11]. The pressure drop is an essential parameter that significantly contributes to the heat sink performance and helps determine the pumping requirement for the circulation of the cooling medium. Therefore, despite the expected longer computational time, the properties of the bulk fluid were assumed to be temperature dependent. The mathematical model of the PCM slurry flow inside the microchannel was a multiphysics model of fluid flow and heat transfer with phase change.

2.1.1. Fluid Flow Model. The conventional theory for continuum mechanics is applicable to the fluid flow inside microchannels with cross sections as small as $100 \mu\text{m}$ in width and $1.7 \mu\text{m}$ in height [20]. Therefore, Navier–Stokes equations can be used to model the flow inside the microchannel under consideration. The assumptions for the fluid flow model are as follows:

- (i) The distribution of the particles is homogeneous throughout the microchannel [8]
- (ii) The flow inside the microchannel is laminar and incompressible and at steady state [8]
- (iii) The fluid is considered Newtonian below the 0.10 volumetric ratio concentration [8]

The governing equations for the flow of the PCM slurry are the following continuity and momentum equations [21]:

$$\frac{\partial u}{\partial x} + \frac{\partial v}{\partial y} = 0,$$

$$\rho_b \left(u \frac{\partial u}{\partial x} + v \frac{\partial u}{\partial y} \right) = -\frac{\partial p}{\partial x} + \mu_b \left(\frac{\partial^2 u}{\partial x^2} + \frac{\partial^2 u}{\partial y^2} \right), \quad (1)$$

$$\rho_b \left(u \frac{\partial v}{\partial x} + v \frac{\partial v}{\partial y} \right) = -\frac{\partial p}{\partial y} + \mu_b \left(\frac{\partial^2 v}{\partial x^2} + \frac{\partial^2 v}{\partial y^2} \right),$$

where u and v are the fluid velocities along the x and y directions, respectively, ρ_b represents the effective density of the bulk fluid, μ_b is the effective dynamic viscosity of the bulk fluid, and p is the pressure.

Effective density ρ_b of the PCM slurry is computed as the weighted average of the densities of the PCM nanoparticles and the carrier fluid [7], as follows:

$$\rho_b = C\rho_p + (1 - C)\rho_f, \quad (2)$$

where ρ_p and ρ_f are the densities of the PCM particle and the carrier fluid, respectively, and C is the PCM volumetric ratio concentration in the slurry.

Effective viscosity μ_b of the PCM slurry is computed using Vand's correlation [22], which was experimentally validated by Fang et al. in [23], as follows:

$$\mu_b = (1 - C - 1.16C^2)^{-2.5} \mu_f, \quad (3)$$

where μ_f is the dynamic viscosity of the carrier fluid.

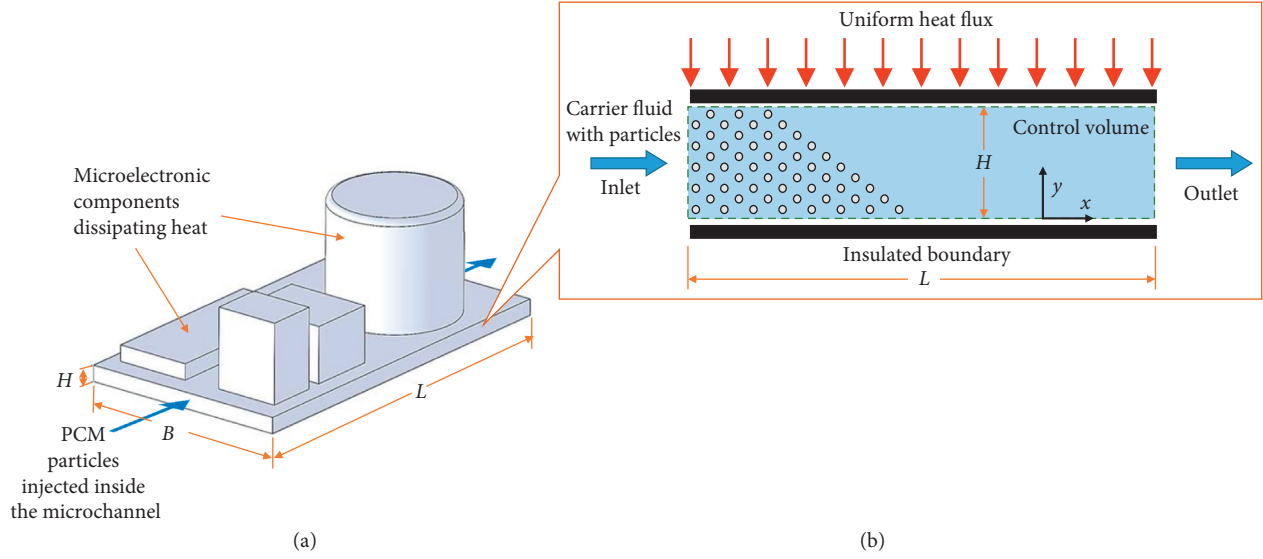


FIGURE 1: (a) 3D sketch of microchannel PCM heat sink and (b) 2D computational model.

TABLE 1: Thermophysical properties of the salt hydrate S44 [18].

PCM state	Density (kg/m ³)	Specific heat (kJ/kg·K)	Latent heat (kJ/kg)	Thermal conductivity (W/m·K)
Solid	1584	1.61	100	0.43
Liquid	—	1.61	—	0.43

2.1.2. Heat Transfer Model. Heat was transferred from the top wall where PCM changed its phase. The top wall had constant heat flux to the PCM slurry flowing through the microchannel. The physics of heat transfer with phase change was modeled using the energy equation of the convective heat transfer, assuming that the particles and the carrier fluid have the same velocity and temperature. Moreover, the thermophysical properties of the PCM slurry depend on the temperature. The 2D energy equation for the convection heat transfer [21] with negligible mechanical energy dissipation effects is as follows:

$$\rho_b c_b \left(u \frac{\partial T}{\partial x} + v \frac{\partial T}{\partial y} \right) = k_b \left(\frac{\partial^2 T}{\partial x^2} + \frac{\partial^2 T}{\partial y^2} \right), \quad (4)$$

where T represents the temperature distribution in the microchannel and u and v are the velocity components along the x and y axes, respectively. ρ_b and c_b are the density and specific heat of the bulk fluid, respectively. k_b is the effective thermal conductivity of the PCM slurry and a combination of the thermal conductivity of the particles k_p and carrier fluid k_f . k_b can be computed using Maxwell's relation [24], as follows:

$$k_b = k_f \frac{2 + (k_p/k_f) + 2C((k_p/k_f) - 1)}{2 + (k_p/k_f) - C((k_p/k_f) - 1)}, \quad (5)$$

where C is the PCM volumetric ratio concentration in the slurry.

2.1.3. Phase Change Model. Heat was transferred from the top surface of the microchannel to the carrier fluid containing

nanoparticles. These particles instantaneously melted to form a PCM slurry when the melting temperature is reached. During the phase change process, heat was stored in the PCM. The heat storage capacity of the PCM slurry can be determined by conducting an energy balance of the phase change process [7]. The energy balance model required the assumption of a piecewise function of specific heat correlation broken at the solidus and liquidus temperatures, which may be located with a difference of 0.5 K in either direction of the PCM melting temperature. The bulk fluid specific heat c_b can be modeled in various ways, depending on the particle temperature relative to the temperatures of the solidus and liquidus regions of the slurry. If the particle temperature was less than the solidus temperature, c_b was computed as follows:

$$c_b = \frac{C\rho_p c_{S,p} + (1-C)\rho_f c_f}{\rho_b}. \quad (6)$$

In case the temperature of the particles was greater than the solidus temperature but less than the liquidus temperature, c_b was modeled as a function of the specific heats of the solidus ($c_{S,p}$) and liquidus phases ($c_{L,p}$) and latent heat of fusion L_{fusion} , as follows:

$$c_b = \frac{C(c_{S,p} + c_{L,p})}{2} + \frac{CL_{\text{fusion}}}{T_{\text{liquidus}} - T_{\text{solidus}}} + \frac{(1-C)\rho_f c_f}{\rho_b}. \quad (7)$$

When the temperature of particle exceeded that of the liquidus phase, the correlation of the specific heat was as follows:

$$c_b = \frac{C\rho_p c_{L,p} + (1-C)\rho_f c_f}{\rho_b}. \quad (8)$$

3. Implementation of the Numerical Method

The mathematical model developed in the previous section was translated into a computational model for implementation. Discretization of the governing equations was conducted using the finite volume approach in ANSYS Fluent (V 16.1) [17]. All variables in the numerical solution were computed at each node, except for the velocities computed midway between the nodes. The pressure-based segregated algorithm, known as SIMPLE, was used to achieve pressure-velocity coupling in the governing equations [25]. Residuals were carefully monitored with convergence criteria of 10^{-9} for the continuity and momentum equations and 10^{-12} for the energy equation. Additionally, convergence was ensured by monitoring the temperature at the outlet throughout the simulations.

3.1. Mesh Properties and Mesh Independence Study. A staggered 2D grid consisting of rectangular and triangular elements was used in the study. A fine mesh was kept near the top and bottom regions to accurately capture the flow property gradients normal to the flow direction. Mesh independence study was conducted by computing local Nusselt numbers along the length of the microchannel for the grid resolutions of 8×5600 , 10×7000 , and 12×8400 as shown in Figure 2. The maximum difference between the Nusselt numbers for different grid resolutions was 0.086. Therefore, the grid resolution of 10×7000 was used in further simulations.

3.2. Model Validation. The computational model was compared with that of the experimental study of Goel et al. [2]. A model with a circular channel that is 3.14 mm in diameter was considered to possess a wall temperature profile. The same experimental conditions, such as Reynolds number of 200, Stefan number of 2, and PCM volumetric ratio concentration of 0.10, were used for the comparison. Comparison between experimental and computational values of the wall temperature along the microchannel has been shown in Figure 3. Evidently, both studies are in agreement with a 1.23% maximum percentage difference between the two temperatures.

4. Results and Discussion

The developed numerical model was simulated using ANSYS Fluent (V. 16.1) [17]. Results were postprocessed to obtain the performance parameters and development of the Nusselt number correlations.

4.1. Thermal Performance Evaluation of Salt Hydrate S44. Heat flux and mass flow rate were varied to investigate the performance of the microchannel heat sink. Given that both parameters are critical to the heat transfer, the combined effects on the three performance parameters—effectiveness ratio, performance index, and Merit number—were obtained in the form of heat flux to mass flow rate ratio.

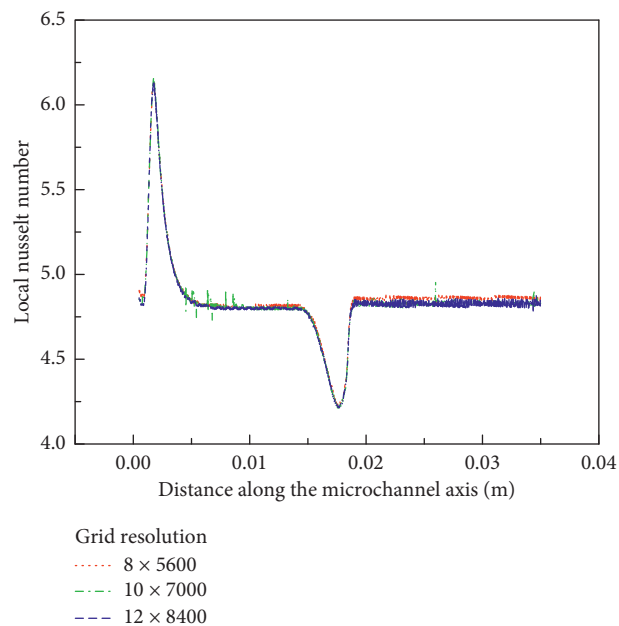


FIGURE 2: Local Nusselt number variations along the microchannel axis for different mesh resolutions.

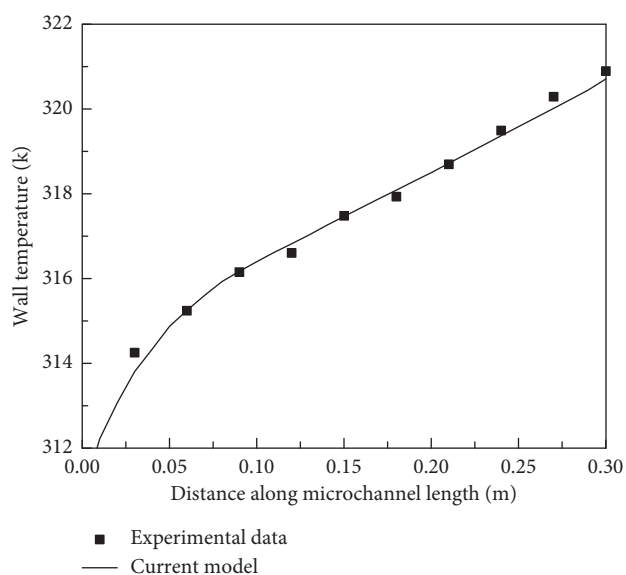


FIGURE 3: Validation of the computational model against experimental data [2].

4.1.1. Effectiveness Ratio. Effectiveness ratio is a measure of the heat transfer enhancement caused by the addition of the PCM nanoparticles to the carrier fluid [1]. It can be quantified as the ratio of the rate of heat transfer of bulk fluid and the rate of heat transfer of the carrier fluid. It is given as follows:

$$\varepsilon_{\text{eff}} = \frac{Q_b}{Q_f}, \quad (9)$$

where Q_b and Q_f are the heat transfer rates of the bulk fluid and the carrier fluid, respectively. They are calculated as follows:

$$\begin{aligned} Q_b &= q'' \times A, \\ Q_f &= \dot{m}c_f\Delta T, \end{aligned} \quad (10)$$

where q'' is the top wall heat flux in W/m^2 , A is the area of the top wall in m^2 , \dot{m} is the mass flow rate in kg/s , c_f is the specific heat of the carrier fluid in $J/kg\cdot K$, and ΔT is the temperature rise along the microchannel length in Kelvin.

Figure 4 shows the effect of heat flux per unit mass flow rate of the bulk fluid for various concentrations of the salt hydrate S44 on the effectiveness ratio. When the particles started melting in the microchannel, the effectiveness ratio reached the maximum value because of the highest ratio of sensible heat to latent heat of the bulk fluid. For this peak value of the effectiveness ratio, the largest length was that along which the particles melt inside the microchannel. Given that the sensible heat region near the inlet of the microchannel cannot be avoided, the maximum value of the effectiveness ratio corresponded to the circumstance when the sensible heat region at the inlet was minimized, and the remaining distance inside the microchannel was covered by the latent heat region. This configuration ensured minimal temperature increase between the inlet and the outlet regions of the microchannel. Hence, for a given concentration of the PCM, an optimal ratio of the heat flux to mass flow rate existed in a region where the largest amount of heat transfer occurred for minimum temperature increase along the heat sink. Consequently, a value below this optimal value indicated that the particles were not completely melted inside the microchannel. Moreover, this optimal value minimized the sensible region near the inlet, and the particles melted just before the outlet. However, a heat flux per unit mass flow rate above the optimal value showed that the particles melted earlier on the inside of the microchannel. A region of sensible heat was left at the end of the microchannel, thereby indicating a nonoptimised design of the microchannel under the given operating conditions. Furthermore, the plot of effectiveness ratio for bulk fluid containing lauric acid as the PCM nanoparticle was presented in Figure 5 for a performance comparison between lauric acid and S44. It is suggested that the slurry with lauric is able to absorb slightly more heat dissipated from the electronic components in comparison with S44.

4.1.2. Performance Index. Performance index is defined as the ratio of the heat transfer rate per unit pumping power of the bulk fluid to the heat transfer rate per unit pumping power of the carrier fluid [1]. The performance index helps the manufacturer in deciding the amount of pumping power and is given as follows:

$$\text{performance index} = \frac{(Q_b/P_b)}{(Q_f/P_f)}, \quad (11)$$

where P_b and P_f are the pumping powers of the bulk and the carrier fluid, respectively, and can be computed as follows:

$$\begin{aligned} P_b &= \Delta p_b u_b A, \\ P_f &= \Delta p_f u_f A, \end{aligned} \quad (12)$$

where Δp_b and Δp_f are the pressure drops in case of the bulk and the carrier fluid, respectively, in atm; A is the top wall area in m^2 ; and u_b and u_f are the velocities of the bulk and

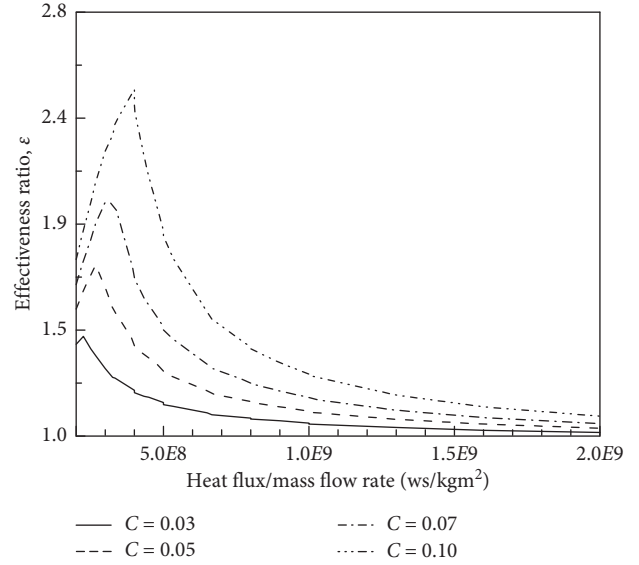


FIGURE 4: Effect of heat flux per unit mass flow rate on the effectiveness ratio at various concentrations of S44 PCM slurry.

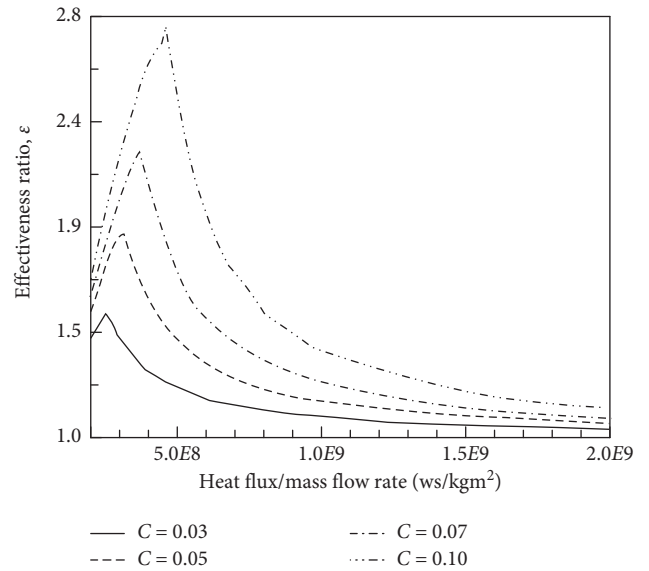


FIGURE 5: Effect of heat flux per unit mass flow rate on the effectiveness ratio for various concentrations of lauric acid slurry [11].

the carrier fluid, respectively, in m/s . The pressure drop of the carrier fluid can be computed using the Reynolds number Re_f calculated based on the hydraulic diameter D_h of the microchannel, as follows:

$$\begin{aligned} \Delta p_f &= \frac{32L\rho_f u_f^2}{Re_f D_h}, \\ Re_f &= \frac{\rho_f u_f D_h}{\mu_f}, \end{aligned} \quad (13)$$

where ρ_f is the density of the carrier fluid in kg/m^3 , L is the microchannel length in meters, and μ_f is the dynamic viscosity of the carrier fluid in $Pa\cdot s$.

Figure 6 shows the effect of the heat flux per unit mass flow rate on the performance index for various concentrations of

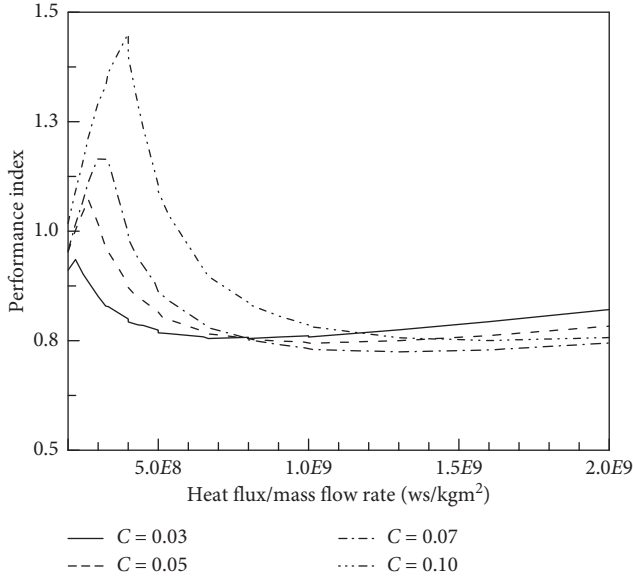


FIGURE 6: Effect of heat flux per unit mass flow rate on the performance index for various concentrations of S44 PCM slurry.

S44. The performance index exhibited a similar pattern when the heat flux to mass flow rate ratio is increased. However, the fluid with smaller particle concentration performs better than those with higher concentration for higher heat flux per unit mass flow rate values. This anomaly in the trend indicated the effect of pressure drop caused by the larger concentrations of S44 in the carrier fluid, and a new expression for the performance index was considered, as follows:

$$\text{performance index} = \frac{\epsilon_{\text{eff}}}{\Delta p_b} \times \frac{P_f}{u_b A} \quad (14)$$

This expression shows the direct relationship between performance index and effectiveness ratio. However, the performance index was inversely related to the pressure drop along the microchannel. The increase in pressure drop with increase in the heat flux to mass flow rate ratio may be attributed to the decrease in the temperature gradient along the length of the microchannel with increasing PCM concentration. Vand's correlation, as given in equation (3), shows that the viscosity decreases with rise in temperature. Therefore, at a higher value of heat flux per unit mass flow rate, a lower rate of increase in the effectiveness ratio with respect to the increase in PCM concentration resulted in higher temperature increase rate, thereby decreasing viscosity at a high rate and resulting in a higher increase of pressure drop rate. At higher values of heat flux per unit mass flow rate, the rate of increase in the effectiveness ratio with respect to the PCM concentration was lower than the rate of increase of the pressure drop. Therefore, as predicted by equation (14), the performance index was lower for higher PCM concentrations at higher values of heat flux per unit mass flow rate. Figure 7 provides the performance index plot of the bulk fluid containing lauric acid as PCM. The comparison clearly showed that the heat transfer rate per fluid pumping power of S44 is higher than that of the lauric acid slurry flow for the considered operating conditions. Hence, S44 provided more practical option as a PCM slurry selection for the objectives of this study.

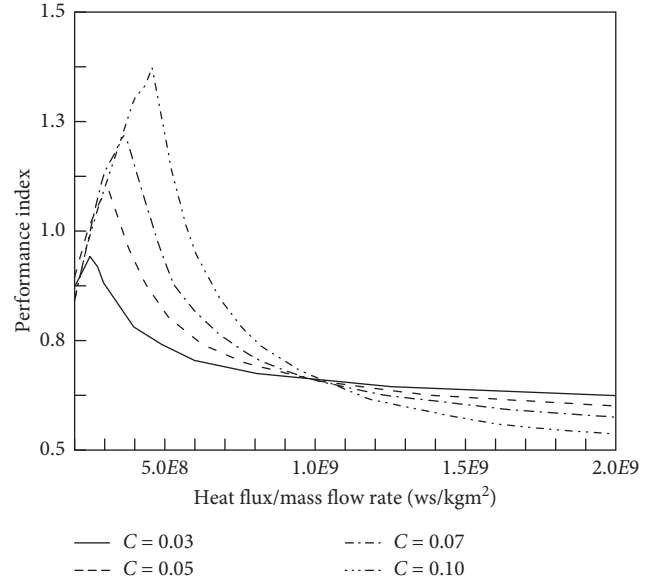


FIGURE 7: Effect of heat flux per unit mass flow rate on the performance index for various concentrations of lauric acid slurry [11].

4.1.3. *Merit Number.* Merit number is the measure of the irreversibility of the heat transfer and frictional losses because of the addition of PCM nanoparticles. It is defined as the ratio of the gain in heat transfer due to the process of addition of PCM particles to the sum of heat transferred at the top wall of the microchannel and the irreversibility [11]. Such irreversibility can be the reason for using the volumetric entropy generation rate S_{gen}'' (in $\text{W}/\text{m}^3 \cdot \text{K}$), as follows:

$$S_{\text{gen}}''' = \frac{k_b}{T^2} \left[\left(\frac{\partial T}{\partial x} \right)^2 + \left(\frac{\partial T}{\partial y} \right)^2 \right] + \frac{\mu_b}{T} \left(\frac{\partial u}{\partial y} \right)^2, \quad (15)$$

where k_b is the thermal conductivity of the bulk fluid in $\text{W}/\text{m} \cdot \text{K}$ and μ_b is the dynamic viscosity bulk fluid in $\text{Pa} \cdot \text{s}$.

Hence, the Merit number is given as follows:

$$M = \frac{Q_{\text{gain}}}{Q_b + \dot{I}}, \quad (16)$$

where Q_{gain} is the gain rate of heat absorption into the slurry due to addition of the particles (W) and \dot{I} is the rate of irreversibility (W). It can be computed as follows:

$$Q_{\text{gain}} = Q_b - Q_f = Q_f (\epsilon_{\text{eff}} - 1), \quad (17)$$

$$\dot{I} = S_{\text{gen,avg}}''' \times \text{volume} \times T_{\text{ref}}$$

where the reference temperature T_{ref} is maintained at 298 K.

Figure 8 shows the effect of heat flux per unit mass flow rate on the Merit number for various concentrations of S44 in the bulk fluid. Merit number also shows a similar trend with increasing heat flux per unit mass flow rate as in the previous cases of effectiveness ratio and performance index. However, the increase in concentration reduced the irreversibility, demonstrating the improvement in heat transfer. The increasing heat flux per unit mass flow rate hinted at the increase in irreversibility. In an adverse situation, this trend of continuous decrease in the Merit number may lead to zero. Therefore, a reasonable heat flux per unit mass flow

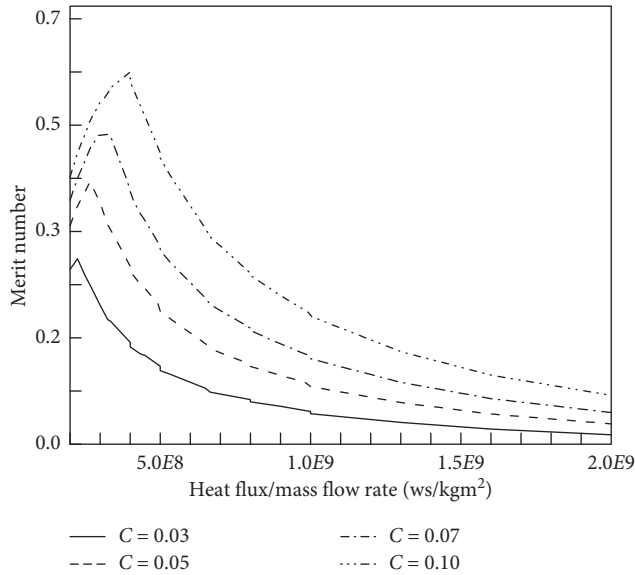


FIGURE 8: Effect of heat flux per unit mass flow rate on the Merit number for various concentrations of S44 slurry.

rate combination must be adopted to minimize irreversibility, especially with increasing PCM concentration. A comparison between the Merit number of lauric acid and S44 under the same conditions suggests that the lauric acid slurry offers marginally less losses than the S44 slurry at the same concentration (Figure 9).

4.2. Development of Nusselt Number Correlations. Any problem of convection is essentially a problem of computing the heat transfer coefficient [21]. Nusselt number \overline{Nu}_L is the nondimensionalized form of the heat transfer coefficient and may be correlated with Reynolds number Re and the Prandtl number Pr of the convective fluid flow by equations of the form $\overline{Nu}_L = f(Re, Pr)$. In order to obtain the Nusselt number correlations for the microchannel PCM heat sink, the data from the study were correlated in terms of averaged Nusselt, Reynolds, and Prandtl numbers.

To develop the Nusselt number correlations for the PCM heat sink, sets of Prandtl number, Reynolds number, and Nusselt number for the convective flow inside the microchannel were obtained, corresponding to each individual operating condition. The Prandtl numbers ranged from 3.74 to 5.30, whereas the wall temperatures ranged between 316.5 and 332.4 K for the PCM concentrations under study. Each data point on the plot represents a unique set of operating conditions for the heat sink. The average Nusselt number was plotted against the average Reynolds number on the log-log scale as shown in Figure 10. The form of the plot obtained hints at the need for Prandtl number normalization. Therefore, the \overline{Nu}_L data set was normalized by the Prandtl number to the power 0.8 in order to obtain a linear assortment of the data points (Figure 11). The power law dependence was strictly suggested by this plot.

By inspection, each separate line in the plot shown in Figure 11 represents each of the four values of mass flow rates considered in this study. The four power laws thus

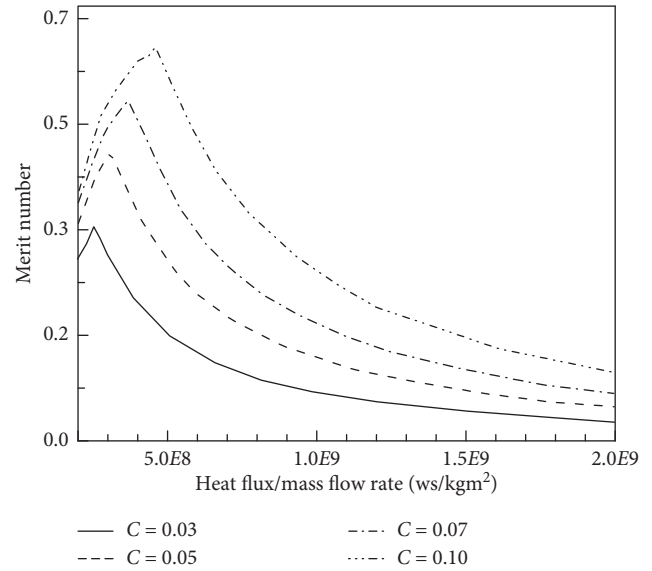


FIGURE 9: Effect of heat flux per unit mass flow rate on the Merit number for various concentrations of lauric acid slurry [11].

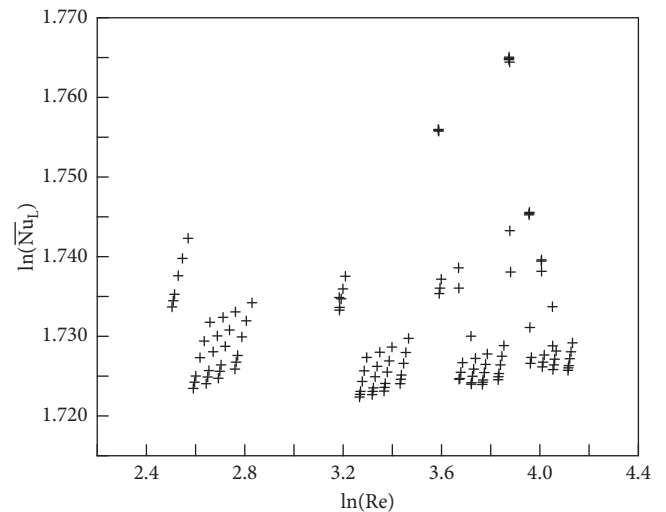


FIGURE 10: Average Nusselt number plotted against average Reynolds number of the slurry flow on the log-log scale.

obtained are the Nusselt number correlations listed in Table 2 along with the corresponding convective heat transfer coefficients for the microchannel PCM heat sink under study. In Table 2, \overline{Nu}_L represents the average Nusselt number, h represents the convective heat transfer coefficient in $W/m^2 \cdot K$, Re represents the Reynolds number, and Pr represents the Prandtl number. The developed convective heat transfer coefficient equations for the microchannel PCM heat sink prediction accuracies were 2.71%, 3.17%, 2.52%, and 3.20% for each range of the Reynolds number.

5. Conclusion

The thermal performance of the water-based salt hydrate S44 slurry flow through a microchannel heat sink was analyzed.

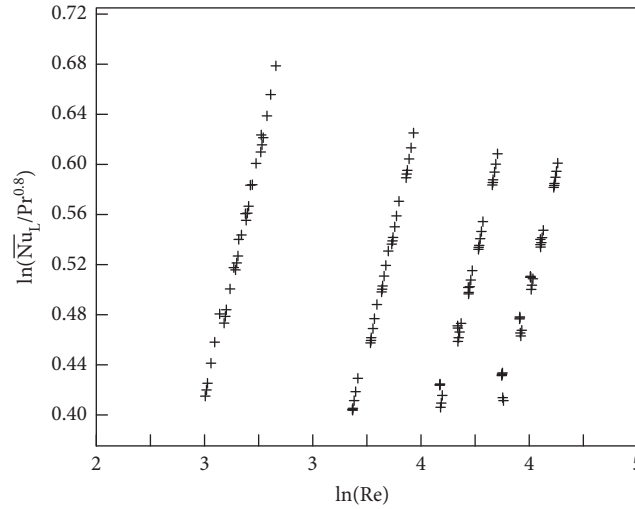


FIGURE 11: Average Nusselt number normalized by the Prandtl number to the power 0.8.

TABLE 2: Correlations for average Nusselt number and convective heat transfer coefficient for the microchannel PCM heat sink.

Range of the Reynolds number	$\overline{Nu}_L = A Re^B Pr^C$	$h = D Re^E Pr^F$ (W/m ² ·K)
12.23 < Re < 16.94	$\overline{Nu}_L = 0.213 Re^{0.783} Pr^{0.800}$	$h = 1380 Re^{0.783} Pr^{0.800}$
24.13 < Re < 32.00	$\overline{Nu}_L = 0.133 Re^{0.761} Pr^{0.800}$	$h = 856 Re^{0.761} Pr^{0.800}$
36.12 < Re < 47.14	$\overline{Nu}_L = 0.116 Re^{0.713} Pr^{0.800}$	$h = 745 Re^{0.713} Pr^{0.800}$
48.11 < Re < 62.29	$\overline{Nu}_L = 0.114 Re^{0.668} Pr^{0.800}$	$h = 731 Re^{0.668} Pr^{0.800}$

Pr: Prandtl number, such that $3.74 < Pr < 5$; q'' : the top plate heat flux, such that $8000 \text{ W/m}^2 < q'' < 20,000 \text{ W/m}^2$; T_w : wall temperature, such that $316.5 \text{ K} < T_w < 332.4 \text{ K}$.

Three performance parameters, namely, effectiveness ratio, performance index, and Merit number, were utilized to quantify the cooling performance of S44 for various concentrations of the PCM nanoparticles. A combined effect of heat flux and mass flow rate was examined in the form of heat flux per unit mass flow rate. Moreover, Nusselt number correlations were developed as a function of Reynolds and Prandtl numbers under a range of operating conditions.

The effectiveness ratio attained its peak value when the phase change region inside the microchannel was maximized. This configuration corresponded to the minimum temperature rise, thereby not only allowing maximum heat transfer to occur from the electronic component to the heat sink but also reducing the unnecessary thermal expansions that can damage the electronic component. Performance index helped the manufacturer determine the pumping power requirement based on the increase of pressure drop with increasing PCM concentration that was required for the electronic component for which the heat sink is to be designed. Given the heat flux of the electronic component, a mass flow rate for the slurry was set, thereby minimizing the power required to pump the slurry through the microchannel. A comparative analysis of the salt hydrate S44 with lauric acid showed that the latter slurry absorbed more heat flux than the former under the investigated operating conditions; however, this occurred at the cost of higher pumping power requirement. The losses due to the addition of the PCM particles were only marginally less in lauric acid than in S44 at the same concentration.

Nomenclature

A:	Microchannel cross-sectional area (m ²)
C:	Volumetric ratio concentration of PCM nanoparticles
c_p :	Isobaric specific heat (J·kg ⁻¹ ·K ⁻¹)
$c_{p,L}$:	Isobaric specific heat of the PCM particles in the solid state (J·kg ⁻¹ ·K ⁻¹)
$c_{p,S}$:	Isobaric specific heat of the PCM particles in the liquid state (J·kg ⁻¹ ·K ⁻¹)
\overline{Nu}_x :	Average Nusselt number over the interval (0, x)
D_h :	Hydraulic diameter (m)
\dot{I} :	Irreversibility rate (W)
h :	Convective heat transfer coefficient (W·m ⁻² ·K ⁻¹)
k :	Thermal conductivity (W·m ⁻¹ ·K ⁻¹)
L :	Microchannel length (m)
L_{fusion} :	Latent heat of fusion (J·kg ⁻¹)
\dot{m} :	Mass flow rate of PCM slurry (kg·s ⁻¹)
P :	Pumping power (W)
p :	Pressure (Pa)
Q :	Rate of heat transfer (W)
q'' :	Heat flux (W·m ⁻²)
S'' :	Volumetric entropy generation rate (W·m ⁻³ ·K ⁻¹)
T :	Temperature (K)
T_{in} :	Inlet temperature (K)
T_{out} :	Outlet temperature (K)
T_w :	Wall temperature (K)
T_{liquidus} :	Liquidus temperature (K)
T_{solidus} :	Solidus temperature (K)

u : Velocity along the x axis ($\text{m}\cdot\text{s}^{-1}$)
 v : Velocity along the y axis ($\text{m}\cdot\text{s}^{-1}$)
 ρ : Density ($\text{kg}\cdot\text{m}^{-3}$)
 μ : Dynamic viscosity ($\text{Pa}\cdot\text{s}$).

Subscripts

b: Bulk fluid
 f: Carrier fluid
 p: Particle.

Data Availability

The data used to support the findings of this study are included within the article.

Conflicts of Interest

The authors declare that they have no conflicts of interest.

Acknowledgments

This study was supported by the National Research Foundation of Korea (NRF), which is a grant funded by the Korea government (MSIP) (no. 2017R1A2B2005515).

References

- [1] K. Q. Xing, Y.-X. Tao, and Y. L. Hao, "Performance evaluation of liquid flow with PCM particles in microchannels," *Journal of Heat Transfer*, vol. 127, no. 8, pp. 931–940, 2005.
- [2] M. Goel, S. K. Roy, and S. Sengupta, "Laminar forced convection heat transfer in microcapsulated phase change material suspensions," *International Journal of Heat and Mass Transfer*, vol. 37, no. 4, pp. 593–604, 1994.
- [3] S. K. Roy and S. Sengupta, "An evaluation of phase change microcapsules for use in enhanced heat transfer fluids," *International Communications in Heat and Mass Transfer*, vol. 18, no. 4, pp. 495–507, 1991.
- [4] J. L. Alvarado, C. Marsh, C. Sohn, G. Phetteplace, and T. Newell, "Thermal performance of microencapsulated phase change material slurry in turbulent flow under constant heat flux," *International Journal of Heat and Mass Transfer*, vol. 50, no. 9–10, pp. 1938–1952, 2007.
- [5] Y. L. Hao and Y. X. Tao, "A numerical model for phase-change suspension flow in microchannels," *Numerical Heat Transfer, Part A: Applications*, vol. 46, no. 1, pp. 55–77, 2004.
- [6] S. Kuravi, J. Du, and L. C. Chow, "Encapsulated phase change material slurry flow in manifold microchannels," *Journal of Thermophysics and Heat Transfer*, vol. 24, no. 2, pp. 364–373, 2010.
- [7] R. Sabbah, M. M. Farid, and S. Al-Hallaj, "Micro-Channel Heat sink with slurry of water with micro-encapsulated phase change material: 3d-numerical study," *Applied Thermal Engineering*, vol. 29, no. 2–3, pp. 445–454, 2009.
- [8] S. Kuravi, K. M. Kota, J. Du, and L. C. Chow, "Numerical investigation of flow and heat transfer performance of nano-encapsulated phase change material slurry in microchannels," *Journal of Heat Transfer*, vol. 131, no. 6, article 062901, 2009.
- [9] S. Kondle, J. L. Alvarado, and C. Marsh, "Laminar flow forced convection heat transfer behavior of a phase change material fluid in microchannels," *Journal of Heat Transfer*, vol. 135, no. 5, article 052801, 2013.
- [10] A. B. S. Alqaity, S. A. Al-Dini, E. N. Wang, S. Z. Shuja, B. S. Yilbas, and K. J. Suabedissen, "Heat transfer enhancement in microchannel flow: presence of microparticles in a fluid," in *Proceedings of ASME 2010 8th International Conference on Nanochannels, Microchannels, and Minichannels: Parts A and B*, pp. 353–358, Montreal, QC, Canada, August 2010.
- [11] A. B. S. Alqaity, S. A. Al-Dini, E. N. Wang, and B. S. Yilbas, "Numerical investigation of liquid flow with phase change nanoparticles in microchannels," *International Journal of Heat and Fluid Flow*, vol. 38, pp. 159–167, 2012.
- [12] A. B. S. Alqaity, S. A. Al-Dini, and B. S. Yilbas, "Investigation into thermal performance of nanosized phase change material (PCM) in microchannel flow," *International Journal of Numerical Methods for Heat & Fluid Flow*, vol. 23, no. 2, pp. 233–247, 2013.
- [13] U. Stritih, "An experimental study of enhanced heat transfer in rectangular PCM thermal storage," *International Journal of Heat and Mass Transfer*, vol. 47, no. 12–13, pp. 2841–2847, 2004.
- [14] X. Wang, J. Niu, Y. Li et al., "Heat transfer of micro-encapsulated PCM slurry flow in a circular tube," *AIChE Journal*, vol. 54, no. 4, pp. 1110–1120, 2008.
- [15] S. K. Saha and P. Dutta, "Heat transfer correlations for PCM-based heat sinks with plate fins," *Applied Thermal Engineering*, vol. 30, no. 16, pp. 2485–2491, 2010.
- [16] V. Shatikian, G. Ziskind, and R. Letan, "Numerical investigation of a PCM-based heat sink with internal fins: constant heat flux," *International Journal of Heat and Mass Transfer*, vol. 51, no. 5–6, pp. 1488–1493, 2008.
- [17] ANSYS, *ANSYS FLUENT Theory Guide*, ANSYS, Inc., Canonsburg, PA, USA, 2010.
- [18] PCM Products Ltd., *PlusICE—Phase Change Materials*, PCM Products Ltd., Yaxley, UK, 2013.
- [19] Intel® product specifications, September 2018, <http://ark.intel.com/>.
- [20] S. G. Kandlikar and W. J. Grande, "Evolution of microchannel flow passage thermohydraulic performance and fabrication technology," *Heat Transfer Engineering*, vol. 24, no. 1, pp. 3–17, 2003.
- [21] P. I. Frank, D. Bergan, and A. Lavine, *Fundamentals of Heat and Mass Transfer*, John Wiley & Sons, Jefferson City, MO, USA, 2007.
- [22] V. Vand, "Theory of viscosity of concentrated suspensions," *Nature*, vol. 155, no. 3934, pp. 364–365, 1945.
- [23] Y. Fang, S. Kuang, X. Gao, and Z. Zhang, "Preparation of nanoencapsulated phase change material as latent functionally thermal fluid," *Journal of Physics D: Applied Physics*, vol. 42, no. 3, article 0305407, 2009.
- [24] J. Maxwell, *A Treatise on Electricity and Magnetism*, Dover Publications, New York, USA, 2008.
- [25] S. V. Patankar, *Numerical Heat Transfer and Fluid Flow*, Taylor & Francis Group, New York, USA, 1980.

Research Article

Continuous Fabrication of Wide-Tip Microstructures for Bio-Inspired Dry Adhesives via Tip Inking Process

Sung Ho Lee, Cheol Woo Park , and Moon Kyu Kwak 

School of Mechanical Engineering, Kyungpook National University, Daegu 41566, Republic of Korea

Correspondence should be addressed to Cheol Woo Park; chwoopark@knu.ac.kr and Moon Kyu Kwak; mkkwak@knu.ac.kr

Received 26 August 2018; Accepted 4 December 2018; Published 2 January 2019

Guest Editor: Hiroshi Umakoshi

Copyright © 2019 Sung Ho Lee et al. This is an open access article distributed under the Creative Commons Attribution License, which permits unrestricted use, distribution, and reproduction in any medium, provided the original work is properly cited.

In this paper, we report a new method for continuous fabrication of dry adhesives composed of microstructures with mushroom-shaped ends. Conventional mushroom microstructure fabrication is performed with a simple molding technique using a reversed phase master. In a typical fabrication process, thin- and wide-tip portions may be ripped during demolding, making it difficult to use in a continuous process. It is also difficult to apply the mushroom structure master to a continuous process system in roll form. Here, a continuous fabrication process was developed by applying the method of fabricating a wide tip using a tip inking method after forming a micropillar. Through the continuous process, the dry adhesive was successfully fabricated and the durability was measured with a reasonable pull-off strength (13 N/cm^2). In addition to the reasonable adhesion, high durability is guaranteed, and fabricated dry adhesives are expected to be used in various fields.

1. Introduction

Mushroom-shaped microstructure-based dry adhesives are expected to be applied in various fields, thanks to their unique properties, such as strong adhesive force, repeatability, durability, reversibility, and self-cleaning [1–9]. The application is evident not only in daily necessities but also in industries as a very strong adhesive on a smooth surface. The principle and properties of adhesion of dry adhesives are widely known through the body structure of various living organisms [10–12]. However, in order for dry adhesives to be widely used, the efficiency of the production process needs to be increased. Until now, dry adhesives have been made by fabricating a silicon master using a complex surface micromachining process and then replicating thermosetting or UV-curable resins [1–13]. In most dry adhesives, because of the larger spatula or mushroom shape, it was very difficult and costly to fabricate a silicon master [4, 14]. Even if the master was produced, it was difficult to effectively reproduce through soft lithography or nanoimprint. Because of the wide-tip structure, the tip was torn during the demolding process and the microstructure was often broken. The limitations of the production method

suggest that continuous production techniques that can increase productivity are considered to be more difficult. Recently, processes for realizing such continuous production have been developed. First, the existing roll-to-roll imprint system was applied to produce UV-curable resin with a mushroom structure to produce dry adhesives [7]. Most ultraviolet-curable resins have a very high elastic modulus after curing, making it difficult to ensure adhesion. In order to solve this problem, a UV-curable resin with a relatively low elastic modulus was used. As a result, a dry adhesive having a reasonable adhesive strength could be continuously produced. However, this method is very difficult to produce a mold with a negative mushroom shape in the form of a film, and further development is required for high-yield production. In order to overcome these material limitations, a continuous production process using thermosetting polymers has been developed [5]. Polydimethylsiloxane (PDMS), which is mainly used for dry adhesives, has a very good conformal contact property and has excellent adhesion performance when it is made with dry adhesives. This is because it has a low elastic modulus. By fabricating the structure, higher contact performance can be realized because low effective elastic modulus can be

achieved with these structures. However, since this material generally takes about 1 hour to cure, continuous production is difficult to achieve. Lee et al. have developed a technology that can produce a continuous roll-to-roll type by thinning the sample and increasing the curing temperature to shorten the time [5]. In order to produce a dry adhesive having a wide tip for high-performance adhesives, the resin must be completely filled with a mold having a negative tip structure. However, since the PDMS has a high viscosity, ~ 2000 cPs, it is difficult to continuously fill the resin. Also, both these methods can be used as general promising techniques to fabricate dry adhesives. The fabricated master mold can be used to easily produce a dry adhesive with a simple molding technique after a simple release layer treatment; however, it is hard to apply it in a roll-to-roll-based continuous production process due to some failures during demolding (e.g., tip tearing depending on the polymer used) [15]. Recently, a continuous production technique using a two-step UV-assisted molding process has been announced [16]. A simple columnar microstructure is produced by the roll-to-roll imprint technique, but the tip portion is partially cured by appropriately controlling the curing time and UV intensity. Subsequently, a mushroom-shaped microstructure was developed by forming a wide tip on the column through the subsequent pressing and planarizing process. This method eliminates the need for a complex master fabrication process and avoids any failure that can occur with demolding. Since the thickness of the uncured resin that can be used for tip widening is only a few microns through the partial curing process, there is a limit to make a wide tip. In this respect, dry adhesives made through a partial curing process are limited in application because wide tips are essential to ensure strong adhesion of dry adhesives.

In this paper, we introduce a simple micropillar structure and a method of forming additional parts by inking the tips. This fabrication method can also be applied to the roll-to-roll-based apparatus without any severe changes; thus, it is applied to the prototype roll-to-roll production equipment to test the continuous fabrication possibility. Moreover, the pull-off strength of the bio-inspired dry adhesive was measured. The measured adhesion strength of approximately 13 N/cm^2 is slightly lower than that of dry adhesives made by typical one-step molding with PDMS; nevertheless, this value is applicable for application. It also has an advantage when compared with the continuous process using partial curing mentioned above. The adhesion strength of fabricated dry adhesives is lower when PDMS material is used but not significantly lower when the same soft polyurethane acrylate (PUA) is used. In addition, higher adhesion can be achieved if the tip size can be widened in future optimization processes.

2. Materials and Methods

2.1. Polyurethane Acrylate (PUA). The PUA consisted of a functionalized prepolymer with acrylate groups for cross-linking, a monomeric modulator, a photoinitiator, and a

radiation curable releasing agent (TEGO Chemical Service) for surface activity. The liquid mixture was drop-dispensed onto a silicon master with slanted pillars, which were prepared by an angled etching technique. A PET film with 100 μm thickness was gently placed on the liquid mixture, followed by UV exposure for 40 s (wavelength = 250–400 nm, dose = 100 mJ/cm^2). After UV curing, the mold was peeled off from the master, thereby leaving behind the PUA micromold. Normal PUA for mold and soft PUA for tip have 200 MPa and 20 MPa of elastic modulus, respectively.

2.2. Tip Widening. A feeding roller was used to induce the continuous supply of resin to soft PUA at the end of the fabricated micropillar. A doctor-blade-type resin dispenser was used to coat the soft PUA on the feeding roller and the pressure was applied for coating ($\sim 10 \text{ kPa}$). We also operated the roll device at a relatively slow speed to achieve sufficient inking (10 cm/min). After inking, the liquid resin was spread across the pressure roller and the wide tip was completely formed with additional UV exposure.

2.3. Measurement of Pull-Off Force. We developed the equipment for pull-off force and durability measurements of dry adhesives. The jig with a glass substrate was moved vertically by a motor-driven crank to make contact with a dry adhesive. The dry adhesive was placed on the stage assembled with a z -axis micromanual stage to control the preload, and a micromanual stage that can be tilted was used to adjust the horizontal level. To measure the pull-off force between the dry adhesive and glass substrate, two load cells with a gram-scale resolution and can respond within 100 ms were set below the stage set. The pull-off force was measured with respect to various preloads, and a durability test was conducted at a rate of 50 cycles/min with 40 N preload at room temperature.

2.4. SEM Observation. The fabricated adhesive samples were visually examined by the scanning electron microscopy (SEM) (S-4800, Hitachi), typically at the operating voltage of 10–25 kV after sputtering a thin Au film ($< 5 \text{ nm}$) to avoid electron charging if necessary.

3. Results and Discussion

Figure 1 is a schematic illustration of a continuous production process for dry adhesives consisting of microstructure fabrication and tip inking. Through the whole process, the microstructure was fabricated by UV-assisted molding, the resin to make the adhering part was inked on the tip part of microstructures, and the wide tip was formed by pressurizing with a flat substrate. In the experiment to prove the concept, a 5 cm wide PET film in the roll unit and microstructures mold of 2 cm by 2 cm area were used. In this process, surface treatment of the substrate and the mold is very important. The microstructure was made of PUA and the tip part was made of soft PUA, so that the adhesion

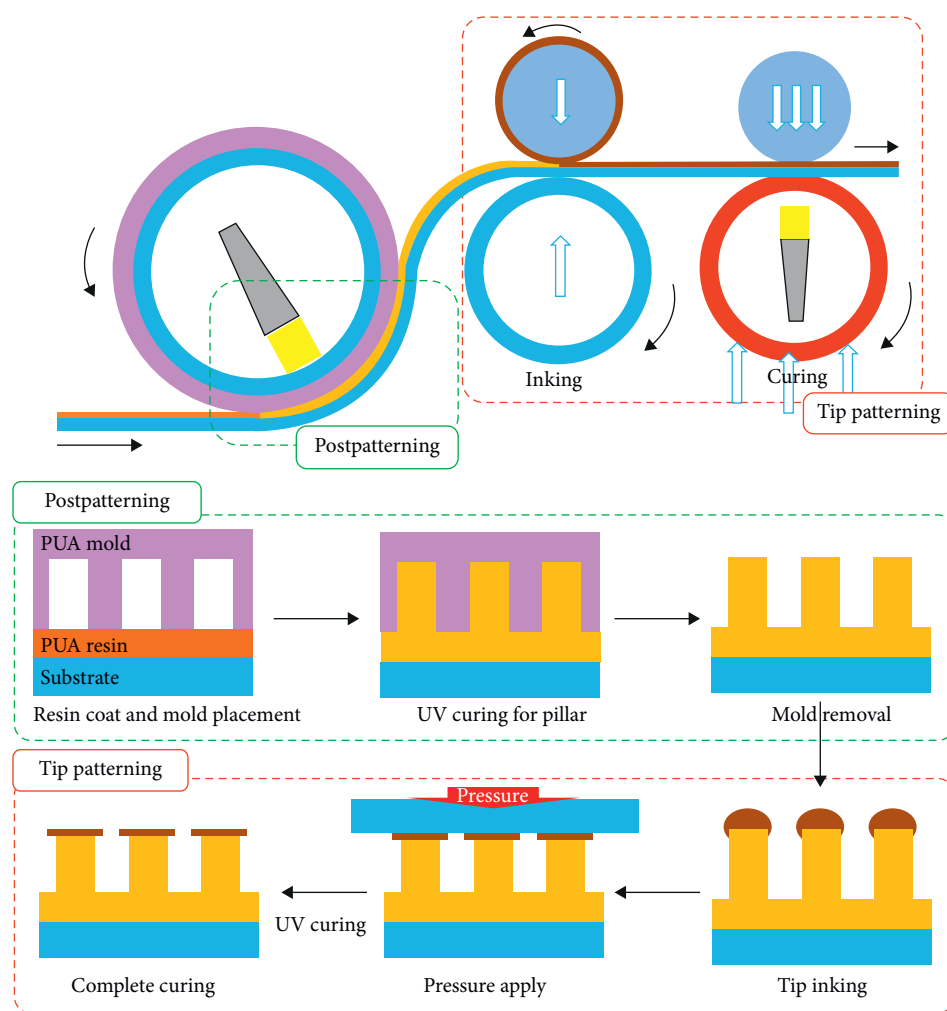


FIGURE 1: Schematic of the continuous fabrication process for mushroom-shaped dry adhesives and procedure for mushroom-shaped structures via imprinting and inking process.

between the two was secured. Because PUA and soft PUA are same kind of polymer-based materials, UV curing has been successfully combined like a single substance. For inking process, a urethane rubber surface was used for proper wetting of the soft PUA, and a PET film with a release treatment was used as the substrate for tip widening. After verifying the possibility of the inking process at the wafer level, the same process principle was applied to achieve continuous production in the roll-to-roll apparatus. The production equipment consists of three process rolls. The first roll is an imprint roll capable of producing a microstructure continuously. We fabricated negative mold of the film type using PUA, and the fabricated soft mold was wound on first roll to realize continuous imprinting. The micropillar structure fabricated on a flexible substrate was then subjected to an inking process through a feeding roll of polymer resin for wide-tip formation. The feeding roll for the inking process was made of urethane and secured with adequate surface energy to transfer the soft PUA to the tip in an appropriate amount. The resin in the tip part is then spread widely by the pressure roll that it contacts. A wide tip was formed on the micropillar by UV exposure with a pressure of about 10 kPa.

The operating speed of the roll unit was determined based on the longest time among the time required for fabricating the microstructure, for inking, and for postexposure. Although not as fast, we were able to produce dry adhesive samples 10 cm long per minute.

Figure 2 shows SEM images of the microstructure of each process of the dry adhesion sample prepared by the aforementioned process. Figure 2(a) is a pillar fabricated by a microstructure production department with a diameter of $10\ \mu\text{m}$, height of $15\ \mu\text{m}$, and period of $35\ \mu\text{m}$. Since the process does not go through an overnight heavy curing process, a reactor still remains on the surface to ensure sufficient wettability and bonding with the soft PUA resin to be inked later. Figures 2(b) and 2(c) are SEM images of the microstructures after inking and tip widening. Due to the sufficient viscosity of the soft PUA, the resin was only present at the tips, and due to the proper wetting it did not flow down the sides of the pillars. In addition, the wide tip was well expressed by the pressure of the PET film roll which was repellent rather than the PUA surface. Although current process conditions have allowed the production of successful dry adhesives, future optimization of the surface energy of the

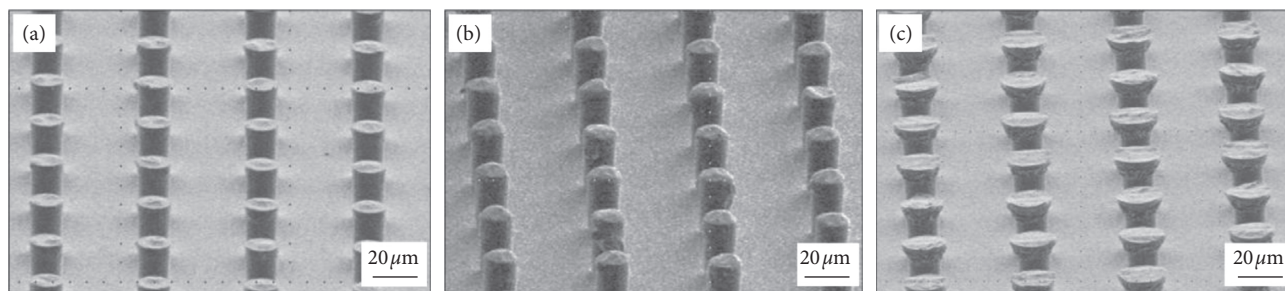


FIGURE 2: SEM images of mushroom structures fabricated in each process: (a) micropillar molding, (b) tip inking, and (c) tip widening.

mold, substrate, and resin will lead to the formation of wider, thinner tips, resulting in high-performance dry adhesives.

Figure 3 shows the measurement results of the pull-off strength, which is a representative performance index of the fabricated dry adhesives. The pull-off strength according to the preload was found to be saturated in the preload of 20 N/cm² or more, and the maximum adhesive property was confirmed as 13 N/cm² in the preload of 40 N/cm². The measured adhesive strength was lower than that of the mushroom-shaped wide-tip microstructures (~20 N/cm²) produced by conventional methods because forming a wide and thin tip necessary for strong adhesion was impossible, which may be solved by optimization of the subsequent process [8].

A comparatively rapid decrease in the adhesive strength was observed during the initial 500 times of use, and the adhesive strength was maintained steadily from about 10 N/cm² to 3000 times of use as shown in Figure 4. After using 1500, 1800, 2100, and 2400 times, cleaning with a Scotch tape was carried out, and the reduced adhesive strength was recovered through this process. Through the cleaning process, the contaminants were removed and the structural collapse, typically pairing, returned to its original state. As the adhesive force recovery through the cleaning process was repeated, the rate at which the adhesive force decreased was gradually increased. Although the adhesion strength is slightly lower than the typical mushroom-shaped microstructure-based dry adhesive, the degradation tendency was considerably better than that of dry adhesives with conventional wide tips. The adhesive strength and lifetime are inversely related to each other; thus, the fabricated dry adhesives are likely to be completely used in applications where they have to be used for a long period of time with a proper adhesive strength. The marathon test result shows a reasonable adhesive strength of up to 3,000 times, and the test is expected to be used in various fields.

4. Conclusions

Demand for dry adhesives has increased in many areas because of their unique performance. However, it was difficult to use because of low yield and long process time of the molding process. In this paper, we have developed a method to continuously fabricate a mushroom-like microstructure by continuously fabricating a simple microstructure using a simple molding process and resin inking. The molded

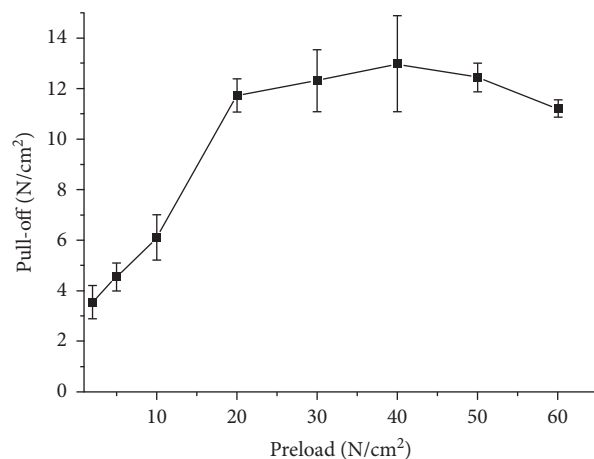


FIGURE 3: Measurement data of the pull-off strength of fabricated dry adhesives as a function of preload.

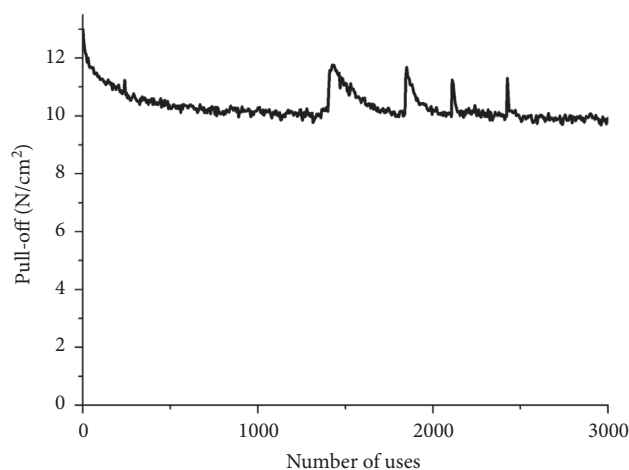


FIGURE 4: Durability test of the fabricated dry adhesives over 3,000 cycles of attachment and detachment.

microstructure acts as a column in the mushroom-like microstructure, and the inked resin acts as a tip through subsequent planarization and curing. The fabricated microstructures showed similar properties to general dry adhesives and showed an adhesion of about 13 N/cm² to the smooth surface. Although the adhesive strength was somewhat lower than that of the conventional dry adhesive production method, the dry adhesive sample produced with

the highly developed technology in terms of productivity did not exhibit a specific adhesive strength drop in 3000 times of use in the marathon test. Further process optimization studies are expected to achieve high adhesive strength when wide tips can be implemented.

Data Availability

The data used to support the findings of this study are available from the corresponding author upon request.

Conflicts of Interest

The authors declare that they have no conflicts of interest.

Acknowledgments

The authors thank Jeong Hyeon Lee for his technical support. MKK acknowledges the support by a grant from the National Research Foundation of Korea (2016R1A2B4007858) funded by the Korean government (MSIP). CWP acknowledges the support by a grant from the National Research Foundation of Korea (2017R1A2B2005515) funded by the Korean government (MSIP).

References

- [1] K. Autumn, "The gecko effect: dynamic dry adhesive microstructures," *American Zoologist*, vol. 41, no. 6, pp. 1382–1383, 2001.
- [2] S. N. Gorb and M. Varenberg, "Mushroom-shaped geometry of contact elements in biological adhesive systems," *Journal of Adhesion Science and Technology*, vol. 21, no. 12–13, pp. 1175–1183, 2007.
- [3] I. Hwang, H. N. Kim, M. Seong et al., "Multifunctional smart skin adhesive patches for advanced health care," *Advanced Healthcare Materials*, vol. 7, no. 15, article 1800275, 2018.
- [4] M. K. Kwak, H.-E. Jeong, and K. Y. Suh, "Rational design and enhanced biocompatibility of a dry adhesive medical skin patch," *Advanced Materials*, vol. 23, no. 34, pp. 3949–3953, 2011.
- [5] S. H. Lee, S. W. Kim, B. S. Kang, P.-S. Chang, and M. K. Kwak, "Scalable and continuous fabrication of bio-inspired dry adhesives with a thermosetting polymer," *Soft Matter*, vol. 14, no. 14, pp. 2586–2593, 2018.
- [6] M. Varenberg, N. M. Pugno, and S. N. Gorb, "Spatulate structures in biological fibrillar adhesion," *Soft Matter*, vol. 6, no. 14, pp. 3269–3272, 2010.
- [7] H. Yi, I. Hwang, J. H. Lee et al., "Continuous and scalable fabrication of bioinspired dry adhesives via a roll-to-roll process with modulated ultraviolet-curable resin," *ACS Applied Materials & Interfaces*, vol. 6, no. 16, pp. 14590–14599, 2014.
- [8] H. Yi, M. Kang, M. K. Kwak, and H. E. Jeong, "Simple and reliable fabrication of bioinspired mushroom-shaped micropillars with precisely controlled tip geometries," *ACS Applied Materials & Interfaces*, vol. 8, no. 34, pp. 22671–22678, 2016.
- [9] H. E. Jeong, J.-K. Lee, H. N. Kim, S. H. Moon, and K. Y. Suh, "A nontransferring dry adhesive with hierarchical polymer nanohairs," *Proceedings of the National Academy of Sciences*, vol. 106, no. 14, pp. 5639–5644, 2009.
- [10] L. F. Boesel, C. Greiner, E. Arzt, and A. del Campo, "Gecko-inspired surfaces: a path to strong and reversible dry adhesives," *Advanced Materials*, vol. 22, no. 19, pp. 2125–2137, 2010.
- [11] A. del Campo, C. Greiner, I. Alvarez, and E. Arzt, "Patterned surfaces with pillars with controlled 3D tip geometry mimicking bioattachment devices," *Advanced Materials*, vol. 19, no. 15, pp. 1973–1977, 2007.
- [12] C. Greiner, E. Arzt, and A. del Campo, "Hierarchical gecko-like adhesives," *Advanced Materials*, vol. 21, no. 4, pp. 479–482, 2009.
- [13] M. K. Kwak, C. Pang, H.-E. Jeong et al., "Towards the next level of bioinspired dry adhesives: new designs and applications," *Advanced Functional Materials*, vol. 21, no. 19, pp. 3606–3616, 2011.
- [14] S. Seok, B. Lee, J. Kim, H. Kim, and K. Chun, "A new compensation method for the footing effect in MEMS fabrication," *Journal of Micromechanics and Microengineering*, vol. 15, no. 10, pp. 1791–1796, 2005.
- [15] D. Sameoto and C. Menon, "A low-cost, high-yield fabrication method for producing optimized biomimetic dry adhesives," *Journal of Micromechanics and Microengineering*, vol. 19, no. 11, 2009.
- [16] S. Lee, H. Yi, C. Park, H. Jeong, and M. Kwak, "Continuous tip widening technique for roll-to-roll fabrication of dry adhesives," *Coatings*, vol. 8, no. 10, p. 349, 2018.

Research Article

Influence of Oxidants on the Stability of Tocopherol in Model Nanoemulsions: Role of Interfacial Membrane Organized by Nonionic Emulsifiers

Jinhyuk Kim,¹ Ha Youn Song,² and Seung Jun Choi ^{1,3}

¹Department of Food Science and Technology, Seoul National University of Science and Technology, Seoul 01811, Republic of Korea

²Department of Agricultural Biotechnology, Seoul National University, Seoul 08826, Republic of Korea

³Department of Interdisciplinary Bio IT Materials, Seoul National University of Science and Technology, Seoul 01811, Republic of Korea

Correspondence should be addressed to Seung Jun Choi; choisj@seoultech.ac.kr

Received 17 August 2018; Accepted 16 October 2018; Published 12 November 2018

Guest Editor: Hiroshi Umakoshi

Copyright © 2018 Jinhyuk Kim et al. This is an open access article distributed under the Creative Commons Attribution License, which permits unrestricted use, distribution, and reproduction in any medium, provided the original work is properly cited.

Nanoemulsions were prepared by using emulsifiers with various sizes of hydrophilic and hydrophobic groups to determine the impact of interfacial characteristics on the stability of α -tocopherol incorporated into the nanoemulsions. The α -tocopherol concentration remaining after 3 weeks of storage at 25°C depended greatly on the type of oxidative stress, which indicated that the environment surrounding the oil droplets could determine the stability of α -tocopherol in nanoemulsions. α -Tocopherol was gradually degraded by radical-mediated oxidation over storage, and approximately 60% of its initial concentration remained after 3 weeks of storage. However, under acid- and iron-mediated oxidation, α -tocopherol concentration steeply decreases for the initial 3-day storage, but the degradation rate of α -tocopherol decreased after 3 days of storage and over 90% of the initial α -tocopherol remained after 3 weeks of storage. Interestingly, and contrary to our expectations, the thickness and/or density of the droplet interfacial membrane rarely affected the stability of α -tocopherol incorporated into nanoemulsions. Although it is difficult to generalize beyond α -tocopherol, we conclude that the properties of oil droplet surfaces had no influence on the storage stability of α -tocopherol encapsulated in the droplets.

1. Introduction

Lipid oxidation is one of the greatest concerns for oil-containing food products because of its negative influence on nutritional quality and consumer health [1]. In addition to lipid oxidation, lipophilic functional compounds incorporated into emulsion-based delivery systems can be decomposed by various oxidative stresses [2]. To inhibit lipid oxidation and to prevent lipophilic compound decomposition, several synthetic and natural antioxidants are generally incorporated into foods containing considerable amounts of lipids [3]. However, as a result of consumers' demands for clean food (i.e., food products that do not contain synthetic additives), food manufacturers have been making various attempts to replace synthetic antioxidants

with natural ones. Among the natural antioxidants permitted for food use, tocopherols are important because they exist naturally in many vegetable oils [4] and because they have the ability to retard lipid oxidation by reacting with several radicals generated from lipid molecules, thereby protecting functional compounds from oxidative degradation. α -Tocopherol radicals can form nonradical products if they are reduced by other coexisting antioxidants, with regeneration of α -tocopherol.

In food systems, oil-in-water emulsions generally consist of water and oil, with the oil being dispersed as small droplets in the water [5]. Emulsifiers have surface activity, so they can create kinetically stable emulsions by absorbing at the surfaces of droplets newly formed during homogenization [6]. Emulsifiers adsorbed at the oil droplet surfaces

create an interfacial membrane comprised of a layer formed of their hydrophobic tails and a layer formed of their hydrophilic heads. Physical destabilization processes, such as coalescence, flocculation, and Ostwald ripening, are greatly affected by the characteristics of interfacial membranes formed with emulsifiers [7]. Interfacial membranes also alter the rates of chemical reactions, such as lipid oxidation [8–10], between oil- and aqueous-phase compounds. Additionally, when a functional lipophilic compound is incorporated into emulsion droplets, the interfacial properties of the oil droplet surface are the main factors that control the stability of the functional compound incorporated therein [3, 11]. Because the interfacial membrane is formed with emulsifiers, the structural and physicochemical properties of emulsifiers play important roles in the emulsion stability and in the storage stability of functional compounds incorporated into the oil droplets [12].

Oil-in-water (O/W) emulsions are widely used as delivery systems in a variety of industries because of their abilities to encapsulate functional lipophilic compounds. Generally, O/W emulsions are classified into conventional emulsions (usually called “emulsions”) and nanoemulsions, according to the size of the emulsion droplets [13]. Because nanoemulsions have much larger specific surface areas than conventional emulsions, chemical degradation reactions at the oil-water interface can occur more quickly in nanoemulsions than in conventional emulsions [14]. Therefore, when O/W nanoemulsions are used as nanocarriers in delivery systems, the interfacial membrane formed by the emulsifier is an important factor in controlling the ability of the emulsion to protect the encapsulated functional compounds and to inhibit their diffusion from the oil droplets into the aqueous phase.

Therefore, in nanoemulsion-based oral delivery systems for functional lipophilic compounds, it is important to know how the interfacial membrane affects the stability of α -tocopherol incorporated into the emulsion for the prevention of lipid oxidation and to understand the effectiveness of α -tocopherol in inhibiting the degradation of the functional lipophilic compounds by oxidative stress from the aqueous phase. Over the past decades, scientists have investigated how the stability and effectiveness of emulsion systems are altered during the incorporation of α -tocopherol [15, 16]. The charge of the emulsion droplet surfaces is one of the major factors influencing the oxidative stability of the emulsified oil and also the stability of the α -tocopherol. The chemical stability of α -tocopherol is effectively improved in emulsions droplets with positively charged surfaces. When α -tocopherol is incorporated into an emulsion with negatively charged interfaces, the α -tocopherol stability can be increased by adding a biopolymer layer with a positive charge to the negatively charged droplet surfaces. However, despite this, most studies on the influence of interfacial membrane properties have shown that the charge of the emulsion droplet surfaces is a key factor influencing the stability of α -tocopherol in emulsions and in lipid oxidation. Therefore, the objective of this work was to determine whether the structural properties of the interfacial membrane could be involved in α -tocopherol decomposition in

emulsions, particularly emulsion-based delivery systems. This evaluation was accomplished by using model emulsion-based delivery systems stabilized by emulsifiers with different hydrophilic head sizes, which led to various droplet interfacial thicknesses.

2. Materials and Methods

2.1. Materials. Polyoxyethylene alkyl ether-type emulsifiers (polyoxyethylene 10 lauryl ether (P10L), polyoxyethylene 10 stearyl ether (P10S), polyoxyethylene 20 stearyl ether (P20S), and polyoxyethylene 23 lauryl ether (P23L), and polyoxyethylene 100 stearyl ether (P100S)) were purchased from Sigma-Aldrich (St. Louis, MO, USA). The molecular structures of the polyoxyethylene alkyl ether-type emulsifiers used in this study are presented in Figure 1. α -Tocopherol, 2,2'-azobis(2-methylpropionamide) dihydrochloride (AAPH), ferrous sulfate heptahydrate ($\text{FeSO}_4 \cdot 7\text{H}_2\text{O}$), and ferric chloride hexahydrate ($\text{FeCl}_3 \cdot 6\text{H}_2\text{O}$) were also purchased from Sigma-Aldrich. Medium-chain triglyceride (Delios S) comprised caprylic (70%) and 30% capric (30%) acids and were obtained from BASF (Ludwigshafen, Germany). All other chemicals used were of analytical grade.

2.2. Emulsion Preparation. The aqueous phase was prepared by dissolving the emulsifiers in the phosphate buffer (10 mM and pH 7) to a predetermined concentration, and the oil phase was prepared by dissolving α -tocopherol in medium-chain triglycerides at a final concentration of 5 mmol/kg. Coarse emulsions were prepared by homogenizing the oil (5%, w/w) and aqueous (95%, w/w) phases (0.25 mmol α -tocopherol/kg emulsion) in a high-speed blender (T18 Basic Ultra-Turrax, Ika, Staufen, Germany) for 2 min at room temperature. The oil droplet sizes in the coarse emulsions were then reduced with 5 passes through a microfluidizer (MN400BF, Micronox, Seongnam, Korea) at 100 MPa. After adjustment of the pH level of the emulsions to a predetermined value, the emulsions were purged with nitrogen with gentle stirring for 30 min before the subsequent step. To determine the effect of transition metals on α -tocopherol stability in the emulsions, ferrous sulfate or ferric chloride solution was added to the emulsions at a final concentration of 1 mmol/kg emulsion. Furthermore, to evaluate the effect of free radicals on α -tocopherol stability in the emulsions, AAPH solution was added to the emulsions to a final concentration of 1 mmol/kg emulsion. Then, 10 g of the emulsion sample were transferred into 12 mL of a glass vial, closed airtight, and were stored in the dark at 25°C.

2.3. Droplet Size Measurement. The mean emulsion droplet diameters were measured by using static light scattering (laser diffraction). To avoid multiple scattering effects, all emulsion samples were diluted to a droplet concentration of approximately 0.005% (w/w) with a buffer solution of the same pH value as the sample, and samples were stirred continuously throughout the measurements to ensure homogeneity. The refractive index values for MCT and buffer solution were set at 1.47 and 1.33, respectively. The particle

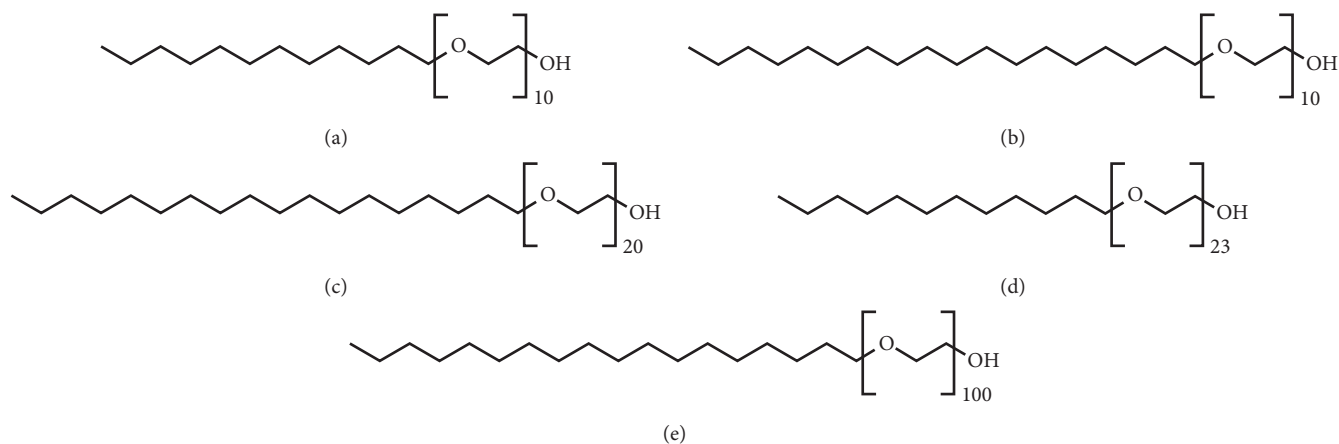


FIGURE 1: Molecular structures of polyoxyethylene alkyl ether-type emulsifiers used in this work. (a) polyoxyethylene 10 lauryl ether (P10L); (b) polyoxyethylene 10 stearyl ether (P10S); (c) polyoxyethylene 20 stearyl ether (P20S); (d) polyoxyethylene 23 lauryl ether (P23L); (e) polyoxyethylene 100 stearyl ether (P100S).

size distribution of the emulsions was then measured by using a commercial static light scattering instrument (BT-9300ST; Bettersize Instruments, Dandong, China). The particle size data are reported as the volume-weighted mean diameter, $d_{43} = \sum n_i \cdot d_i^4 / \sum n_i \cdot d_i^3$, with n_i representing the number of particles with diameter d_i .

2.4. α -Tocopherol Concentration Measurement. α -Tocopherol concentration was measured according to the method described by Yang et al. [17] with slight modification. α -Tocopherol concentrations in emulsions were determined by first vigorously vortexing 2 g of emulsion with 4 g of dichloromethane for 2 min. The mixture was then centrifuged at $1,842 \times g$ for 10 min at 25°C , and the solvent layer was collected. α -Tocopherol concentrations were determined with HPLC by using an Agilent 1100 instrument (Palo Alto, CA, USA). A Triart C18 column (250 mm \times 4.6 mm \times 5 μm , YMC, Tokyo, Japan) was used, with a methanol mobile phase at a rate of 1 mL/min. The wavelength for detection was 295 nm. Concentrations of α -tocopherol were calculated on the basis of a calibration curve generated by using authentic α -tocopherol.

Therefore, the decomposition rate (k) of α -tocopherol was calculated, by assuming a first-order reaction:

$$C_t = C_0 \cdot e^{-k \cdot t}, \quad (1)$$

where C_0 is the initial α -tocopherol concentration (mmol/kg emulsion) and C_t is the α -tocopherol concentration remaining at time t (day). The k value was calculated by performing a linear regression on the plot $\ln(C_t/C_0)$ versus t . The equality of coefficients of different linear regressions was analyzed by the Chow test [18]. If time-dependent changes in the degradation of α -tocopherol in emulsions were observed (the fast degradation of α -tocopherol in the early stage of storage and the slow its degradation in the late storage period in this study), the initial α -tocopherol decomposition rate (mmol/kg emulsion/day) was determined. The initial α -tocopherol decomposition rate could be determined by calculating the

tangential slope at $t = 0$ because the instantaneous rate at time t is determined by calculating the tangential slope at t on α -tocopherol concentration versus time curve.

2.5. Statistical Analysis. All the experiments were performed in triplicate, and the data are expressed as mean \pm standard deviation. Analysis of variance (ANOVA) was performed, and the mean separations were performed using Duncan's multiple range test ($p < 0.05$). The statistical analyses described above were all conducted using SAS (version 9.4.; SAS Institute Inc., Cary, NC, USA).

3. Results and Discussion

To minimize the negative effect of micelles on the stability of the emulsions and α -tocopherol therein [19], the minimum emulsifier concentrations (MECs) required to prepare highly stable emulsions with mostly small droplets were determined in our previous study [7]. The MECs for P10L, P10S, P20S, P23L, and P100S were 2.903, 3.165, 2.926, 1.784, and 0.994 mM, respectively. As all emulsions prepared at the MECs had similar initial droplet diameters ($d_{43} = 0.29, 0.28, 0.29, 0.32,$ and $0.28 \mu\text{m}$ for P10L-, P10S-, P20S-, P23L-, and P100S-stabilized emulsions, respectively) and the droplet sizes rarely changed after 21 days of storage, and any significant difference in the α -tocopherol decomposition rate between emulsions could not stem from an effect of the oil droplet interfacial area. Although the emulsifier concentration in emulsions were different from each emulsion, the facts that all emulsions had a similar oil droplet size indicated that emulsions had the different emulsifier loading (emulsifier concentration per unit droplet surface area) values which could be attributed to droplet interfacial density. The emulsifier loading values for P10L-, P10S-, P20S-, P23L-, and P100S-stabilized emulsions were calculated as 1.91, 2.90, 1.87, 1.24, and $0.62 \mu\text{mol}/\text{m}^2$, respectively, indicating that the interfacial density of emulsions differed. When oils are stabilized by emulsifiers to spherical droplets, the interfacial membrane of oil droplet surfaces are

comprised of the inner layer formed with the hydrophobic tails of emulsifiers and the outer layer formed with their hydrophilic heads. Considering the molecular structures of emulsifiers used in this work, it means that the thickness of the outer layer of the interfacial membrane could be mainly attributed by a number of oxyethylene groups of the hydrophilic groups of emulsifiers and that the length of alkyl chains of the hydrophobic tails of emulsifiers could determine the thickness of its inner layer.

Since the partition coefficient of α -tocopherol is approximately 12 [20], it is likely that the concentration of α -tocopherol in the aqueous phase was negligible. Therefore, if α -tocopherol degradation is observed after a certain period of storage and prooxidants are present in the aqueous phase, most of α -tocopherol must have decomposed at the emulsion droplet surface, rather than in the aqueous phase.

3.1. Influence of the pH Level on α -Tocopherol Degradation.

Vitamin E compounds, including α -tocopherol, exhibit fairly good stability in the absence of oxygen and lipid peroxides [21]. However, with the consideration that commercially available emulsion-based foods are generally acidic [10] and molecular oxygen is never completely removed from them, it is important to understand the influence of the pH level on the chemical stability of α -tocopherol in emulsions. Therefore, to examine how the characteristics of emulsion droplet surfaces affect the chemical decomposition of α -tocopherol in acidic environments, the pH level of the emulsions was adjusted to 7 or 3 and the emulsions were then stored. Because medium-chain triglycerides consist of only saturated fatty acids, they are exceptionally stable to oxidation [22]. In addition, most of the oxygen molecules were removed by nitrogen purging. Therefore, if α -tocopherol degradation is observed to a considerable level, it could be the result of factors other than lipid peroxides derived from the oxidation of the medium-chain triglyceride carrier oil. One possible reason for the reduction of α -tocopherol during storage is the presence of a trace amount of oxygen molecules in the emulsions. In this study, to minimize the effect of oxygen molecules on α -tocopherol decomposition, nitrogen purging was carried out to remove oxygen molecules. However, it seems that the oxygen molecules in the aqueous phase were not completely removed. The effects of the emulsifier and pH level on α -tocopherol stability in emulsions are shown in Figure 2. As indicated in Table 1, regardless of the pH level, P100S-stabilized emulsions showed the highest initial decomposition rate of α -tocopherol among the emulsions. P100S has the largest hydrophilic head size among the emulsifiers used and the P100S-stabilized emulsion contained the smallest amount of the emulsifier among the emulsions prepared in this work, so it appears that the thick and/or loosely-packed interface is disadvantageous for the stability of α -tocopherol encapsulated in the emulsions. Because the P10S- and P20S-stabilized emulsions have droplet surfaces of similar density, it was expected that α -tocopherol in the emulsion stabilized with P20S, which has a hydrophilic head size that is twice as large as that of

P10S, would be more stable than that in the P10S-stabilized emulsion; however, there was no significant difference in the initial decomposition rate of α -tocopherol in these two emulsions ($p > 0.05$). P20S- and P23L-stabilized emulsions have interfacial membranes of similar thickness because the difference in the oxyethylene group number of the hydrophilic heads of P20S and P23L is only three, while the P20S-stabilized emulsion has a denser interfacial membrane than the P23L-stabilized emulsion, as described above. However, both of these emulsions showed very similar initial decomposition rates of α -tocopherol, independent of the pH level. It was apparent that the thickness and/or density of the droplet surfaces did not affect the initial α -tocopherol decomposition rate. In addition, considering the content (>90%) of α -tocopherol remaining after 21 days of storage, the variation in initial α -tocopherol decomposition rates among the emulsions did not have much effect.

3.2. Influence of Transition Metals on α -Tocopherol Degradation.

The previous findings indicate that iron ions could be the direct or indirect reasons for the degradation of the several food components including lipids [23] and the precursors of vitamins such as carotenoids [24] because of their electron transfer reaction. The cation radicals could be formed by the interaction of iron ions with those food components. It means transition metals like iron could act as oxidizing agents. Therefore, in this study, iron ions were chosen as oxidants for studying the degradation of α -tocopherol. The initial decomposition rates of α -tocopherol in emulsions with iron were different from those of α -tocopherol in iron-free emulsions. As shown in Table 1, the emulsions stabilized with different emulsifiers in the absence of iron had different initial α -tocopherol decomposition rates, whereas little difference was observed in the initial α -tocopherol decomposition rates for emulsions stabilized with different emulsifiers in the presence of iron. However, similar to the observation mentioned above, there was no significant difference in the α -tocopherol content remaining in the emulsions after 21 days of storage ($p < 0.05$), which suggests that iron did not have an influence on the stability of α -tocopherol in the emulsions (Figures 3 and 4).

Irrespective of the oxidative state of the iron, the initial decomposition rates of α -tocopherol in emulsions in the presence of ferrous iron were not significantly different from those in emulsions stored with ferric iron ($p < 0.05$). In addition, when emulsions contained iron with the same oxidative state, they showed very similar initial decomposition rates of α -tocopherol, regardless of the pH level. Although all of the emulsifiers used in this work were nonionic, the droplet surface charges of the emulsions were slightly negative and their values changed depending on the pH level (-7.3, -6.8, -5.5, -9.4, and -1.7 mV for P10L-, P10S-, P20S-, P23L-, and P100S-stabilized emulsions at pH 7, respectively, and around -1.5 mV at pH 3). Because the droplet surfaces were more negatively charged at pH 7, except those in the P100S-stabilized emulsion and could attract iron molecules to the surface of the emulsion droplets, it was expected that α -tocopherol would be rapidly decomposed at pH 7 because the

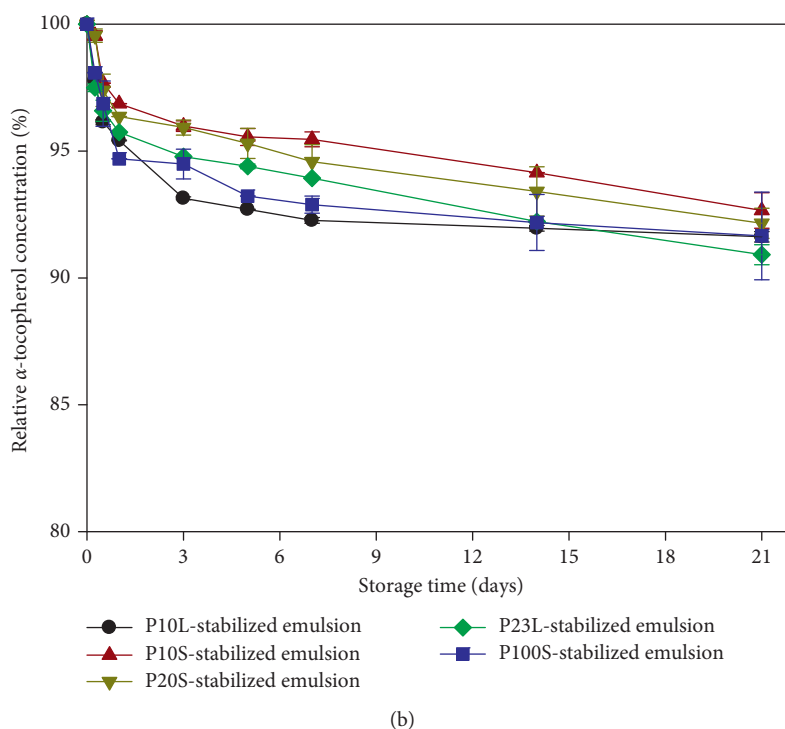
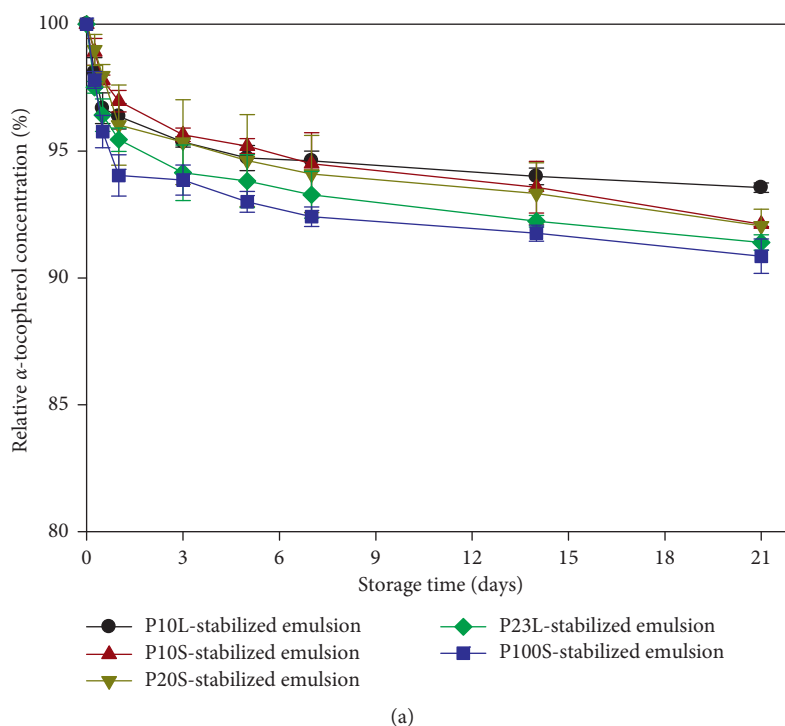


FIGURE 2: Change in concentration of α -tocopherol in emulsions at pH 7 (a) and 3 (b) stored at 25°C. P10L, polyoxyethylene 10 lauryl ether; P10S, polyoxyethylene 10 stearyl ether; P20S, polyoxyethylene 20 stearyl ether; P23L, polyoxyethylene 23 lauryl ether; P100S, polyoxyethylene 100 stearyl ether.

iron molecules would accumulate around the more negatively charged droplet surfaces at this pH level. This suggests that the iron did not decompose α -tocopherol by direct interaction at the interfacial membrane. Therefore, the stability of α -tocopherol in emulsions was not influenced by the thickness and/or density of the droplet interfaces.

3.3. Influence of Radicals on α -Tocopherol Degradation. AAPH may be a suitable material for studying the influence of radicals on the stability of α -tocopherol encapsulated in emulsions because it is a self-generator of free radicals through spontaneous decomposition at room temperature. Quite different from the previous findings, in this case, the

TABLE 1: The initial decomposition rate (mmol/kg emulsion/day) of α -tocopherol in emulsions stabilized with emulsifiers having various sizes of hydrophilic and hydrophobic groups.

Environmental stress		Emulsifier used for emulsion preparation				
		P10L	P10S	P20S	P23L	P100S
pH 7	No	^{AB} 0.0185 ± 0.0108 ^{ab}	^B 0.0034 ± 0.0007 ^b	^B 0.0083 ± 0.0094 ^b	^A 0.0098 ± 0.0109 ^{ab}	^A 0.0266 ± 0.0095 ^a
	Ferrous iron	^{ABC} 0.0142 ± 0.0003 ^c	^{AB} 0.0210 ± 0.0000 ^b	^A 0.0250 ± 0.0009 ^a	^A 0.0242 ± 0.0028 ^a	^A 0.0211 ± 0.0002 ^b
	Ferric iron	^A 0.0210 ± 0.0093 ^a	^{AB} 0.0231 ± 0.0028 ^a	^A 0.0215 ± 0.0035 ^a	^A 0.0258 ± 0.0323 ^a	^A 0.0230 ± 0.0061 ^a
pH 3	No	^{ABC} 0.0173 ± 0.0004 ^b	^B 0.0030 ± 0.0000 ^c	^B 0.0034 ± 0.0005 ^c	^A 0.0030 ± 0.0005 ^c	^A 0.0188 ± 0.0011 ^a
	Ferrous iron	^A 0.0226 ± 0.0017 ^a	^{AB} 0.0225 ± 0.0021 ^a	^A 0.0250 ± 0.0009 ^a	^A 0.0217 ± 0.0042 ^a	^A 0.0107 ± 0.0011 ^b
	Ferric iron	^A 0.0231 ± 0.0006 ^a	^A 0.0330 ± 0.0407 ^a	^A 0.0264 ± 0.0101 ^a	^A 0.0364 ± 0.0467 ^a	^A 0.0198 ± 0.0236 ^a

P10L, polyoxyethylene 10 lauryl ether; P10S, polyoxyethylene 10 stearyl ether; P20S, polyoxyethylene 20 stearyl ether; P23L, polyoxyethylene 23 lauryl ether; P100S, polyoxyethylene 100 stearyl ether. The values with different small letter superscripts in the same row are significantly different ($p < 0.05$) by Duncan's multiple range test. The values with different capital letter superscripts in the same column are significantly different ($p < 0.05$) by Duncan's multiple range test.

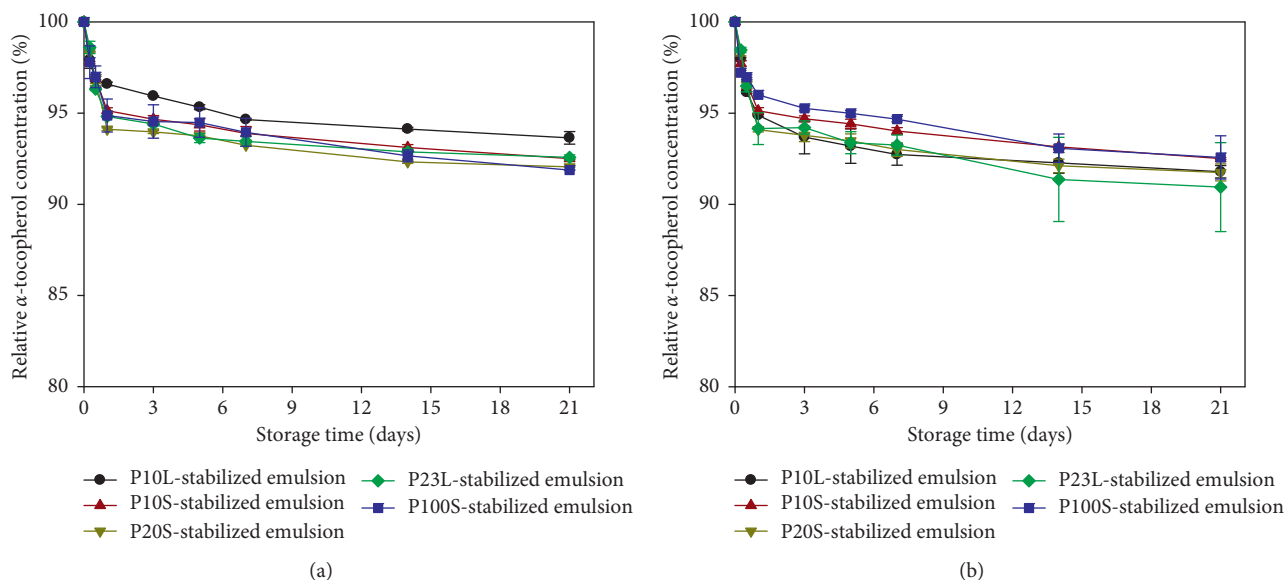


FIGURE 3: Change in concentration of α -tocopherol in emulsions in the presence of ferrous iron at pH 7 (a) and 3 (b) stored at 25°C. P10L, polyoxyethylene 10 lauryl ether; P10S, polyoxyethylene 10 stearyl ether; P20S, polyoxyethylene 20 stearyl ether; P23L, polyoxyethylene 23 lauryl ether; P100S, polyoxyethylene 100 stearyl ether.

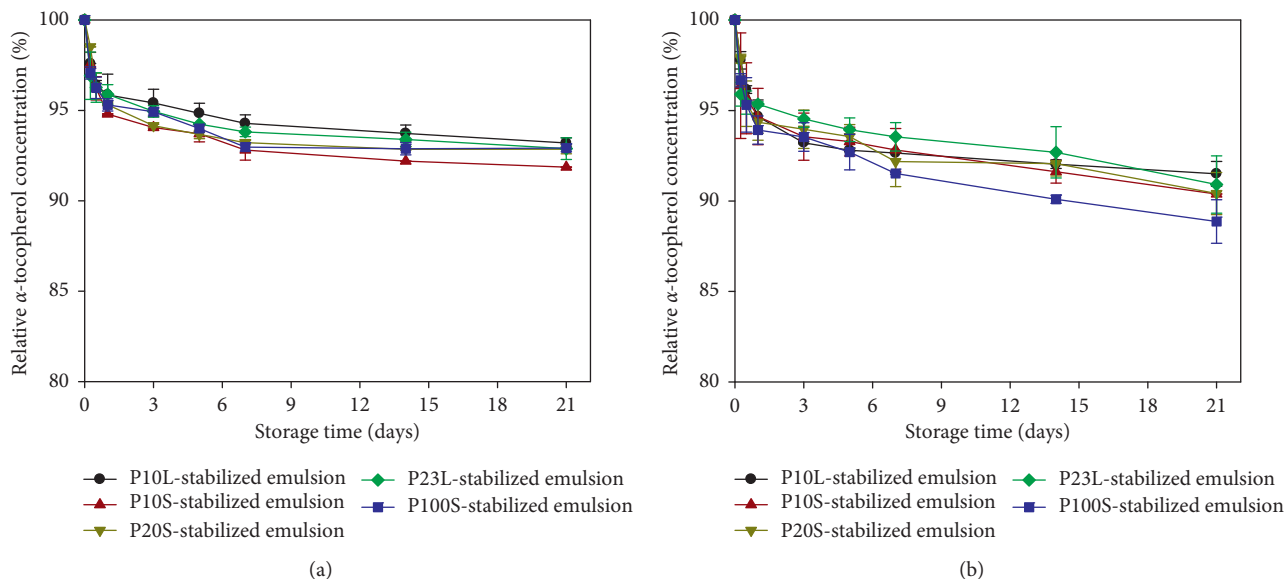


FIGURE 4: Change in concentration of α -tocopherol in emulsions in the presence of ferric iron at pH 7 (a) and 3 (b) stored at 25°C. P10L, polyoxyethylene 10 lauryl ether; P10S, polyoxyethylene 10 stearyl ether; P20S, polyoxyethylene 20 stearyl ether; P23L, polyoxyethylene 23 lauryl ether; P100S, polyoxyethylene 100 stearyl ether.

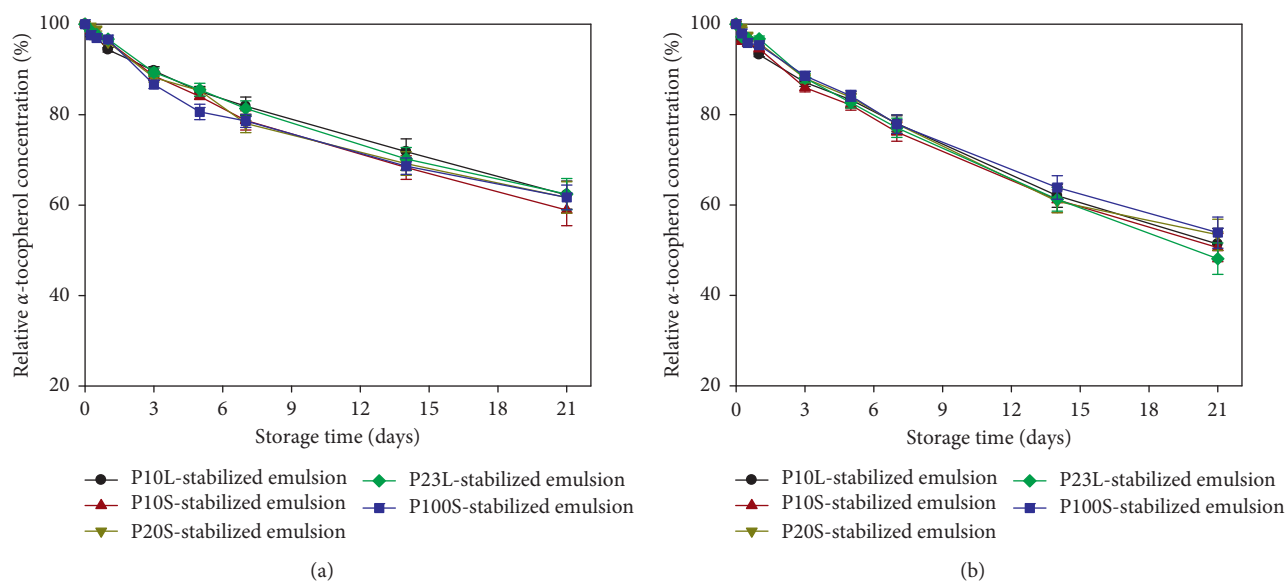


FIGURE 5: Change in concentration of α -tocopherol in emulsions in the presence of radicals at pH 7 (a) and 3 (b) stored at 25°C. P10L, polyoxyethylene 10 lauryl ether; P10S, polyoxyethylene 10 stearyl ether; P20S, polyoxyethylene 20 stearyl ether; P23L, polyoxyethylene 23 lauryl ether; P100S, polyoxyethylene 100 stearyl ether.

TABLE 2: The decomposition rate (k) of α -tocopherol in emulsions stabilized with emulsifiers having various sizes of hydrophilic and hydrophobic groups in presence of radicals.

	Emulsifier used for emulsion preparation									
	P10L		P10S		P20S		P23L		P100S	
	k (day^{-1})	r^2	k (day^{-1})	r^2	k (day^{-1})	r^2	k (day^{-1})	r^2	k (day^{-1})	r^2
pH 7	^B 0.0218 ^b	0.989	^B 0.0252 ^a	0.984	^B 0.0235 ^{ab}	0.967	^B 0.0226 ^{ab}	0.985	^B 0.0230 ^{ab}	0.951
pH 3	^A 0.0312 ^{bc}	0.996	^A 0.0319 ^b	0.994	^A 0.0310 ^{bc}	0.988	^A 0.0344 ^a	0.999	^A 0.0293 ^c	0.995

P10L, polyoxyethylene 10 lauryl ether; P10S, polyoxyethylene 10 stearyl ether; P20S, polyoxyethylene 20 stearyl ether; P23L, polyoxyethylene 23 lauryl ether; P100S, polyoxyethylene 100 stearyl ether. The α -tocopherol decomposition rate values with different small letter superscripts in the same row are significantly different ($p < 0.05$) by the Chow test. The α -tocopherol decomposition rate values with different capital letter superscripts in the same column are significantly different ($p < 0.05$) by the Chow test.

α -tocopherol concentration gradually decreased during the 21-day storage period (Figure 5). The values of k for α -tocopherol in emulsions stored at pH 3 ranged from 0.0293 to 0.0344 day^{-1} , and the values of k for α -tocopherol in emulsions stored at pH 7 ranged from 0.0218 to 0.0252 day^{-1} (Table 2). Although α -tocopherol decomposed more quickly in acidic conditions than neutral conditions, the lack of correlation between the k value and the properties (thickness and/or density) of the interfacial membranes suggests that the interfacial characteristics played little or no role in improving the stability of emulsified α -tocopherol against radical-mediated oxidation.

During the design of this experiment, we expected that the properties of the interfacial membranes of oil droplets would affect the storage stability of α -tocopherol incorporated in emulsions. Although there is a lack of information about the influence of the density of interfacial membranes on the oxidative stability of emulsified oils and the storage stability of encapsulated functional lipophilic compounds, according to previous studies, the emulsion interfacial thickness could be one of the important

determinants of the oxidative stability of food emulsions [16]. Song et al. [11] reported that the storage stability of β -carotene in emulsions varied depending on the droplet interfacial thickness, and they also revealed that the droplet interfacial density may be a factor to consider for improving β -carotene stability. As described above, all of the emulsions analyzed in this study had different densities and thicknesses for their interfacial membranes. For example, the P100S-stabilized emulsion had the thickest interfacial membrane but its density was the lowest among the emulsions, whereas the P10L- and P10S-stabilized emulsions had the opposite properties. The stability of α -tocopherol in the emulsions greatly depended on the environmental conditions surrounding the emulsion droplets, and the denseness and/or thickness of the interfacial membrane of the oil droplets did not play a crucial role in improving the stability of the encapsulated α -tocopherol. In conclusion, our findings, together with those of previous studies, suggested that the data are still insufficient to generalize the influence of droplet interface characteristics on the oxidative stability of emulsified oils

and the chemical stability of encapsulated oil-soluble components.

Data Availability

The data used to support the findings of this study are available from the corresponding author upon request.

Conflicts of Interest

The authors declare that they have no conflicts of interest.

Acknowledgments

This study was supported by the Research Program funded by Seoul National University of Science and Technology.

References

- [1] E. N. Frankel, "Lipid oxidation: mechanisms, products and biological significance," *Journal of the American Oil Chemists' Society*, vol. 61, no. 12, pp. 1908–1917, 1984.
- [2] D. J. McClements, E. A. Decker, and J. Weiss, "Emulsion-based delivery systems for lipophilic bioactive components," *Journal of Food Science*, vol. 72, no. 8, pp. R109–R124, 2007.
- [3] D. J. McClements, "Emulsion design to improve the delivery of functional lipophilic components," *Annual Review of Food Science and Technology*, vol. 1, no. 1, pp. 241–269, 2010.
- [4] E. N. Frankel, "Antioxidants in lipid foods and their impact on food quality," *Food Chemistry*, vol. 57, no. 1, pp. 51–55, 1996.
- [5] D. J. McClements, *Food Emulsions: Principles, Practices, and Techniques*, CRC Press, Boca Raton, FL, USA, 2nd edition, 2005.
- [6] H. D. Silva, M. A. Cerqueira, B. W. S. Souza et al., "Nano-emulsions of β -carotene using a high-energy emulsification-evaporation technique," *Journal of Food Engineering*, vol. 102, no. 2, pp. 130–135, 2011.
- [7] S. W. Han, H. Y. Song, T. W. Moon, and S. J. Choi, "Influence of emulsion interfacial membrane characteristics on Ostwald ripening in a model emulsion," *Food Chemistry*, vol. 242, pp. 91–97, 2018.
- [8] B. Chen, D. J. McClements, and E. A. Decker, "Role of continuous phase anionic polysaccharides on the oxidative stability of Menhaden oil-in-water emulsions," *Journal of Agricultural and Food Chemistry*, vol. 58, no. 6, pp. 3779–3784, 2010.
- [9] H. Faraji, D. J. McClements, and E. A. Decker, "Role of continuous phase protein on the oxidative stability of fish oil-in-water emulsions," *Journal of Agricultural and Food Chemistry*, vol. 52, no. 14, pp. 4558–4564, 2004.
- [10] C. Qian, E. A. Decker, H. Xiao, and D. J. McClements, "Physical and chemical stability of β -carotene-enriched nanoemulsions: influence of pH, ionic strength, temperature, and emulsifier type," *Food Chemistry*, vol. 132, no. 3, pp. 1221–1229, 2012.
- [11] H. Y. Song, T. W. Moon, and S. J. Choi, "Storage stability of β -carotene in model beverage emulsions: implication of interfacial thickness," *European Journal of Lipid Science and Technology*, vol. 120, no. 9, article 1800127, 2018.
- [12] D. J. McClements, "Nanoemulsion-based oral delivery systems for lipophilic bioactive components: nutraceuticals and pharmaceuticals," *Therapeutic Delivery*, vol. 4, no. 7, pp. 841–857, 2013.
- [13] T. G. Mason, J. N. Wilking, K. Meleson, C. B. Chang, and S. M. Graves, "Nanoemulsions: formation, structure, and physical properties," *Journal of Physics: Condensed Matter*, vol. 18, no. 41, pp. R635–R666, 2006.
- [14] D. J. McClements and J. Rao, "Food-grade nanoemulsions: formulation, fabrication, properties, performance, biological fate, and potential toxicity," *Critical Reviews in Food Science and Nutrition*, vol. 51, no. 4, pp. 285–330, 2011.
- [15] J. R. Mancuso, D. J. McClements, and E. A. Decker, "Ability of iron to promote surfactant peroxide decomposition and oxidize α -tocopherol," *Journal of Agricultural and Food Chemistry*, vol. 47, no. 10, pp. 4146–4149, 1999.
- [16] M. P. C. Silvestre, W. Chaiyasit, R. G. Brannan, D. J. McClements, and E. A. Decker, "Ability of surfactant headgroup size to alter lipid and antioxidant oxidation in oil-in-water emulsions," *Journal of Agricultural and Food Chemistry*, vol. 48, no. 6, pp. 2057–2061, 2000.
- [17] Y. Yang, E. A. Decker, H. Xiao, and D. J. McClements, "Enhancing vitamin E bioaccessibility: factors impacting solubilization and hydrolysis of α -tocopherol acetate encapsulated in emulsion-based delivery systems," *Food and Function*, vol. 6, no. 1, pp. 84–97, 2015.
- [18] G. C. Chow, "Tests of equality between sets of coefficients in two linear regressions," *Econometrica*, vol. 28, no. 3, pp. 591–605, 1960.
- [19] D. J. McClements, "Ultrasonic determination of depletion flocculation in oil-in-water emulsions containing a non-ionic surfactant," *Colloids and Surfaces A-Physicochemical and Engineering Aspects*, vol. 90, no. 1, pp. 24–35, 1994.
- [20] USEPA, *Estimation Program Interface Suite (TM), Ver. 4.11*, United States Environmental Protection Agency, Washington, DC, USA, 2012.
- [21] J. F. I. Gregory, "Vitamins," in *Fennema's Food Chemistry*, S. Damodaran, K. L. Parkin, and O. R. Fennema, Eds., CRC Press, Boca Raton, FL USA, 4 edition, 2008.
- [22] J. A. Heydinger and D. K. Nakhasi, "Medium chain triacylglycerols," *Journal of Food Lipids*, vol. 3, no. 4, pp. 251–257, 1996.
- [23] E. Choe and D. B. Min, "Mechanisms and factors for edible oil oxidation," *Comprehensive Reviews in Food Science and Food Safety*, vol. 5, no. 4, pp. 169–186, 2006.
- [24] C. S. Boon, D. J. McClements, J. Weiss, and E. A. Decker, "Factors influencing the chemical stability of carotenoids in foods," *Critical Reviews in Food Science and Nutrition*, vol. 50, no. 6, pp. 515–532, 2010.

Review Article

An Overview of Nanotechnology in Food Science: Preparative Methods, Practical Applications, and Safety

Hyunjong Yu,¹ Jun-Young Park,¹ Chang Woo Kwon ,² Sung-Chul Hong,³ Kyung-Min Park,⁴ and Pahn-Shick Chang ^{1,5,6}

¹Department of Agricultural Biotechnology, Seoul National University, Seoul 08826, Republic of Korea

²Corporate Research and Development Center, Ilshinwells Co., Ltd., Cheongju 28176, Republic of Korea

³Systems Biotechnology Research Center, KIST Gangneung Institute of Natural Products, Gangneung 25451, Republic of Korea

⁴Department of Food Science and Biotechnology, Wonkwang University, Iksan 54538, Republic of Korea

⁵Center for Food and Bioconvergence, Seoul National University, Seoul 08826, Republic of Korea

⁶Research Institute of Agriculture and Life Sciences, Seoul National University, Seoul 08826, Republic of Korea

Correspondence should be addressed to Pahn-Shick Chang; pschang@snu.ac.kr

Received 13 July 2018; Accepted 6 September 2018; Published 29 October 2018

Academic Editor: Manuela Curcio

Copyright © 2018 Hyunjong Yu et al. This is an open access article distributed under the Creative Commons Attribution License, which permits unrestricted use, distribution, and reproduction in any medium, provided the original work is properly cited.

As the researches to utilize nanotechnology in food science are advanced, applications of nanotechnology in various fields of the food industry have increased. Nanotechnology can be applied to the food industry for production, processing, storage, and quality control of foods. Nanomaterials, unlike conventional microscale materials, having novel characteristics can improve sensory quality of foods by imparting novel texture, color, and appearance. Nanotechnology has been used to design nanosensors for detection of harmful components in foods and a smart packaging system enabling to recognize food contamination very rapidly and sensitively. Nanoencapsulation is the most significant technology in food science, especially for bioactive compounds and flavors. Targeted delivery systems designed with nanoencapsulation can enhance bioavailability of bioactive compounds after oral administration. In addition, nanoencapsulation enables to control the release of flavors at the desired time and to protect the degradation of flavors during processing and storage. In this review, current applications of nanotechnology in food science including flavor control, enhancement of bioavailability of bioactive compounds, and detection of deleterious substances in foods are presented. Furthermore, this article overviews classification, preparative methods, and safety issues of nanomaterials for food science. This review will be of help to provide comprehensive information for newcomers utilizing nanotechnology to the food sector.

1. Introduction

Nanotechnology is defined as the creation, utilization, and manipulation of materials, devices, or systems at the nanometer scale [1]. Nanomaterials are usually defined as materials smaller than 100 nm and have unique properties when compared with their macroscale counterparts, due to the high surface to volume ratio and novel physicochemical properties such as color, solubility, and thermodynamics [2, 3]. These novel properties provide opportunities to improve the sensory qualities of food such as taste, texture, and color. In addition, nanomaterials can be used to improve

protection mechanisms for food. Utilizing nanosensors and nanopackaging materials enables rapid, sensitive, and reliable detection of microbial contamination, harmful chemicals, and pesticides. Nanoencapsulation systems have the potential to improve food processing by enabling the delivery of bioactive compounds for enhancing bioavailability in foods [4]. In this review, the classification, methods of preparation, and safety issues of nanomaterials are described. The main focus of the review is on nanotechnology applications for foods and includes controlled release of flavors, targeted delivery of bioactive compounds for enhancing the bioavailability, and nanosensors for pathogens

and chemical detection in foods. The aim of this review is to describe the circumstances of nanotechnology utilized in the food sector and to present a comprehensive perspective to food scientists embarking on research about nanotechnology.

2. Classification of Nanocarriers

Nanocarriers can be widely classified as organic-based, inorganic-based, or a combination of both (Table 1) [5]. Organic nanocarriers are comprised of polymeric nanoparticles and lipid-based nanoparticles such as liposomes, nanoemulsions (e.g., micelles and reversed micelles), dendrimers, and carbon-based nanocarriers (e.g., fullerenes and carbon nanotubes). Inorganic nanocarriers are comprised of metallic nanostructures such as quantum dots (Figure 1).

2.1. Polymeric Nanoparticles. Polymeric nanoparticles are based on biocompatible and biodegradable polymers derived from natural and synthetic sources. Biodegradable polymers are typically composed of synthetic polymers such as poly(lactic acid), polyglycolic acid, poly(lactic-co-glycolic acid), poly(ϵ -caprolactone), polymethyl methacrylate, and poly(amino acid). Biodegradable polymers may also consist of natural polymers including, but not limited to, agarose, sodium alginate, chitosan, collagen, and fibrin [6]. Polymers that can provide a controlled drug release of core materials are desirable and have given rise to the popularity of polymeric nanoparticles for anticancer treatment and vaccine delivery [7]. The chemical properties of polymeric nanoparticles and their flexibility has made them suitable for integration with biomaterials (e.g., genetic material and growth factors) and for targeted delivery to stimulate tissue regeneration [8].

2.2. Liposomes. Liposomes are concentric lipid-bilayered nanocarriers comprised of an aqueous core enclosed by surfactant that can be of either natural or synthetic phospholipids. Liposomes can be categorized based on their structure as multilamellar vesicles (MLVs), oligolamellar vesicles (OLVs), and unilamellar vesicles (ULVs). Based on the size of the ULVs, they are further divided into small unilamellar vesicles (SUVs) of 20 to 100 nm diameter, medium unilamellar vesicles (MUVs), large unilamellar vesicles (LUVs) of larger than 100 nm diameter, and giant unilamellar vesicles (GUVs) of larger than 1,000 nm diameter [9]. Liposome-based carrier systems such as immunoliposomes, virosomes, stealth liposomes, and archaeosomes contain lipid bilayers that are biocompatible and may improve the solubility and stability of core materials [10–13].

2.3. Dendrimers. Dendrimers are monodispersed macromolecular compounds composed of repetitively branched molecules around an inner core. Dendrimers can be structured from monomers by convergent or divergent polymerization methods. The desired size and shape of a dendrimer is dependent on the number of branching units

on the repeating unit as seen when using different units, such as chitin, melamine, polyamidoamine, poly L-glutamic acid, polyethyleneimine, polyethylene glycol, and polypropyleneimine [14]. Core materials can be loaded either in the interior or conjugated to a large number of free surface groups to enhance targeted delivery [15].

2.4. Carbon-Based Nanocarriers. Carbon nanotubes are carbon-based tubular structures that are arranged in the shape of a graphene sheet that has been wound into a cylinder or capped at both ends to produce a buckyball shape [14]. There are two carbon-based configurations: single-walled nanotubes (SWNTs) and multiwalled nanotubes (MWNTs). Whereas SWNTs are composed of a single graphene cylinder, MWNTs are composed of more than two concentric cylindrical shells of graphene sheets around a central hollow core [16]. Depending on the functionalization, the nanotubes are further categorized as target-oriented, ligand-attached, solvent-dispersed, and surfactant-grafted. In addition to tubular types, fullerenes are also common carbon-based nanocarriers that represent geometric cage-like structures composed of hexagonal and pentagonal carbon faces [17].

2.5. Hydrogel Nanoparticles. Hydrogels are three-dimensional polymer networks that can absorb a large volume of water or biological fluid. Water-absorbing ability of the hydrogels is dependent on the presence of hydrophilic groups (e.g., -OH, -CONH-, -CONH₂-, and -SO₃H) [18]. The crosslinks in the polymer networks are provided by covalent bonds, hydrogen bonds, dipole-dipole interactions, van der Waals interactions, and physical entanglements [19]. These crosslinks can be categorized by physical entanglements or crystallites, and chemical tie-points and junctions [20]. In a drug delivery system, polymer materials such as alginate, chitosan, poly(vinyl alcohol), poly(ethylene oxide), poly(vinyl pyrrolidone), and poly-N-isopropylacrylamide are widely used to make cross-linked networks. These networks are affected by the electric field, light intensity, pH, and temperature [21, 22].

2.6. Quantum Dots. Quantum dots are nanocrystals of inorganic fluorescent semiconducting atoms and have a size range of 2–10 nm. The semiconducting material, cadmium selenide, consists of a core, and aqueous zinc sulfide shell that insulates the core to enhance optical properties. Quantum dots can be constructed to emit light from the ultraviolet to infrared wavelength. Emitted wavelengths are intense enough to be detected at the subcellular level [23]. In addition, quantum dots are a stable and inert delivery vessel as biomolecules can be conjugated to the outer aqueous shell [24].

2.7. Nanoemulsions. Nanoemulsions consist of droplets with a size range of 10–100 nm and can be categorized into two types based on the relative spatial organization of the oil and water phases. A micellar system comprised of oil

TABLE 1: Physicochemical properties and applications of various nanomaterials.

Types	Size (nm)	Physicochemical properties	Applications
Carbon nanotubes	0.5–3 (diameter) 20–1,000 (length)	Third allotropic crystalline form of carbon sheets either single layer (single-walled nanotube, SWNT) or multiple layer (multiwalled nanotube, MWNT). These crystals have remarkable strength and unique electrical properties (conducting, semiconducting, or insulating)	Functionalization enhanced solubility, penetration to cell cytoplasm and to nucleus, as Carrier for gene delivery, peptide delivery
Dendrimer	<10	Highly branched, nearly monodispersed polymer system obtained from controlled polymerization; three main parts core, branch, and surface	Long circulatory, controlled delivery of bioactive compounds, targeted delivery of bioactive compounds to macrophages, liver targeting
Liposome	50–100	Phospholipid vesicles, biocompatible, versatile, good entrapment efficiency and different vesicle types depending on the structure multilamellar vesicles (MLV): >500 nm; oligolamellar vesicle (OLV): 100–500 nm; unilamellar vesicles, and unilamellar types depending on the size as small unilamellar vesicles (SUV): 20–100 nm; large unilamellar vesicles (LUV): >100 nm; giant unilamellar vesicles (GUV): >1,000 nm	Long circulatory, offer passive and active delivery of gene, protein, peptide, and various other components
Metallic nanoparticles	<100	Gold and silver colloids, very small size resulting in high surface area available for functionalization, high stability	Drug and gene delivery, highly sensitive diagnostic assays, thermal ablation, and radiotherapy enhancement
Nanocrystals quantum dots	2–9.5	Semiconducting material synthesized with II-VI and III-V column element; size between 10 and 100 Å; bright fluorescence, narrow emission, broad UV excitation, and high photo stability	Long-term multiple color imaging of liver cell; DNA hybridization, immunoassay; receptor-mediated endocytosis; labeling of breast cancer marker Her2 surface of cancer cells
Polymeric micelles	10–100	Block amphiphilic copolymer micelles, high drug entrapment, payload, and biostability	Long circulatory, target specific active and passive drug delivery, diagnostic value Excellent carrier for controlled and sustained delivery of drugs; Stealth and surface modified nanoparticles used for active and passive delivery of bioactive compounds
Polymeric nanoparticles	10–1,000	Biodegradable, biocompatible, and offer complete drug protection	

droplets suspended within a water phase is referred to as an oil-in-water (O/W) nanoemulsion, whereas a reversed micellar system that is comprised of water droplets suspended in an oil phase is referred to as a water-in-oil (W/O) nanoemulsion [25]. O/W nanoemulsions are usually kinetically stable and slightly turbid to transparent. Due to the weak light scattering of particles in nanoemulsions, they are suitable for incorporation into optically transparent products such as fortified soft drinks and waters, whitening cosmetics, sauces, and soups [26–29].

3. Preparation Methods for Nanocarriers

There are several conventional and emerging methods for the preparation of nanocarriers. Typical methods based on emulsification technology are most commonly used but specific methods must be developed for each type of nanocarrier. In this section, the conventional and emerging

methods for the preparation of nanocarriers are described (Table 2) [18].

3.1. Conventional Methods

3.1.1. High-Pressure Homogenization. High-pressure homogenization has been widely used for the preparation of lipid-based nanocarriers such as nanoemulsions and solid lipid nanoparticles. High shear stress produces high pressures (100–2,000 bar), resulting in disruption of particles into the nanometer range [30]. This method is divided into hot homogenization and cold homogenization. The former gives lower particle size because of the decreased viscosity of the phase at a higher temperature but may result in an increased degradation rate of the core material in the nanocarrier. The latter was developed to overcome the limitations of the hot homogenization, incurred by high temperatures, and involves the

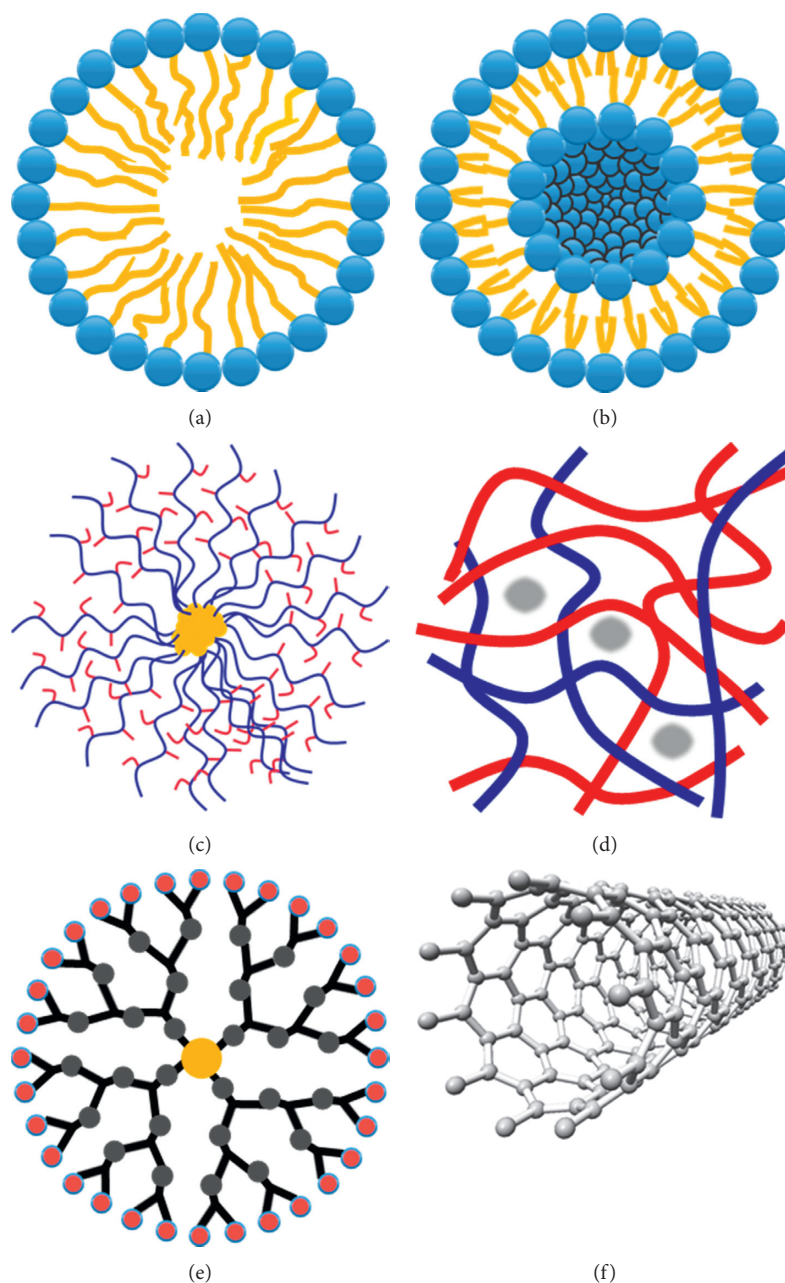


FIGURE 1: Schematic diagrams of 6 types of nanocarriers. (a) Micelle. (b) Liposome. (c) Polymeric nanoparticle. (d) Hydrogel nanoparticle. (e) Dendrimer. (f) Carbon nanotube.

solubilization or dispersion of core material above the melting point of nanocarriers (5–10°C) [31]. High-pressure homogenization has high encapsulation efficiency thereby enabling the controlled release of the core material.

3.1.2. Solvent Emulsification-Diffusion Method. Solvent emulsification-diffusion is the most commonly used method for the preparation of lipid-based and polymeric-based nanoparticles. The oil phase contains the polymer in an organic solvent whereas the aqueous phase contains a stabilizer in water. When mixed together, the water induces the

diffusion of the organic solvent resulting in the formation of nanoparticles [31]. The solvent used for the preparation of nanoparticles must be removed. Moreover, emulsification methods for the production of more complex nanocarriers required a double emulsion [32]. The first step is to add a small amount of aqueous media to a larger volume of immiscible organic solvents to dissolve the phospholipid. The organic solution containing the water droplets is added to a large volume of aqueous media producing a water-in-oil-in-water (W/O/W) emulsion. A lipid monolayer forms around the organic droplets resulting in aqueous cores surrounded by two lipid monolayers that are separated by an organic layer. Unilamellar liposomes with high entrapment

TABLE 2: Conventional and emerging methods for preparation of nanocarriers.

Preparation method	Advantages	Disadvantages
<i>Conventional methods</i>		
High homogenization	Large-scale production, high encapsulation efficiency	Deactivation of core material in nanocarrier
Solvent injection (ethanol or ether)	Ability to control vesicle size	Dilution of nanocarrier, heterogeneous population, use of high temperature
Reverse phase evaporation	High encapsulation efficiency, economic	Organic solvent traces, not suitable for fragile molecules or food ingredients
Solvent-emulsification	High encapsulation efficiency	Multivesicular, unstable
Postformation processing	Reduced processing time, high encapsulation efficiency	Low lamellarity and heterogeneity
<i>Emerging methods</i>		
Microfluidic channel method	Synthesis of monodisperse nanocarrier, high encapsulation efficiency	Fabrication could be complex and needs optimization
Supercritical fluid method	Control over particle formation, easily translated to large-scale production, environment-friendly	Elevated pressure and temperatures
Self-assembly method	Handy and controllable method for changing the shape of nanocarriers	Poorly understood experimental conditions
Spray drying	Environment-friendly process, high encapsulation efficiencies	Expense and time-required
Freeze drying of monophasic solutions	Monodisperse nanocarrier that can be stored for a long time in a sealed container	Time-required
Membrane contactor method	Nanocarriers have homogeneous and small size, high encapsulation efficiency, simplicity for scale-up	Hydrophilic drug encapsulation needs optimization

of the initial aqueous media can then be formed by the removal of the organic solvent [33, 34].

3.1.3. Injection Methods. The two injection methods for preparation of lipid-based nanocarriers utilize ether or ethanol. Diethyl ether and ether-methanol mixtures are widely used for dissolving the lipids [35]. The lipid-ether solution is injected into the aqueous media and nanocarrier vesicles are formed [36, 37]. LUVs are formed as the injection speed increases. An advantage of the ether injection method is the removal of the solvent from the product, allowing extended process-running time and producing a concentrated liposomal product with high entrapment efficiencies. However, this technique creates a heterogeneous population (70–200 nm) with a requirement for high temperatures to encapsulate the organic products [38].

The ethanol injection method dissolves the lipids in ethanol [39]. The high concentration of the core materials in the aqueous phase can be increased by multiple injections of the lipid solution. An advantage of this technique is the quick and simple formation of MLVs [40]. Disadvantages include producing a heterogeneous population (30–110 nm), low concentration of enabled liposomes, and a high level of difficulty when removing the ethanol. Ethanol removal poses a significant problem when using liposomes for biological cell culture or microorganism treatment, as all of ethanol must be removed [41].

3.1.4. Reverse Phase Evaporation Method. The reverse phase evaporation method was first shown by Szoka and Papahadjopoulos and is based on the creation of reversed micelles

[42]. Reversed micelles are in the aqueous phase with a central core surrounded by lipid and dispersed in an organic solvent [43]. Reversed micelles are produced by dissolving the lipids in an organic solvent, adding a small volume of aqueous phase, and sonicating the solution to produce inverted micelles. The organic solvent is removed using a rotary evaporator resulting in a viscous gel [44]. When sufficient solvent has been removed, the gel collapses, and an aqueous suspension of vesicles forms [45]. The disadvantage of the reverse phase evaporation method is that the compound to be encapsulated within the vesicles is in contact with an organic solvent. Consequently, this method is not suitable for fragile molecules or food ingredients despite the potential to achieve encapsulation efficiencies of up to 80% [44].

3.2. Emerging Technologies

3.2.1. Microfluidic Channel Method. The microfluidic channel method consists of two silicon wafers such as polydimethylsiloxane (PDMS), vertically attached together [46]. In this case the microchannel, the width of which is 200–1,000 μm , was carved on one side of the PDMS layer. Two inlet lines (outside inlet and central inlet) and one outlet were directly connected with the microchannel. In the case of liposome preparation, a lipid solution is injected into the central inlet while aqueous solutions are injected to the outside inlet, which intersects with the central position. Liposomes are formed due to the different shear forces that are generated at the liquid interfaces by the changing flow rate ratio. The process involves a stream of lipid dissolved in solvent passing between two aqueous streams in

a microfluidic channel. Mixing occurs at the liquid interfaces creating nanocarriers [47, 48]. An advantage of this technique is the ease of control concerning vesicle size and monodispersion although a continuous system is yet to be developed.

3.2.2. Supercritical Fluid Methods. Methods involving supercritical fluids for nanocarrier preparation are used in pharmaceutical research and industry to address limitations associated with conventional methods [32]. A supercritical fluid can be either a liquid or gas, such as water or carbon dioxide, under conditions that are above its thermodynamic critical point of temperature and pressure (e.g., carbon dioxide at 60°C and 250 bar). Supercritical fluid methods are separated into two categories: rapid expansion and anti-solvent precipitation [31]. The advantages of these methods over conventional methods include a reduction of impact on the environment and improved design of particle morphology (size and shape). The disadvantage of this method is poor scalability for industrial manufacturing, which may result in variable particle characteristics [49].

3.2.3. Self-Assembly Methods. Self-assembly is the physical process where preexisting disordered components or molecules arrange themselves into regulated structures by physical or chemical reactions without external influences [50]. Protein folding and liposome assembly are examples of self-assembly. Self-assembly has the potential to be used in nanotechnology, where a desired structure could be encoded into the properties of the nanomaterials being used. Nevertheless, it has not been used to its full potential as yet because experimental conditions under which a set of components self-assemble remain poorly understood [31].

4. Applications in the Food Sector

4.1. Flavor Control. Flavors are considered important ingredients in any foods, playing a significant role in sensory quality and influencing the consumption of food. The increasing interest on the stability of flavors in different types of food is linked to the quality and acceptability of the food [51]. However, it is difficult to control and stabilize flavors, mainly during the storage and manufacturing processes [52]. To limit flavor degradation or loss during processing and storage, it is beneficial to encapsulate the flavor before use in food, improving chemical stability, and providing controlled release. Encapsulation with a protective carrier guard against interactions between flavors, reactions induced by light, and oxidation [53]. Popular carriers are biopolymers such as carbohydrates (e.g., starch, maltodextrins, and dextrose), gums (e.g., gum arabic, alginates, and carrageenan), proteins (e.g., whey proteins and gelatin), and chitosan [51]. When designing an encapsulation system, factors for consideration are the physico-chemical properties of the flavor (solubility) and the carrier (viscosity). Especially, the carriers should not react with the flavors [54].

Nanoencapsulation packs substances into nanocarriers and provides final product functionality that includes controlled release of the core materials [55]. With a properly designed controlled release system such as sustained release and burst release, the flavors can be released at the desired time and at a desired rate [56]. This system has a slow or near zero release of flavors in solvated conditions but have a burst release due to changes in pH and/or ionic strength or temperature when a food product is in contact with saliva. Nanocarrier encapsulation provides sustained release of the flavor compounds maintaining the flavor quality during shelf-life storage. Sustained release can be achieved by encapsulating a compound in appropriate nanocarriers that maintain physical stability under the expected performing conditions and durations. Factors influencing the release mechanisms include the type of carrier to encapsulate the flavors, the method of preparation, and the environment where the flavors are released. On the release mechanism, processes of diffusion, degradation, melting, and osmosis may also be important [52]. Controlled release of flavor compounds can be manipulated by interactions between core materials and carrier materials.

4.2. Enhancing the Bioavailability of Bioactive Compounds. The bioavailability of bioactive compounds is the most important factor for consideration when producing functional foods. Bioavailability is defined as the amount of a bioactive compound that can enter the bloodstream [57]. When bioactive compounds are administrated orally, these compounds pass through the mouth, stomach, and intestines to access the bloodstream. Protection against the gastrointestinal tract (GIT) environment requires defense against digestive enzymes, pH, and temperature [33]. It is necessary to increase the stability of bioactive compounds and improve their absorption by epithelium cells, to increase bioavailability.

Several target delivery systems using nanocarriers have been developed to improve the bioavailability of various bioactive compounds. Bioactive compounds can be classified into lipophilic and hydrophilic types based on their solubility in water. Many of the bioactive compounds are highly lipophilic molecules, such as polyunsaturated lipids, oil-soluble vitamins, phytosterols, curcuminoids, carotenoids, and flavonoids. The lipophilic bioactive compounds have low bioavailability within the human GIT due to poor absorption in the gastrointestinal fluids [58]. These bioactive compounds are usually encapsulated to resist the high acidity and degradation by enzymes in the stomach and duodenum but also to enhance their low water-solubility, which interferes with applications in food such as beverages [59].

Nanocarriers provide an increased surface area and enhance solubility and bioavailability of the encapsulated bioactive compounds when compared to microsize carriers. Reducing the particle size improves the delivery efficiency, solubility, and biological activity of the compounds due to greater surface area per unit [60]. It was demonstrated that the bioavailability of β -carotene encapsulated within O/W

nanoemulsions increased with decreasing particle size [58]. These findings have been confirmed with Coenzyme Q₁₀ and lipophilic compounds when fed to animals [61]. It was concluded that a more rapid digestion of the lipid phase in emulsions occurred when the lipid droplet size decreased. More mixed micelles cause to solubilize the lipophilic bioactive compounds within the fluids of the small intestine [58]. Although carbohydrate, protein, and lipid-based nanocarriers have several advantages, the carbohydrate- and protein-based carriers currently have low potential for scale-up due to the requirement for complicated chemical or heat treatments in the process that cannot be adequately controlled. On the other hand, lipid-based nanocarriers, including nanoemulsions and nanoliposomes, solid lipid nanoparticles, biopolymer nanoparticles, and microgels, have a greater potential for industrial scale-up and have the advantage of higher encapsulation efficiency and low toxicity [1].

Many targeted delivery systems have been proposed but none can currently be considered as a universally applicable system for bioactive compounds because individual bioactive compounds have their own characteristic molecular structure necessitating different systems. It was demonstrated that each compound could have differences in molecular weight, polarity, and solubility, resulting in the need for different encapsulation approaches to meet the specific physicochemical and molecular requirements for a specific bioactive compound [59]. When targeted delivery systems are designed, an important requirement is encapsulation efficiency of core materials into carriers. The efficiency is related to the type of molecule to be encapsulated and the specific products that serve as carriers [62]. Whilst high encapsulation efficiency is important, it is essential to choose a system that can be easily incorporated without interfering with the texture and taste of the food. Food products have various physicochemical properties and sensory characteristics, such as appearance, texture, flavor, and mouthfeel. Some food products are optically clear low-viscosity liquids (such as fortified waters), whereas others are optically opaque semisolids or solids (such as yogurts and spreads) [58]. Delivery systems for a bioactive compound must be incorporated into the final food product without adverse effect on its quality.

4.3. Detection of Deleterious Substances in Foods. Nanosensors are an important area in food industry. These devices may be able to detect and quantify low concentrations of pathogens, organic compounds, and other chemicals. Furthermore, these devices have the potential to exhibit high sensitivity, fast response, and recovery and integrate addressable arrays on a large scale [63].

An example of a nanosensor application is organophosphate for pesticide detection in fruit and water [64]. High interface sensitivity caused by the loading of more enzyme/antibody, low detection limits, and excellent selectivity are some of the advantages of nanosensors. An example of applying semiconductors to the use of quantum dots in the detection of the pesticide 2,4-dichlorophenoxyacetic acid was studied [65]. Quantum dots are

semiconductor fluorescent nanoparticles, which can be used to monitor pesticide with high sensitivity [66]. Another example of a nanosensor is an invention by Kraft Foods. They developed a nanosensor to be incorporated within food packaging consisting of an array of nanosensors that are extremely sensitive to gases produced by food as it spoils. As the food spoils and these gases are detected, the sensor strip changes color providing a clear optical signal of food freshness [66].

Nanosensors have also been used for pathogen and mycotoxin detection in foods. Conventional control of these microorganisms is complicated, but the nanosensor can rapidly detect toxins and pathogens in foods, during processing, and in storage. The nanosensor can be used for smart packaging where the sensor fluoresces in different colors when the sensor contacts with different food pathogens. Different devices have been developed to detect numerous toxins, pathogens, and chemicals in food packaging using nanowires and antibodies [58].

In the food market, nanoelectromechanical systems (NEMS) are already in use to analyze deleterious substances. NEMS could be used in quality control devices for foods because they consist of advanced transducers for specific detection of chemical and biochemical signals [67]. The use of nanosensors has several advantages for food technologies, such as portable instrumentation with quick responses and low costs. Nanocantilevers are another innovative class of nanosensors. The detection is based on the principle to detect biological-binding interactions through physical and/or electromechanical signals (e.g., antigen and antibody, enzyme and substrate or cofactor, and receptor and ligand) [68]. These nanosensors consist of tiny pieces of silicon-based materials that have the capability of recognizing proteins and detecting pathogenic bacteria and viruses [69].

5. Safety Issues in Food Nanotechnology

A recent innovation in nanotechnology has fostered a number of nano-based scientific and industrial areas with the market for nanomaterial-containing products experiencing steady growth. Despite its various advantages, the rapid proliferation of nanotechnology in food technology has also raised public safety and environmental, ethical, policy, and regulatory issues. Nanomaterials may exhibit substantially different physicochemical and biological properties compared to their conventional form, and these unknown properties may create unpredictable hazards.

The potential hazard of direct contact of nanomaterials with humans through oral intake is still a concern, even though the nanoencapsulation technology of bioactive compounds has been very extensively studied in the food industry [70]. The fate of nanocarriers in GIT varies greatly depending on their susceptibility to hydrolysis by digestive enzymes and the conditions of GIT [71]. Nevertheless, free nanocarriers typically cross intestinal/cellular barriers, which could lead to an increase in the bioaccumulation of foreign materials in human blood, cells, and tissues.

The high usage of organic solvents and emulsifiers for the preparation of nanocarriers can lead to risks due to their

toxicity [25]. The organic solvents must be removed by an evaporation process but can lead to unexpected residual solvents remaining in the final product, causing safety implications if their concentration is unknown. Solvents and emulsifiers have been classified as toxic, with safe usage levels documented by organizations including the World Health Organization (WHO), the Food and Drug Administration (FDA), and the European Food Safety Authority (EFSA) [25].

In fact, the available information on the potential safety risks that may arise from the nanotechnology is sparse. The safety of nanomaterials and associated hazards remain uninvestigated and require further risk assessment. The direct and indirect effects of nanomaterials to human health must be explored and include the biological fate of nanomaterials after digestion, their behavior within GIT, and their possible interactions with biological systems. Moreover, it is of great importance to develop regulatory controls to protect the public from potential adverse effects of nanotechnology [72].

Modern food legislation, with the help of several world organizations, regulates many issues related to consumer health, many of which may be applied to nanotechnology and nanomaterials used in foods. Despite the current lack of specific regulation and risk management for nanotechnology, it is evident that there have been significant advances in the application and regulation of novel nanotechnology in the food industry. By keeping modern food regulations, any new specific nanotechnology regulation, information transparency and a willingness to provide the public with information in mind, the safety of nanomaterials in the food industry can be assured.

6. Conclusions

Advances in nanotechnology have brought benefits for the food industry, with many applications yet to be realized. Nanotechnology has already demonstrated its applicability in the areas of food production, processing, packaging, and safety. Although nanotechnology in foods has progressed year upon year, further research is necessary to maximize the number of uses within the food industry. In particular, the safety concerns regarding the consumption of nanomaterials in foods must be addressed before the products are released to the market. Therefore, it is necessary to standardize test procedures to determine the impact of nanomaterials. Furthermore, regulations must be introduced that can ease consumer worry and improve consumer acceptability. The uptake of nanotechnology will cause rapid development of the food industry with nanotechnology-based foods becoming more readily available to the consumer.

Conflicts of Interest

The authors declare that they have no conflicts of interest.

Authors' Contributions

Hyunjong Yu and Jun-Young Park contributed equally to this work.

Acknowledgments

This work was supported by the National Research Foundation of Korea (NRF) grant funded by the Korea Government (MSIT) (no. NRF-2017R1A2B4009230).

References

- [1] M. Fathi, M.-R. Mozafari, and M. Mohebbi, "Nano-encapsulation of food ingredients using lipid based delivery systems," *Trends in Food Science Technology*, vol. 23, no. 1, pp. 13–27, 2012.
- [2] M. Zhu, G. Nie, H. Meng, T. Xia, A. Nel, and Y. Zhao, "Physicochemical properties determine nanomaterial cellular uptake, transport, and fate," *Accounts of Chemical Research*, vol. 46, no. 3, pp. 622–631, 2012.
- [3] T. Singh, S. Shukla, P. Kumar, V. Wahla, V. K. Bajpai, and I. A. Rather, "Application of nanotechnology in food science: perception and overview," *Frontiers in Microbiology*, vol. 8, p. 1501, 2017.
- [4] Q. Chaudhry, M. Scotter, J. Blackburn et al., "Applications and implications of nanotechnologies for the food sector," *Food Additives and Contaminants*, vol. 25, no. 3, pp. 241–258, 2008.
- [5] D. K. Mishra, R. Shandilya, and P. K. Mishra, "Lipid based nanocarriers: a translational perspective," *Nanomedicine: Nanotechnology, Biology and Medicine*, vol. 14, no. 7, pp. 2023–2050, 2018.
- [6] L. Wan-Ju and S. T. Rocky, "Polymeric scaffolds for cartilage tissue engineering," *Macromolecular Symposia*, vol. 227, no. 1, pp. 65–76, 2005.
- [7] F. Masood, "Polymeric nanoparticles for targeted drug delivery system for cancer therapy," *Materials Science and Engineering*, vol. 60, pp. 569–578, 2016.
- [8] S. Saravanan, A. Chawla, M. Vairamani, T. Sastry, K. Subramanian, and N. Selvamurugan, "Scaffolds containing chitosan, gelatin and graphene oxide for bone tissue regeneration *in vitro* and *in vivo*," *International Journal of Biological Macromolecules*, vol. 104, pp. 1975–1985, 2017.
- [9] A. Sharma and U. S. Sharma, "Liposomes in drug delivery: progress and limitations," *International Journal of Pharmaceutics*, vol. 154, no. 2, pp. 123–140, 1997.
- [10] S. E. Alavi, H. Mansouri, M. K. M. Esfahani, F. Movahedi, A. Akbarzadeh, and M. Chiani, "Archaeosome: as new drug carrier for delivery of paclitaxel to breast cancer," *Indian Journal of Clinical Biochemistry*, vol. 29, no. 2, pp. 150–153, 2014.
- [11] K. P. Mineart, S. Venkataraman, Y. Y. Yang, J. L. Hedrick, and V. M. Prabhu, "Fabrication and characterization of hybrid stealth liposomes," *Macromolecules*, vol. 51, no. 8, pp. 3184–3192, 2018.
- [12] M. Merino, S. Zalba, and M. J. Garrido, "Immunoliposomes in clinical oncology: state of the art and future perspectives," *Journal of Controlled Release*, vol. 275, pp. 162–176, 2018.
- [13] J. Fleddermann, E. Diamanti, S. Azinas et al., "Virosome engineering of colloidal particles and surfaces: bioinspired fusion to supported lipid layers," *Nanoscale*, vol. 8, no. 15, pp. 7933–7941, 2016.
- [14] R. Duncan and L. Izzo, "Dendrimer biocompatibility and toxicity," *Advanced Drug Delivery Reviews*, vol. 57, no. 15, pp. 2215–2237, 2005.
- [15] A. D'emanuele and D. Attwood, "Dendrimer–drug interactions," *Advanced Drug Delivery Reviews*, vol. 57, no. 15, pp. 2147–2162, 2005.

- [16] C. Pham-Huy, P. Dramou, L. A. Pham-Huy, D. Xiao, and H. He, "Carbon nanotubes used as nanocarriers in drug and biomolecule delivery," in *Drug Delivery Approaches and Nanosystems*, vol. 1, pp. 163–212, Apple Academic Press, Waretown, NJ, USA, 2017.
- [17] J. E. N. Dolatabadi, Y. Omid, and D. Losic, "Carbon nanotubes as an advanced drug and gene delivery nanosystem," *Current Nanoscience*, vol. 7, no. 3, pp. 297–314, 2011.
- [18] K. Sharma, B. S. Kaith, V. Kumar et al., "Synthesis and properties of poly(acrylamide-aniline)-grafted gum ghatti based nanospikes," *RSC Advances*, vol. 3, no. 48, pp. 25830–25839, 2013.
- [19] J. D. A. Pachioni-Vasconcelos, A. M. Lopes, A. C. Apolinario et al., "Nanostructures for protein drug delivery," *Biomaterials Science*, vol. 4, no. 2, pp. 205–218, 2016.
- [20] N. Peppas, P. Bures, W. Leobandung, and H. Ichikawa, "Hydrogels in pharmaceutical formulations," *European Journal of Pharmaceutics and Biopharmaceutics*, vol. 50, no. 1, pp. 27–46, 2000.
- [21] J. Lin, Q. Tang, D. Hu, X. Sun, Q. Li, and J. Wu, "Electric field sensitivity of conducting hydrogels with interpenetrating polymer network structure," *Colloids and Surfaces A: Physicochemical and Engineering Aspects*, vol. 346, no. 1–3, pp. 177–183, 2009.
- [22] Y.-Y. Xiao, X.-L. Gong, Y. Kang, Z.-C. Jiang, S. Zhang, and B.-J. Li, "Light-, pH- and thermal-responsive hydrogels with the triple-shape memory effect," *Chemical Communications*, vol. 52, no. 70, pp. 10609–10612, 2016.
- [23] W. Qu, W. Zuo, N. Li et al., "Design of multifunctional liposome-quantum dot hybrid nanocarriers and their biomedical application," *Journal of Drug Targeting*, vol. 25, no. 8, pp. 661–672, 2017.
- [24] D. Mo, L. Hu, G. Zeng et al., "Cadmium-containing quantum dots: properties, applications, and toxicity," *Applied Microbiology and Biotechnology*, vol. 101, no. 7, pp. 2713–2733, 2017.
- [25] D. J. McClements and J. Rao, "Food-grade nanoemulsions: formulation, fabrication, properties, performance, biological fate, and potential toxicity," *Critical Reviews in Food Science and Nutrition*, vol. 51, no. 4, pp. 285–330, 2011.
- [26] T. Wang, S. Soyama, and Y. Luo, "Development of a novel functional drink from all natural ingredients using nanotechnology," *LWT-Food Science and Technology*, vol. 73, pp. 458–466, 2016.
- [27] P. Boonme, V. B. Junyaprasert, N. Suksawad, and S. Songkro, "Microemulsions and nanoemulsions: novel vehicles for whitening cosmeceuticals," *Journal of Biomedical Nanotechnology*, vol. 5, no. 4, pp. 373–383, 2009.
- [28] H. D. Silva, M. A. Cerqueira, and A. A. Vicente, "Nanoemulsions for food applications: development and characterization," *Food and Bioprocess Technology*, vol. 5, no. 3, pp. 854–867, 2012.
- [29] K. Lane, E. Derbyshire, C. Smith, K. Mahadevan, and W. Li, "Sensory evaluation of a yogurt drink containing an omega-3 nanoemulsion with enhanced bioavailability," *Proceedings of the Nutrition Society*, vol. 72, no. OCE2, p. E99, 2013.
- [30] R. H. Müller, K. Mäder, and S. Gohla, "Solid lipid nanoparticles (SLN) for controlled drug delivery—a review of the state of the art," *European Journal of Pharmaceutics and Biopharmaceutics*, vol. 50, no. 1, pp. 161–177, 2000.
- [31] B. Mishra, B. B. Patel, and S. Tiwari, "Colloidal nanocarriers: a review on formulation technology, types and applications toward targeted drug delivery," *Nanomedicine: Nanotechnology, Biology and Medicine*, vol. 6, no. 1, pp. 9–24, 2010.
- [32] K. Otake, T. Imura, H. Sakai, and M. Abe, "Development of a new preparation method of liposomes using supercritical carbon dioxide," *Langmuir*, vol. 17, no. 13, pp. 3898–3901, 2001.
- [33] Y. P. Patil and S. Jadhav, "Novel methods for liposome preparation," *Chemistry and Physics of Lipids*, vol. 177, pp. 8–18, 2014.
- [34] T. Wang, Y. Deng, Y. Geng, Z. Gao, J. Zou, and Z. Wang, "Preparation of submicron unilamellar liposomes by freeze-drying double emulsions," *Biochimica et Biophysica Acta (BBA)-Biomembranes*, vol. 1758, no. 2, pp. 222–231, 2006.
- [35] D. W. Deamer, "Preparation and properties of ether injection liposomes," *Annals of the New York Academy of Sciences*, vol. 308, no. 1, pp. 250–258, 1978.
- [36] J. Dua, A. Rana, and A. Bhandari, "Liposome: methods of preparation and applications," *International Journal of Pharmaceutical Studies and Research*, vol. 3, no. 2, pp. 14–20, 2012.
- [37] A. Samad, Y. Sultana, and M. Aqil, "Liposomal drug delivery systems: an update review," *Current Drug Delivery*, vol. 4, no. 4, pp. 297–305, 2007.
- [38] A. Akbarzadeh, R. Rezaei-Sadabady, S. Davaran et al., "Liposome: classification, preparation, and applications," *Nanoscale Research Letters*, vol. 8, no. 1, p. 102, 2013.
- [39] M. Pons, M. Foradada, and J. Estelrich, "Liposomes obtained by the ethanol injection method," *International Journal of Pharmaceutics*, vol. 95, no. 1–3, pp. 51–56, 1993.
- [40] C. Jaafar-Maalej, R. Diab, V. Andrieu, A. Elaissari, and H. Fessi, "Ethanol injection method for hydrophilic and lipophilic drug-loaded liposome preparation," *Journal of Liposome Research*, vol. 20, no. 3, pp. 228–243, 2010.
- [41] P. Stano, S. Bufali, C. Pisano et al., "Novel camptothecin analogue (gimatecan) containing liposomes prepared by the ethanol injection method," *Journal of Liposome Research*, vol. 14, no. 1–2, pp. 87–109, 2004.
- [42] F. Szoka and D. Papahadjopoulos, "Procedure for preparation of liposomes with large internal aqueous space and high capture by reverse-phase evaporation," *Proceedings of the National Academy of Sciences*, vol. 75, no. 9, pp. 4194–4198, 1978.
- [43] T. Nagata, K. Okada, I. Takebe, and C. Matsui, "Delivery of tobacco mosaic virus RNA into plant protoplasts mediated by reverse-phase evaporation vesicles (liposomes)," *Molecular and General Genetics MGG*, vol. 184, no. 2, pp. 161–165, 1981.
- [44] T. Imura, K. Otake, S. Hashimoto et al., "Preparation and physicochemical properties of various soybean lecithin liposomes using supercritical reverse phase evaporation method," *Colloids and Surfaces B: Biointerfaces*, vol. 27, no. 2–3, pp. 133–140, 2003.
- [45] K. Otake, T. Shimomura, T. Goto et al., "Preparation of liposomes using an improved supercritical reverse phase evaporation method," *Langmuir*, vol. 22, no. 6, pp. 2543–2550, 2006.
- [46] S.-H. Song, C.-K. Lee, T.-J. Kim, I.-c. Shin, S.-C. Jun, and H.-I. Jung, "A rapid and simple fabrication method for 3-dimensional circular microfluidic channel using metal wire removal process," *Microfluidics and Nanofluidics*, vol. 9, no. 2–3, pp. 533–540, 2010.
- [47] J. Shi, H. Huang, Z. Stratton, Y. Huang, and T. J. Huang, "Continuous particle separation in a microfluidic channel via standing surface acoustic waves (SSAW)," *Lab on a Chip*, vol. 9, no. 23, pp. 3354–3359, 2009.
- [48] J. Shi, X. Mao, D. Ahmed, A. Colletti, and T. J. Huang, "Focusing microparticles in a microfluidic channel with standing surface acoustic waves (SSAW)," *Lab on a Chip*, vol. 8, no. 2, pp. 221–223, 2008.

- [49] L. Lesoin, C. Crampon, O. Boutin, and E. Badens, "Preparation of liposomes using the supercritical anti-solvent (SAS) process and comparison with a conventional method," *Journal of Supercritical Fluids*, vol. 57, no. 2, pp. 162–174, 2011.
- [50] S. H. Ansari, F. Islam, and M. Sameem, "Influence of nanotechnology on herbal drugs: a review," *Journal of Advanced Pharmaceutical Technology and Research*, vol. 3, no. 3, pp. 142–146, 2012.
- [51] B. N. Estevinho and F. Rocha, "A key for the future of the flavors in food industry," in *Nanotechnology Applications in Food*, A. E. Oprea and A. M. Grumezescu, Eds., pp. 1–19, Academic Press, Cambridge, MA, USA, 2017.
- [52] A. Madene, M. Jacquot, J. Scher, and S. Desobry, "Flavour encapsulation and controlled release—a review," *International Journal of Food Science Technology*, vol. 41, no. 1, pp. 1–21, 2006.
- [53] T. A. Tari and R. S. Singhal, "Starch based spherical aggregates: reconfirmation of the role of amylose on the stability of a model flavouring compound, vanillin," *Carbohydrate Polymers*, vol. 50, no. 3, pp. 279–282, 2002.
- [54] A. Gharsallaoui, G. Roudaut, O. Chambin, A. Voilley, and R. Saurel, "Applications of spray-drying in microencapsulation of food ingredients: an overview," *Food Research International*, vol. 40, no. 9, pp. 1107–1121, 2007.
- [55] M. X. Quintanilla-Carvajal, B. H. Camacho-Díaz, L. S. Meraz-Torres et al., "Nanoencapsulation: a new trend in food engineering processing," *Food Engineering Reviews*, vol. 2, no. 1, pp. 39–50, 2010.
- [56] B. N. Estevinho, F. Rocha, L. Santos, and A. Alves, "Microencapsulation with chitosan by spray drying for industry applications—A review," *Trends in Food Science Technology*, vol. 31, no. 2, pp. 138–155, 2013.
- [57] A. F. Esfanjani, E. Assadpour, and S. M. Jafari, "Improving the bioavailability of phenolic compounds by loading them within lipid-based nanocarriers," *Trends in Food Science Technology*, vol. 76, pp. 56–66, 2018.
- [58] D. J. McClements, "Nanoscale nutrient delivery systems for food applications: improving bioactive dispersibility, stability, and bioavailability," *Journal of Food Science*, vol. 80, no. 7, pp. 1602–1611, 2015.
- [59] P. de Vos, M. M. Faas, M. Spasojevic, and J. Sikkema, "Encapsulation for preservation of functionality and targeted delivery of bioactive food components," *International Dairy Journal*, vol. 20, no. 4, pp. 292–302, 2010.
- [60] R. Shegokar and R. H. Müller, "Nanocrystals: industrially feasible multifunctional formulation technology for poorly soluble actives," *International Journal of Pharmaceutics*, vol. 399, no. 1-2, pp. 129–139, 2010.
- [61] H. Cho, L. Salvia-Trujillo, J. Kim, Y. Park, H. Xiao, and D. McClements, "Droplet size and composition of nutraceutical nanoemulsions influences bioavailability of long chain fatty acids and Coenzyme Q10," *Food Chemistry*, vol. 156, pp. 117–122, 2014.
- [62] N. V. N. Jyothi, P. M. Prasanna, S. N. Sakarkar, K. S. Prabha, P. S. Ramaiah, and G. Srawan, "Microencapsulation techniques, factors influencing encapsulation efficiency," *Journal of Microencapsulation*, vol. 27, no. 3, pp. 187–197, 2010.
- [63] S. Otlés and B. Yalcin, "Nano-biosensors as new tool for detection of food quality and safety," *LogForum*, vol. 6, no. 4, p. 7, 2010.
- [64] M. G. Valdés, A. C. V. González, J. A. G. Calzón, and M. E. Díaz-García, "Analytical nanotechnology for food analysis," *Microchimica Acta*, vol. 166, no. 1-2, pp. 1–19, 2009.
- [65] A. Vinayaka, S. Basheer, and M. Thakur, "Bioconjugation of CdTe quantum dot for the detection of 2, 4-dichlorophenoxyacetic acid by competitive fluoroimmunoassay based biosensor," *Biosensors and Bioelectronics*, vol. 24, no. 6, pp. 1615–1620, 2009.
- [66] N. Durán and P. D. Marcato, "Nanobiotechnology perspectives. Role of nanotechnology in the food industry: a review," *International Journal of Food Science Technology*, vol. 48, no. 6, pp. 1127–1134, 2013.
- [67] N. Sozer and J. L. Kokini, "Nanotechnology and its applications in the food sector," *Trends in Biotechnology*, vol. 27, no. 2, pp. 82–89, 2009.
- [68] R. H. Hall, "Biosensor technologies for detecting microbiological foodborne hazards," *Microbes and Infection*, vol. 4, no. 4, pp. 425–432, 2002.
- [69] C. S. Kumar, *Nanomaterials for Biosensors*, Wiley-VCH, Weinheim, Germany, 2007.
- [70] X. He and H. M. Hwang, "Nanotechnology in food science: functionality, applicability, and safety assessment," *Journal of Food and Drug Analysis*, vol. 24, no. 4, pp. 671–681, 2016.
- [71] D. J. McClements and H. Xiao, "Is nano safe in foods? Establishing the factors impacting the gastrointestinal fate and toxicity of organic and inorganic food-grade nanoparticles," *npj Science of Food*, vol. 1, no. 1, p. 6, 2017.
- [72] P. N. Ezhilarasi, P. Karthik, N. Chhanwal, and C. Anandharamakrishnan, "Nanoencapsulation techniques for food bioactive components: a review," *Food and Bioprocess Technology*, vol. 6, no. 3, pp. 628–647, 2013.